4.3 DIRECT GROWTH OF CeO_2 IN STATIC AIR

The post annealing in air of the CeO_2 films grown in Ar/H_2 needs several hours to complete the reorientation of the crystal grains. To simplify the process, we studied the growth of ceria films directly in air. The first attempt was performed at 1000ºC in static air for four hours, with the same thermal ramp as in the Ar/H_2 synthesis: 60ºC/h up to 250ºC dwell of 30 min, and ramp of 200ºC/h up to 1000ºC, and precursor solution of 0.25M (25-30 nm). The AFM and XRD analysis were not promising as shown in fig. 4.13(a,b).

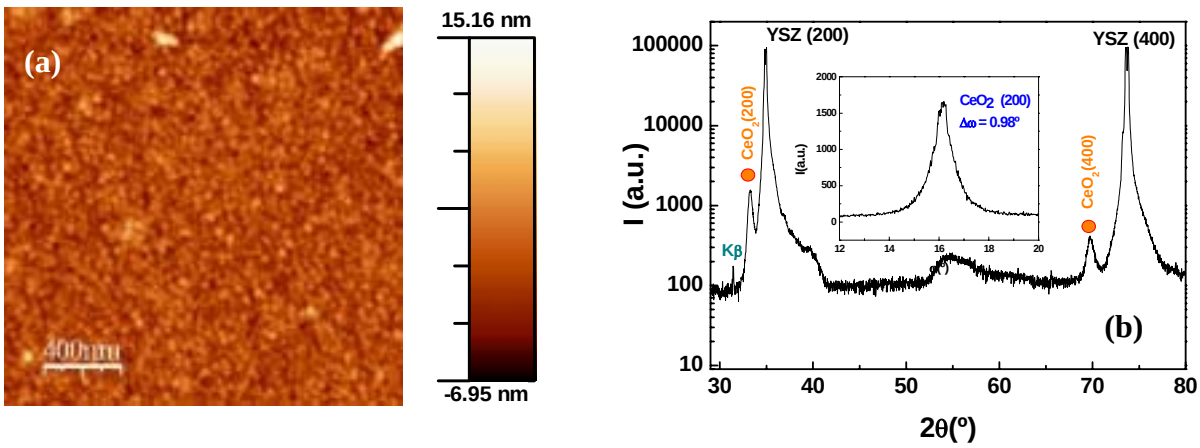

Fig. 4.13(a,b): AFM topographical image of a CeO_2/YSZ sample grown directly in air at 1000ºC for 4h. A granular morphology is shown (a). XRD pattern indicates that the ceria has grown (00l) oriented; in the inset the (200) rocking curve is presented.

The small grain morphology and low intensity of the (200) peak suggest that the crystalline film contains a randomly oriented fraction. Using a faster thermal ramp, 1500ºC/h, the amount of the epitaxial CeO_2 film begins to increase and the film surface showed a mixed terrace-granular morphology (fig. 4.15(a)).

To reach the perfect and complete epitaxy of CeO_2 films we had two different possibilities: increasing the synthesis temperature and so the cation diffusion, or increasing the duration of the thermal treatment. High temperature and oxygen atmosphere are very oxidising for metal substrates especially for stainless steal, so we decided to increase the duration. Results are shown in fig. 4.14(a,b).

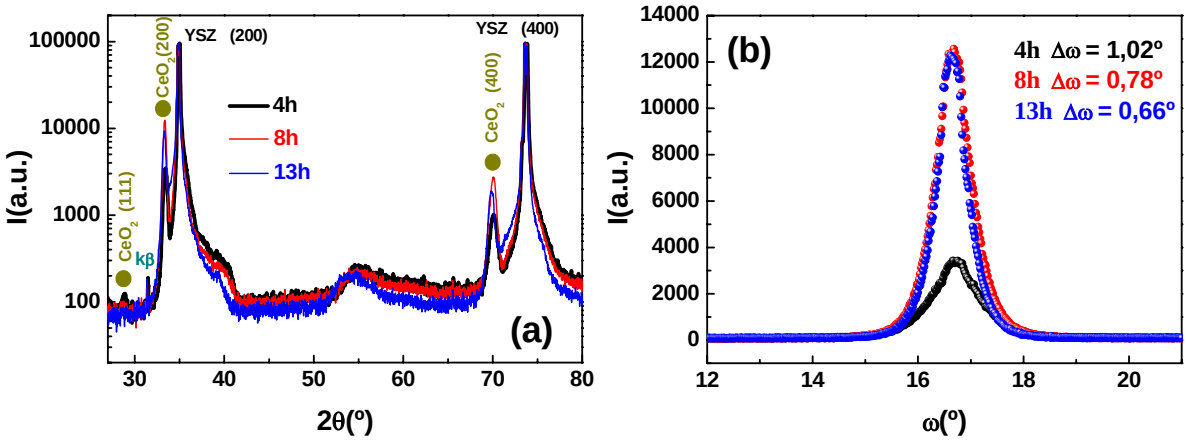

Fig. 4.14(a,b): Three samples of CeO_2/YSZ have been synthesised directly in air with a ramp of 1500ºC/h for different annealing times: 4h, 8h and 13h. θ/2θ (a) and (200) ω-scan (b) demonstrate that after 8 h the film has reached a maximum crystalline coherent volume.

Three different samples of CeO_2 on YSZ single crystals with a thickness of 25-30 nm have been synthesised: the thermal ramp was of 1500ºC/h up to 1000ºC, the atmosphere was static air and time of annealing was respectively of 4h 8h and 13h. Also for this process it is reasonable that homogeneous nucleation happens through out the film thickness, and that in a second stage the ceria film becomes epitaxial with the YSZ single crystal. AFM images, fig. 4.15(a,b,c), show that the morphology of the 8h and 13h samples consist of the characteristic (001)-faceted hillocks.

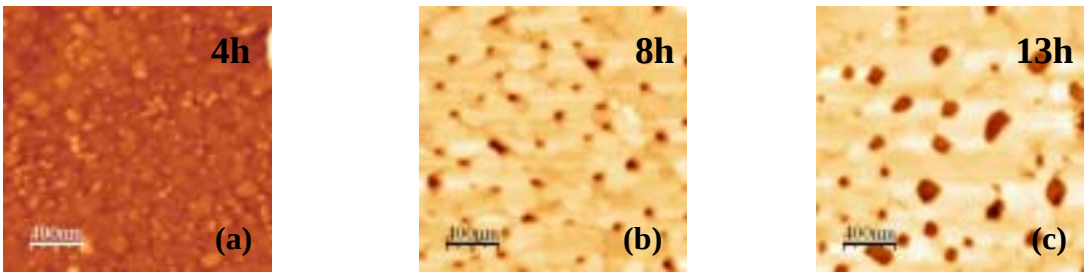

Fig. 4.15(a,b,c): AFM analysis of the CeO_2 films annealed for 4h (a), 8h(b) and 13h (c), respectively.

However, the surface roughness is similar to that found in the Ar/H_2 samples post annealed in air (fig. 4.3(b)). Rms values for the eight and thirteen hours samples are again near 3nm, (fig. 4.16).

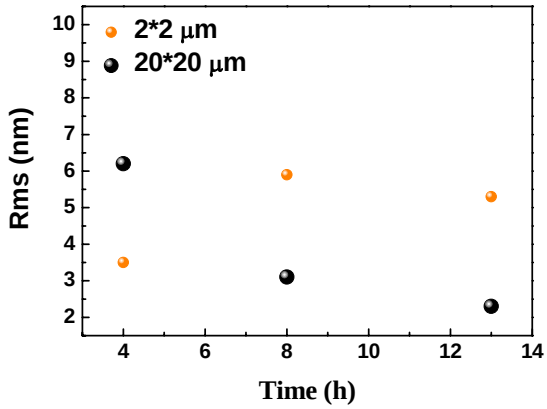

Fig. 4.16: Rms values of the three samples analysed by 20·20 and 2·2 μm areas scans.

In fact, homogeneously distributed porosity in the 8h and 13h samples is visible. The size of the pores increases with time. The out-of-plane FWHM improves with time, from 1.04º for the 4h film to the 0.66º for the 13h sample. Unfortunately the pores size increases as well with time.

Locally, far from the pores formed during the film recrystallization, the rms value is very low, often below 1 nm reflecting a very flat surface. The 2·2 μm scan images show a dense matrix of CeO_2, the grains are no longer distinguishable and only terraces are visible. SEM surface analysis of a CeO_2 film, fig. 4.17, grown directly in air, confirms the same flat and dense morphology and the homogeneously distributed porosity.

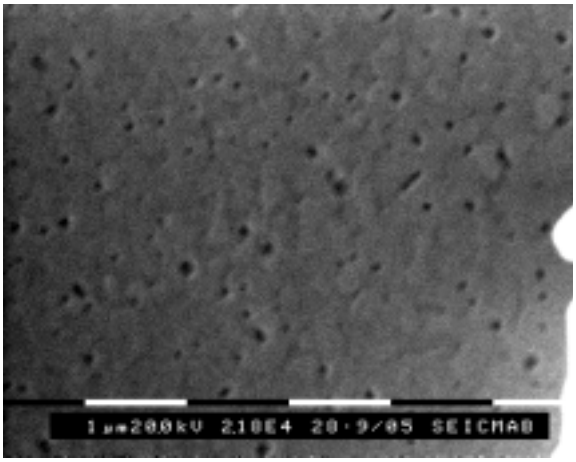

Fig. 4.17: Secondary electron image of a CeO_2/YSZ synthesised at 1000ºC in static air. Porosity can be observed in an almost featureless surface.

Fig. 4.18(a,b,c) shows some examples of porosity found in films grown for 8 hours at 1000ºC.

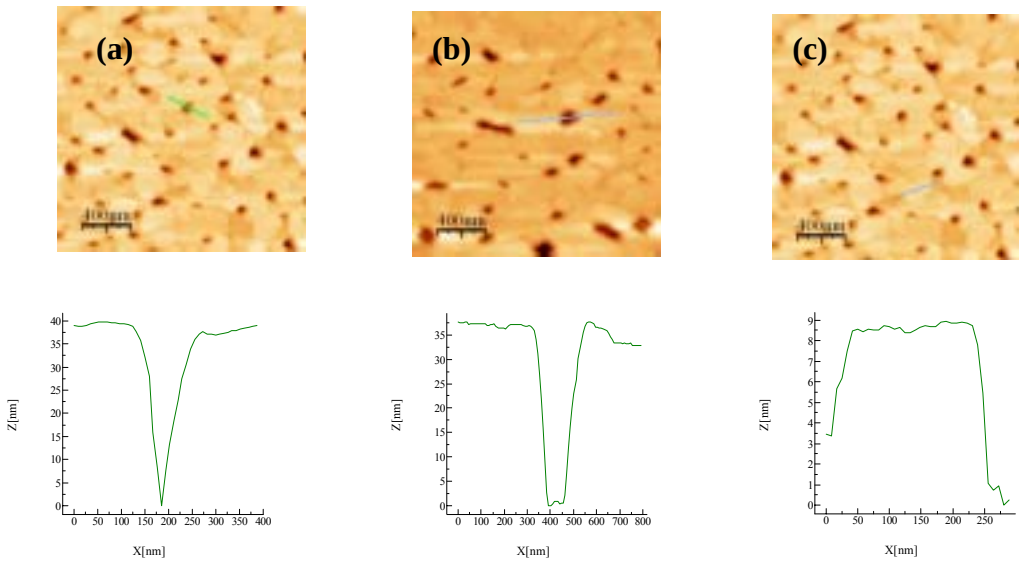

Fig. 4.18(a,b,c): AFM profiles indicate that the pores may extend down to the substrate. Their depth is near 35nm (a,b). The terraces exibit very flat surfaces (c).

The surface as said before, is terraced and (00l) oriented as for the post annealed samples, pag.82. No many significant differences with the post-annealed samples are found. The size of the terraces have a similar mean value ~200nm. Some pores measure 35 nm, for which so we can suppose that they extend down to the substrate (the samples are 25-30 nm thick). These pores formation in thin film materials, when subjected to heat treatment, is well know as reported by several groups with several materials, gold [16], silver [17], thin [18], copper [19], platinum [20] and YSZ [21]. In these studies, thin films were observed to develop holes wich would grow and coalesce to form islands.

Thermodynamic calculations, by K.T. Miller et al. [21], show that this breakup lowers the free energy of the system when the grain-size-to-film-thickness ratio exceeds a critical value. These calculations predict also that the film become more stable as film thickness is increased. . In a secondary growth regime the growth of pin holes in the thin films can be explained as the result of the deepening of the grain boundary groove at a three grains junction during grain growth as proposed by Srolovits [22].

The importance of the thermal ramp has been investigated in a wide range of rates: 200ºC/h, 360ºC/h,750ºC/h,1000ºC/h, 1500ºC/h, 1800ºC/h, and rapid thermal annealing

where the sample is introduced in the furnance at the synthesis temperature. The parameters of thickness, synthesis temperature, and duration of annealing have been maintained constant: 25-30nm, 1000ºC and 8 hours. The XRD and AFM results fig. 4.19 and 4.20 respectivily, indicate that in the range 1000ºC/h-1500ºC/h the CeO_2 is completely epitaxial with the substrate.

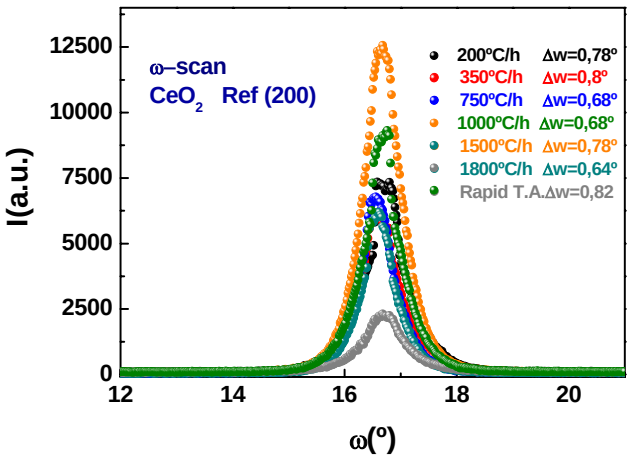

Fig. 4.19: The intensity of the (200) ω-scan of CeO_2/YSZ samples as a function of the heating ramp.

Tentatively, we can explain this behaviour as follows: when the heating rate is too small, the non epitaxial grains which have nucleated far from the substrate grow too much and it's necessary more time to consum them by the advancing growth front. For the more rapid thermal ramps, on the other hand, it is likely that the growth rate is too fast and the film is affected by a high density of growth induced defects.

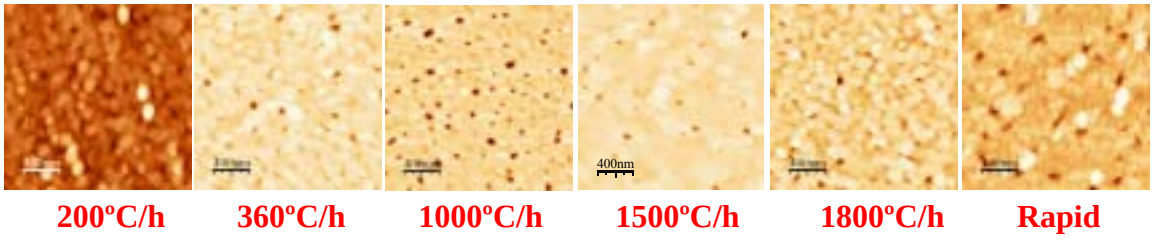

Fig. 4.20: AFM images illustrating the effect of the thermal ramp on surface morphology.

Indeed, classical grain growth models of polycrystalline films (see e.g. ref. [23]), state that those grains having a favoured epitaxial orientation grow at the expenses of

grains having a less favoured one, leading to abnormal or secondary grain growth. Such a behaviour has been indeed reported for other CSD systems, where the randomly oriented film is consumed by the advancing growth front of the first epitaxial layer (see e.g. ref. [24]). Further TEM analysis on quenched CeO_2 samples grown with different ramps is necessary to get insight into this issue.

These growth conditions have been optimised for the particular thickness of 25-30nm. The best compromise between thickness, necessary for CeO_2 to be an effective barrier against cation diffusion, and duration, leading to short processes are necessary for an industrial plant. The ω-scans measured on the samples grown with different ramp (fig.4.19), indicate that there are not important differences in the quality of the films, $0.64º<\Delta w<0.82º$.

In the case of rapid thermal annealing, although AFM did not reveal cracks, careful inspection by SEM, fig. 4.21, indicated that the rapid heating of the thin film induced the detachment of the film in several points of the substrate.

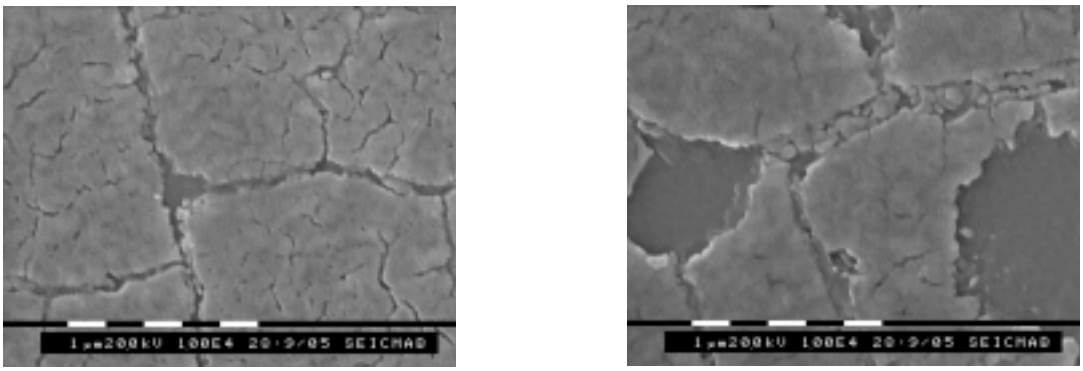

Fig. 4.21: In the CeO_2/YSZ film 25-30 nm thick obtained by rapid thermal annealing, film detachment has been observed by SEM.

We tested also thicker films at the same syntesis conditions: 1500ºC/h up to 1000ºC and dwell of 8h in static air . As expected the time is not enough to permit the transmission of the epitaxial orientation from the substrate to the surface. In fig. 4.22(a,b) a sample of CeO_2 50-60 nm thick is analysied by AFM and XRD, respectively. The surface is granular and the film is randomly oriented in its mayority.

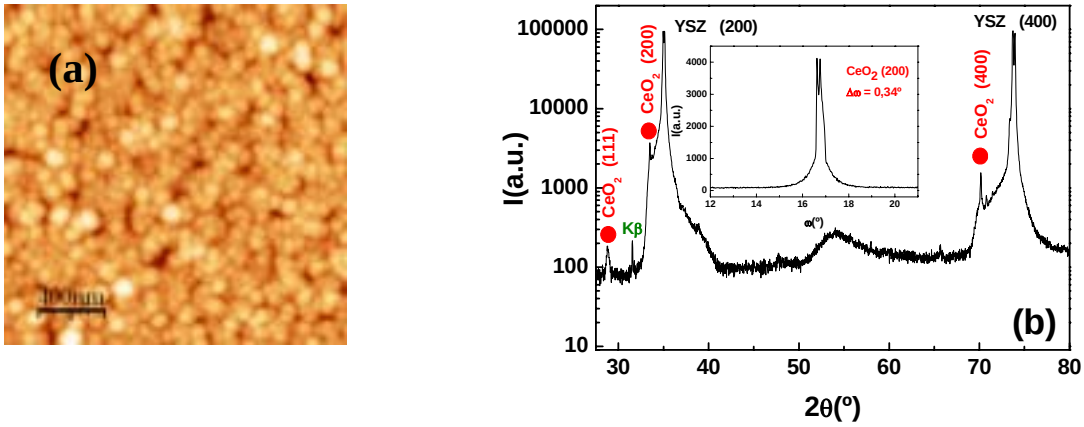

Fig. 4.22(a,b): (a) AFM analysis of a 60 nm CeO_2 film grown at 1500ºC/h up to 1000ºC for 8h in air, shows a granular film morphology. (b) θ/2θ spectra indicates that the film has one part monocristalline(sharp (00l) peaks), and upper part misoriented ((111) orientation of CeO_2 film).

In the θ/2θ analysis the sharp peaks of CeO_2, Δθ= 0.2º, indicate that the epitaxial part of the film nucleated on substrate, is almost monocristalline. On the other hand the presence of the (111) ceria orientation confirms that the upper part of the film is randomly oriented, the (111) reflection is in fact the more intense one for ceria structure.

In the inset the rocking curve of the (200) reflection is presented, Δω=0.34º. The same sample has been submitted to an extra treatment at 1000ºC for a total of 152 hours in static air (fig. 4.23(a)). The succesive treatments have been of 8h, 24h, 24h,24h and of 72h but the sample has not re-oriented (the XRD intensity of the (200) ceria peak reached only the 6500 counts after the total 152 h of annealing). The optimized conditions of syntesis for a 25-30 nm film, need to be reviewed when changing the film thickness. The grain re-orientation is substrate to surface directed thus when the film thickness is double, the time that the film needs to reach the complete epitaxy will be higher.

Fig. 4.23(b) is a plot of the (200) peak intensity as a function of annealing time. The plot indicates that the increase epitaxial volume depends linearly on time.

Comparison with the sample at pag.84 indicates that the thicker is the films, the slower is the advancement of the epitaxial growth front.

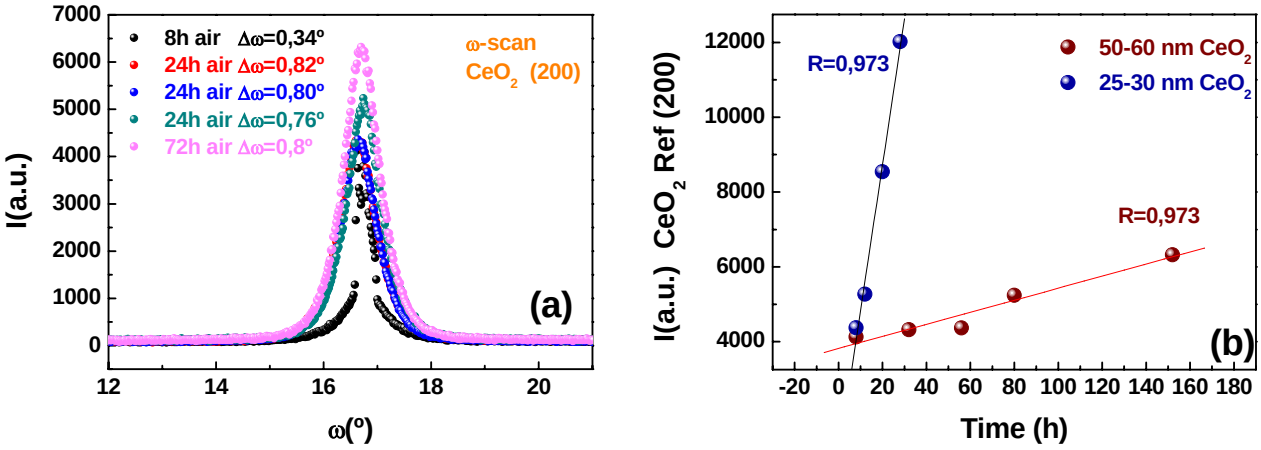

Fig. 4.23(a,b): The intensity of the (200) ceria peak increases with annealing time (a). As seen before this dependence is linear, but for this 50-60 nm film the line slope is much smaller than for the 25-30 nm one(b).

AFM analysis of the sample after the complete treatment of 152 hours is presented in fig. 4.24(a,b,c). The grain size of CeO_2 has not changed in a important way when compared with the AFM images of the sample just after growth in staic air for 8h (fig. 4.22(a)).

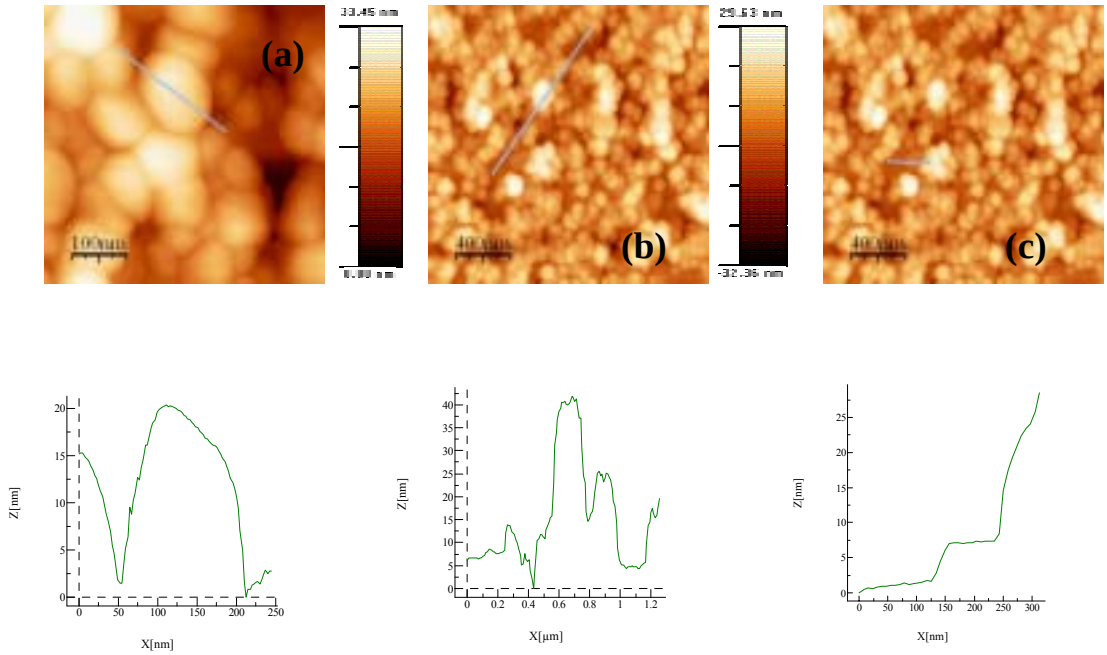

Fig. 4.24(a,b,c): AFM topographical images of the 60 nm CeO_2/YSZ film after a 152 h of annealing at 1000ºC in static air. The superficial grain size has not visible increased with respect to the sample just after the 8 h synthesis.

The morphology is still granular and far from the terraced one found in past processed samples. In the profile in fig. 4.24(a) it is easy to appriciate the grains convex shape (non facetted). The pores, already present after synthesis, (fig.4.22(a)), have increased their size and permit to analyse the inner part of the film, the one just in contact with the substrate, (fig. 4.24(c)). The profile shows a flat-terrace (pressumably (001) oriented) over which randomly oriented grains are distributed. This probably corresponds to the epitaxial part of the film that diffracts in ω–scan (fig.4.23(a)).

In polycrystalline thin films normal grain growth slow down or completely stops when grains grow to sizes comparable to the film thickness [25,26]. The preferential growth of few grains in a larger population of smaller ones is referred to the secondary grain growth [27]. The surface energy of the top and the bottom surfaces of the films plays an important role in the selection of those grains, which energetically favoured, could continue to grow. Those grains that normally have a preferred crystallographic orientation at a particular temperature grow abnormally fast till impinging on other grains with similar surface energies. A similar secondary grain growth seems to be the mechanism that in the present ceria films permits the textured grains, favoured with respect to the misoriented ones, to growth. Its rate depends inversely on the film thickness as reported by [28]. In agreement with this theory, the slope of the fitting line for the intensity-time relation of the 60 nm ceria film with respect to the one obtained for the 30 nm film (pag.94) is higher of a factor 24. As the slope is directly connected to the growth rate of textured grains, at these synthesis temperatures the process is presumably dominated by a secondary grain growth regime.

It is therefore reasonable that in the case of CSD processes, where a large fraction of the film nucleates homogeneously, the material underlines mainly at two different and opposite thermodynamic driving forces, the interface energy and the surface one, γ_i and γ_s. Probably each one of these driving forces favours grains with different orientations, the compromise between them and the particular synthesis conditions, fixes the film thickness at which one prevails over the other. Increasing the synthesis temperature should be possible to prepare a textured thicker film. Nevertheless the new process will not be useful with metal substrates as stainless steel, beacause over 1000ºC it surely would oxidise.

We can summarize the optimized parameters to synthetize epitaxial CeO_2 buffer layers as follows:

- Film thickness: 25-30 nm (precursor solution of 0.25M with 5%vol of water, 6000rpm and 3000rpm/s spinner parameters)
- Thermal ramp: 1000-1500ºC/h
- T synthesis: 1000ºC
- Synthesis time: 8h
- Atmosphere: static air (tests done in flux of pure O_2 have not given any properties improvement)

It would be interesting to understand how the film porosity influences the final superconducting properties of a YBCO film grown on this ceria buffer layer. Probably further modifications to the synthesis process, to avoid or reduce the generation of pores, will be necessary.

4.4 SURFACE ENERGY AND MORPHOLOGY

Cerium oxide is a strongly ionic crystal with the fluorite structure, in which the stacking sequence along the <100> direction consists of alternating charged planes introducing a dipole moment perpendicular to the {100} surfaces (fig.4.25).

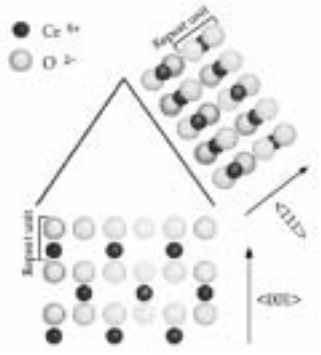

Fig. 4.25: The surface film orientation in CeO_2 can induce large variations in surface energy. The energetically highest {100} surface and the minimum {111} one are here presented [29].

Therefore, the {100} surfaces would have a prohibitively large surface energy leading to sharp maxima in the Wulff plot. As reported by R.Wallenberg [30], faceting is likely to play also a role on the roughness of (001) oriented CeO_2 films owing to the

instability of their (001) facets. Accordingly, (001) oriented CeO_2 films are forced to roughen or develop other facets. Computer simulations by Sayle et al. [31] indicate that the {111} facets are the most stable ones, in agreement with the observation by several authors that individual grains in CeO_2 films are bounded by {111} planes [30].

Obviously, since the size of the inclined facets increases with the grain size, this kind of faceting would add to the grain size dependent roughness evolution observed in our films grown in Ar/H_2 5%.

More recent theoretical calculations [29] have been performed and the surface energies, ordered after relaxation of atomic positions are: {111}<{110}<{211}<{100}<{210}<{310} with surface energy values of respectively 9.6, 15.3, 16.7, 20.3, 20.4 and 22.4 eV/nm^2, respectively.

In our ceria samples post annealed or synthesised directly in air, the formation of (001)-terraces through truncation of the (111) pyramids have been observed by TEM, leaving the (111) as the second most occurring surface (fig. 4.26(a,b)).

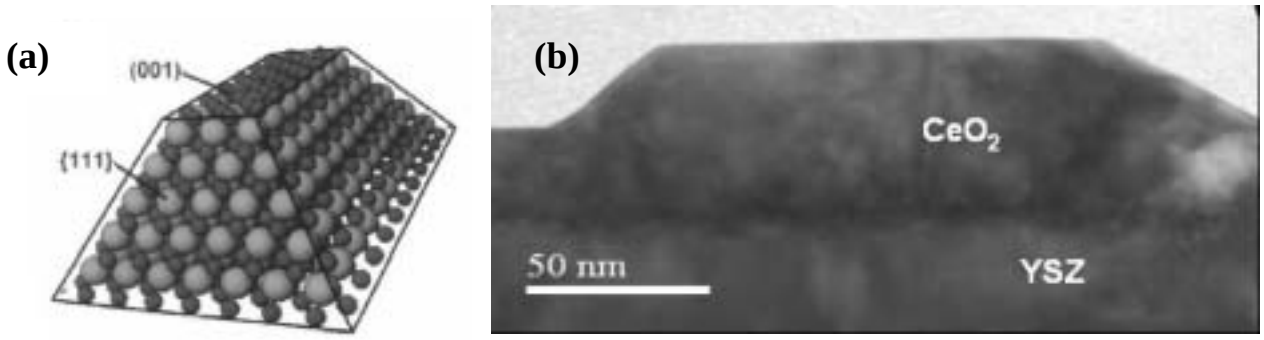

Fig. 4.26(a,b): XTEM image of a CeO_2 sample post annealed in air. Schematics of a truncated {111}pyramids [29] (a), nicely reconciles with our experimental results (b) [1].

Other researchers have experimentally shown for CeO_2 on STO, that the (001) planes can be stabilised with ½ monolayer of oxygen terminating the surface [32], i.e., surface polarity can be avoided by surface reconstruction with oxygen. Therefore, in the light of these findings it is not surprising that post processing in oxidising conditions results in the truncation of {111} pyramids by stabilization (001) planes.

Theoretically the mixed surface (001)/{111}film surface is not, from the thermodynamic point of view, the more stable configuration, but energetically could accommodate better the formation of defects and oxygen vacancies rather than the pure {111}-type [29], R.Wallenberg et al. have found an analogous surface behaviour in a similar system CeO_2-$YO_{1.5}$ where the Y^{3+} substitute part of the Ce^{4+}[30]. S.N.Jacobsen

et al. [29] have obtained a completely flat (001)-surface of CeO_2 on α-Al_2O_3 by sputter deposition, nevertheless their working conditions where far from the thermodynamic equilibrium.

4.5 GROWTH MODEL FOR MOD CeO_2

4.5.1 IDENTIFICATION OF AN IMPURITY DRIVEN GROWTH INHIBITION MECHANISM IN FILMS GROWTH IN A REDUCING CONDITIONS

In order to get insights into the growth mechanism of these nanostructured films, the temperature dependence of the in-plain grain size was investigated for nominally 25-30 nm thick films annealed for 4 h at 650°C, 700ºC, 750°C, 800°C, 850ºC, 900°C and 1300ºC in Ar/5%H_2, by quantitative analysis of AFM images. The results, depicted in fig. 4.27, show a clear increase of both, the grain size and the width of the distribution, with temperature.

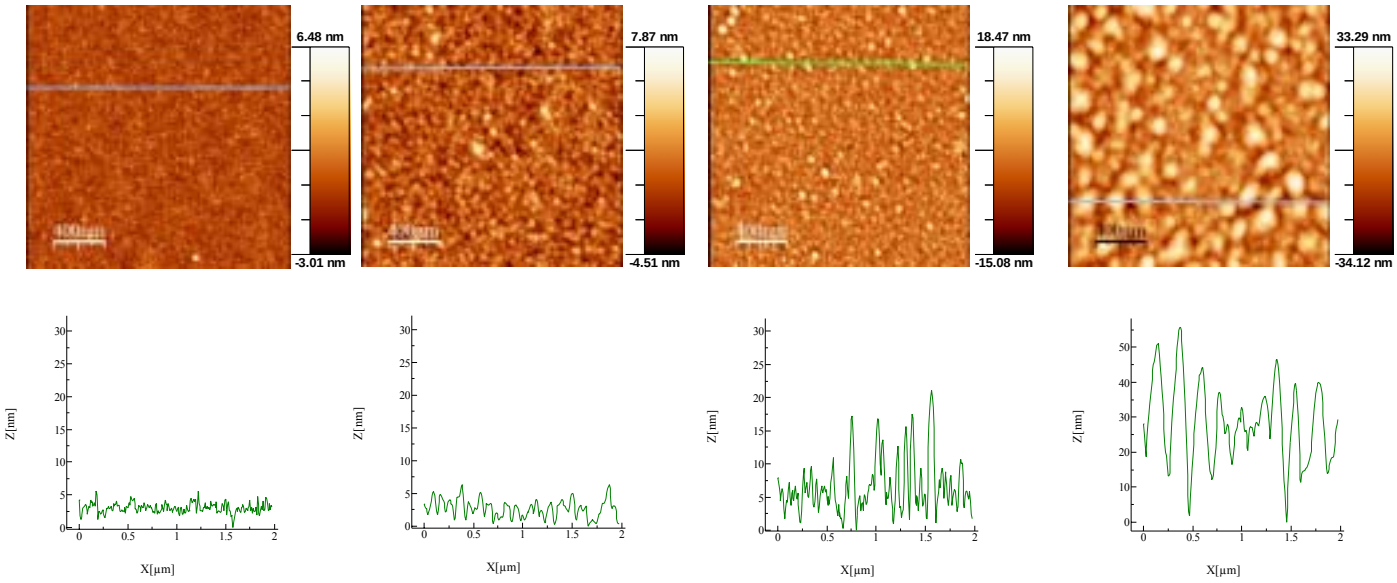

Fig. 4.27: Grain size dependence of CeO_2 thin film with temperature.

However, despite this increase in grain size, the granular character is preserved in the whole temperature range. From a comparison with TEM images, it was noted that grain sizes derived from AFM images are artificially magnified as a consequence of the

convolution of the tip and the grain shapes. Accordingly, obtained values were used to analyse the variation of the grain size but can not be taken as a realistic measure of the lateral size of the grains. In 3D systems, thermically activated grain growth typically obeys the relationship $\langle r\rangle^2 - \langle r_o\rangle^2=\alpha t$, where $\langle r\rangle$ is the average grain radius after a time t, $\langle r_o\rangle$ is average initial grain radius, and $\alpha=\alpha_o exp(-Q/kT)$ where α_o is a weakly temperature dependent constant, Q is an activation energy for grain boundary motion, and k and T have their usual meanings [33]. In MOD films the initial grain size can be neglected and the following Arrhenius type dependence is obtained

$\langle r\rangle^2=\alpha_o t exp(-Q/kT)$,

which is characteristic of a thermally activated process driven by the motion of grain boundaries. Fig. 4.28 shows a plot of $2\ln\langle r\rangle$ against 1/T. The good fit (R=0.9996) of the experimental data to the model supports that grain growth in these films is governed by the motion of grain boundaries with a negligible effect of the substrate, which is consistent that the grain size is smaller the film thickness.

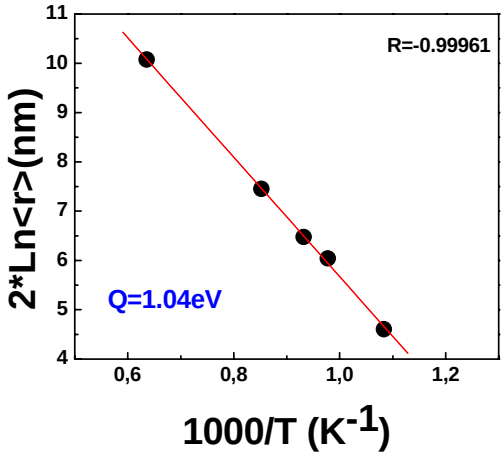

Fig. 4.28 : Arrhenius plot of the grain size dependence on the reciprocal of temperature.

From the slope of this plot, a value Q=1.04 eV was obtained, which compares well with the value ~ 1.1 eV obtained from other CSD derived CeO_2 films [34]. Such thin film values are significantly larger than 0.16 eV and 0.50 eV determined for the growth of bulk nanocrystalline (initial grain diameter 4-5 nm) CeO_2 for T<600ºC and T>600ºC, respectively [35]. Such a difference between the grain growth behaviour of CSD

derived films and bulk nanocrystalline samples suggest the action of a microstructural mechanism inhibiting grain growth in those films. It is interesting to note that such a mechanism can be at the origin of the observed anomalous granular microstructure prevailing after annealing the films at 750ºC for 4h under an Ar/5%H_2 atmosphere. The above considerations suggests that in films deposited in an Ar/5%H_2 atmosphere there is some microstructural impediment for grain growth.

Fig. 4.29(a) is an EELS mapping of the C distribution in an as grown sample, superposed to an image of the microstructure of the mapped area. The C concentration is proportional to the density of black dots. The image clearly shows that C impurities decorate grain boundaries and porosity. Fig. 4.29(b) compares the EELS spectra obtained from an as-grown film and a post-processed one, indicating that the carbon K (C-K) peak disappears after annealing under oxidising atmospheric conditions.

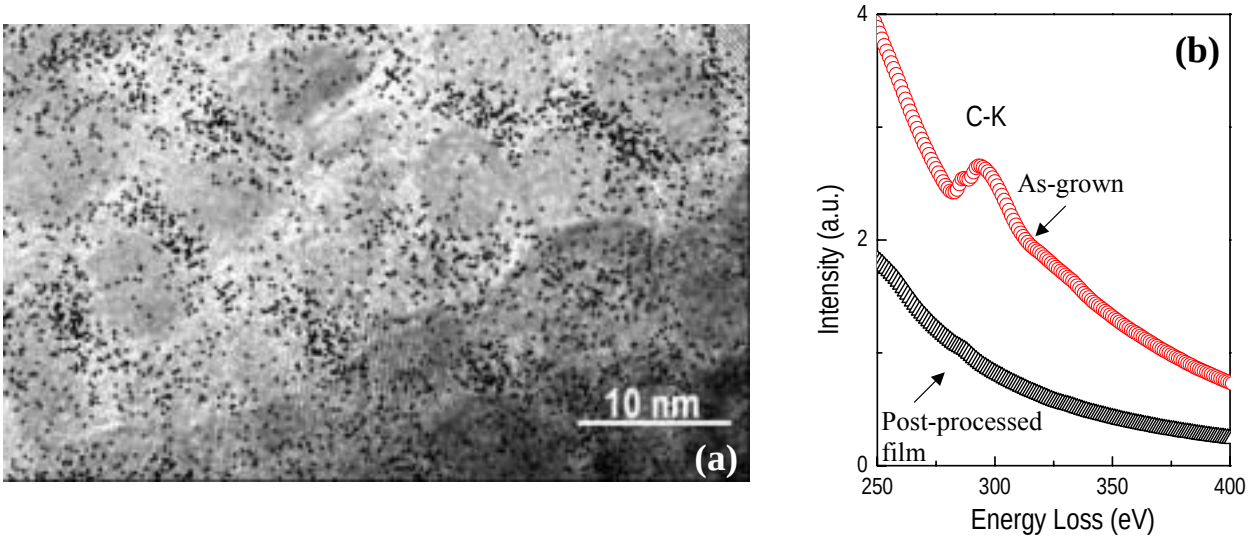

Fig. 4.29(a,b): EELS mapping of the C distribution through the cross sectional area of an as-grown CeO_2/YSZ film, superposed to an image of the microstructure of the mapped area (a). Comparison of EELS spectra obtained from an as-grown film and a post-processed one (b) [2].

Therefore, post processing is highly effective in cleaning residual C via oxidation. Unexpectedly, however, C migration from grain boundaries and interconnected porosity can induce localised but severe etching of the substrate. Fig. 4.30(a,b) is a high resolution XTEM image showing such an etch pit, which appears as a white faceted inclusion in the substrate covered by the CeO_2 film, along with the EELS spectrum taken within the inclusion exhibiting a prominent C-K peak.

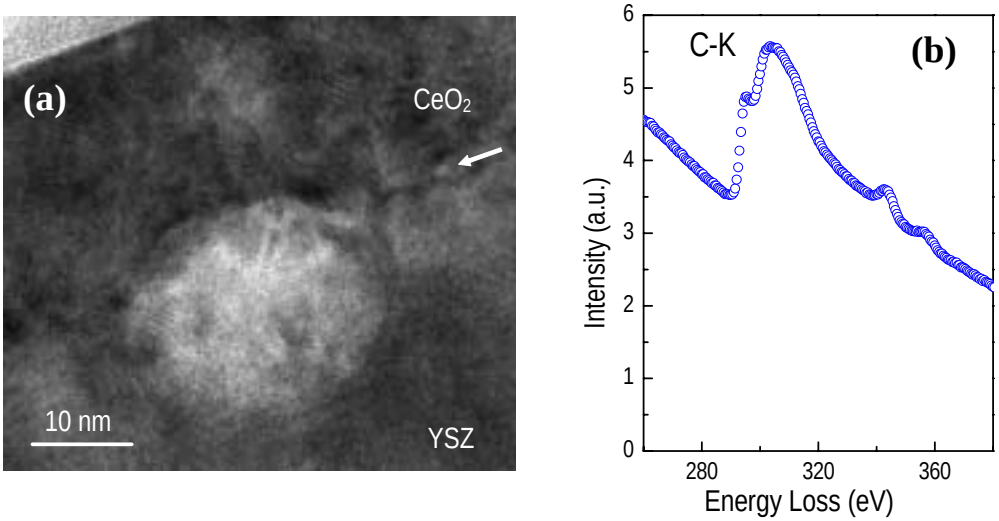

Fig. 4.30(a,b): (a) High resolution XTEM image of post processed film viewed along <100>. Interface is indicated by an arrow. The image shows facetted void originated at the interface and extending into the substrate. (b) EELS spectra taken within the void is shown in the right panel.

Our results demonstrate that both surface disorder and surface roughness are direct consequences of a marked granularity which prevails after a 4 hours anneal at temperatures comprised between 650ºC and 900ºC in Ar/5%H_2. This indicates that the advancement of the growth front of the first epitaxial layer through the nanocrystalline disordered CeO_2 film is impeded by some microstructural mechanism that is deactivated under oxidising conditions. It is well known that impurity atoms may decrease the mobility of grain boundaries [36-37]. Hence, the observation of C atoms decorating grain boundaries and filling porosity in as-grown samples can explain the observed frozen-in granular microstructure after thermal processing. An analogous growth inhibition mechanism has been reported for other sol-gel derived nanocrystalline metal oxides [38]. This scenario is erased by post processing under oxidising conditions. Oxygen can clean out the grain boundaries and porosity via oxidation of C, thus unblocking grain growth and promoting the solid-state epitaxial growth through the whole thickness of the films. The activation energy of grain boundary motion of ceria thin films grown directly in static air is supposed to change with respect to the one for samples grown in Ar/H_2. Unfortunately it was impossible to measure the grain size by AFM analysis; the grains are in fact too well interconnected and their boundaries are not easily distinguishable

4.5.2 SUMMARY

- In CSD films nucleation occurs under very high under cooling and homogeneous and heterogeneous nucleation take place simultaneously.
- In Ar/H_2 synthesis carbon residues in the grain boundaries inhibit grain growth, and the film remains granular.
- After crystal growth, reorientation of the grains is possible, after liberating the grain boundaries from the carbon residues.
- A fully (00L) oriented CeO_2 film can be obtained by synthesising the film at high temperature (T>900ºC) in air for a time t that depends on the film thickness.

Fig. 4.31 presents a schematic resume of ceria nucleation and growth.

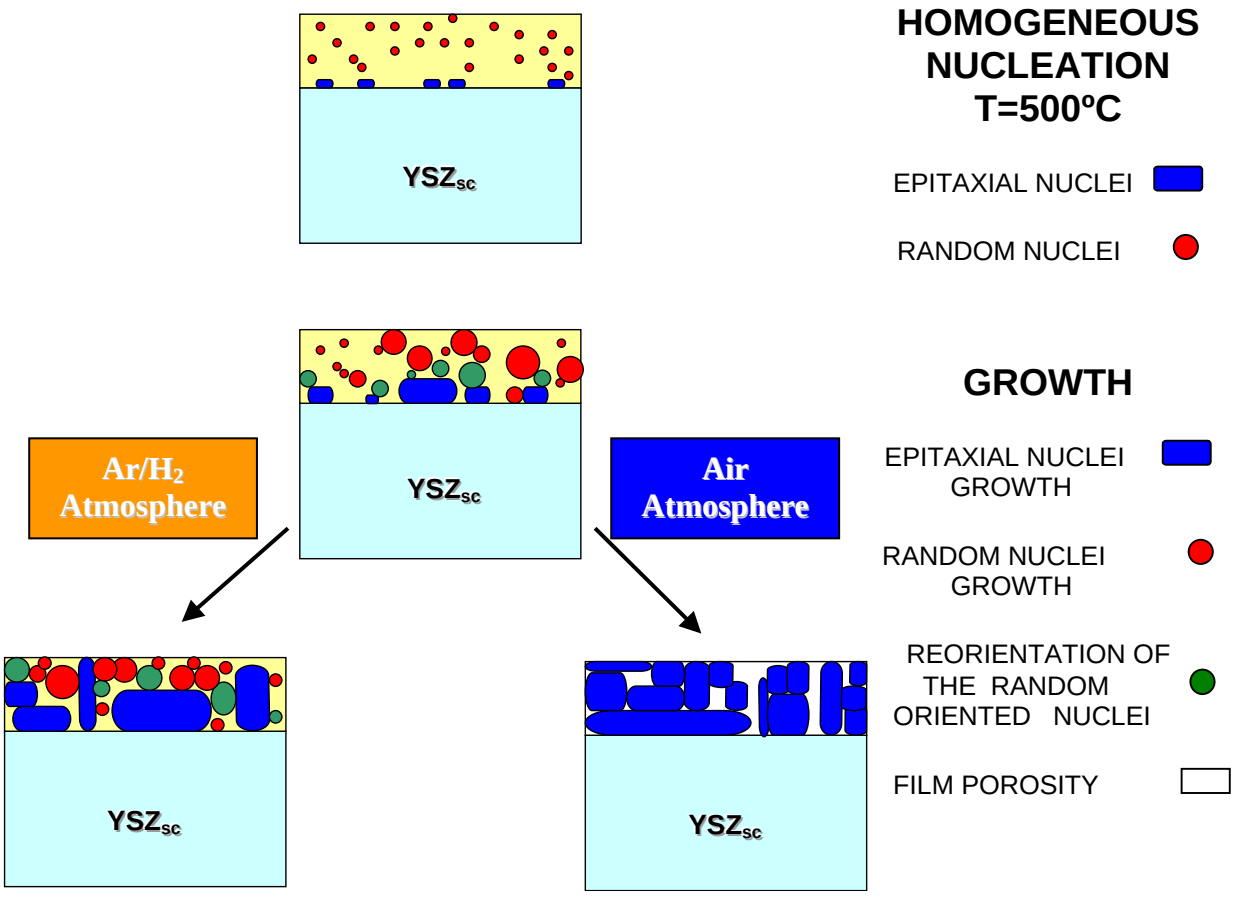

Fig. 4.31: Schematic of the growth process of CeO_2

4.6 SELF-ASSEMBLING OF MOD-CeO_2 ISLANDS

It is well known that above a certain thickness ~400nm, the YBCO cannot support the same current densities through out the whole thickness [39]. Recent studies [40] have indicated that YBCO can grow perfectly from the crystallographic point of view and the loss of pinning is due to the lower quantity of film defects on the top superconducting layer.

Tuning long linear defects in the YBCO film is a way to enhance flux pinning, and therefore Jc. Patterning techniques exist to date to produce chemical and topographical contrasts (i.e. microcontact printing, microfluidic patterning, atomic force lithography, electron beam lithography, photolithography and photodegradation or photoactivation of self-assembled monolayers (SAMs)). The use of colloidal suspensions for in situ generating nano patterns on a substrate could be a viable solution. In such a process, colloids in a suspension are adsorbed on a substrate and a pattern is generated. Preliminary studies of columnar defects generated on the substrate before depositing YBCO have been developed. The idea consists on using a very diluted solution to grow nano-particles of ceria in a substrate, and study their distribution. Nobody knows which is the optimum morphology that the particles must have to reach the maximum pinning, probably as long enough to cross the total film thickness and as smaller as possible in diameter. Also topographical accidents can induce growth defects useful as pining centres.

In the first approach we synthesise particles of CeO_2 on STO single crystals. The STO was previously treated for 1 hour in static air, the annealing in fact promotes a rearrangement of the surface, only TiO termination and a step structure appears. This structure favours, using vacuum technique, the particles nucleation between steps and step as reported by Lagally [41].

In these tests we used a precursor solution of 0.006M and a synthesis in Ar/H_2 at 750ºC for 4h. AFM results of two of these samples are presented in fig. 4.32.

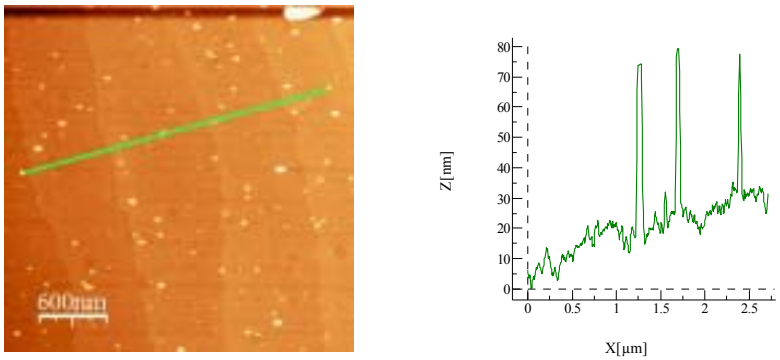

Fig. 4.32: AFM image of super diluted solution deposited on YSZ single crystal at 750ºC in Ar/H_2 for 4 h.

The grains seem to be quite homogenously distributed, with a height near 80-100 nm and an in-plane bottom size of 100nm against the 20nm on the top grain. The grains do not move to the positions between step and step as observed [41].

Four samples from a 0.03 M precursor solution at 1000ºC for 8h have been prepared in static air. To investigate the chemical and geometrical effects on the growth of CeO_2 used different substrates: STO (001), LAO (001), YSZ (001) and Al_2O_3 (1-102). The AFM analysis of the 500·500 nm and 2·2 μm scans of these samples are presented in fig. 4.33. Nevertheless, unexpectedly we find that the higher the solution concentration, the lower is the mean height of these islands.

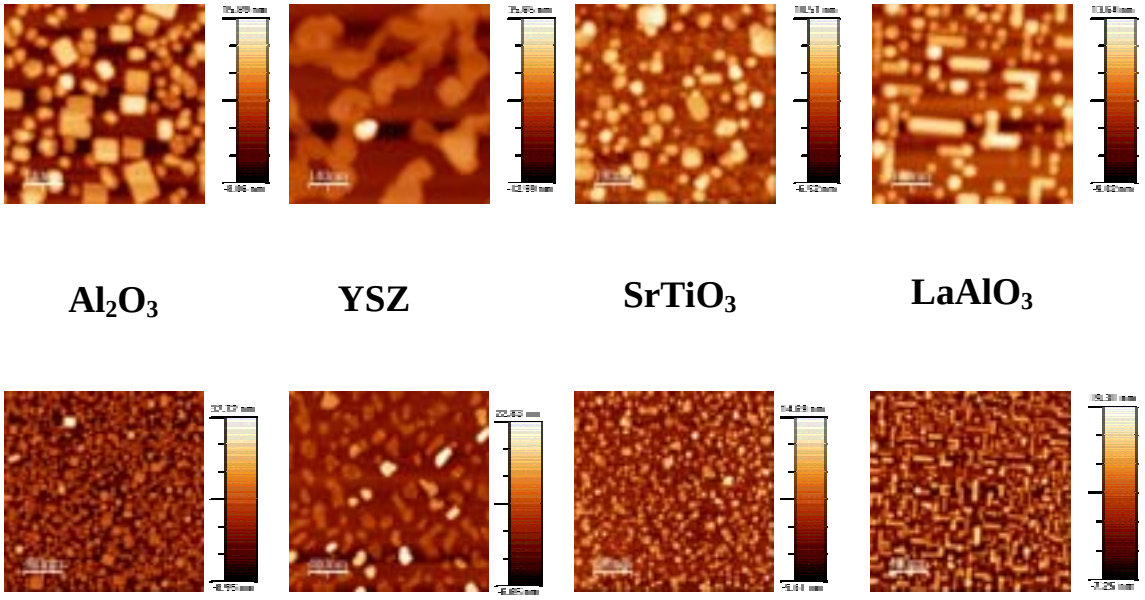

Fig. 4.33: AFM topographical images of CeO_2 islands grown at 1000ºC for 8 h in static air on different substrates. Depending on the substrate the growth stress of the islands will be different.

The ordered rectangular shape of ceria islands grown on LAO are probably oriented following the twins orientations of the underlying single crystal substrate.

In fig. 4.34(b) the mismatch of ceria with the different substrates is reported; for STO and LAO single crystals, the theoretically calculation has been performed taking in account the most favourable diagonal growth of the CeO_2 cell.

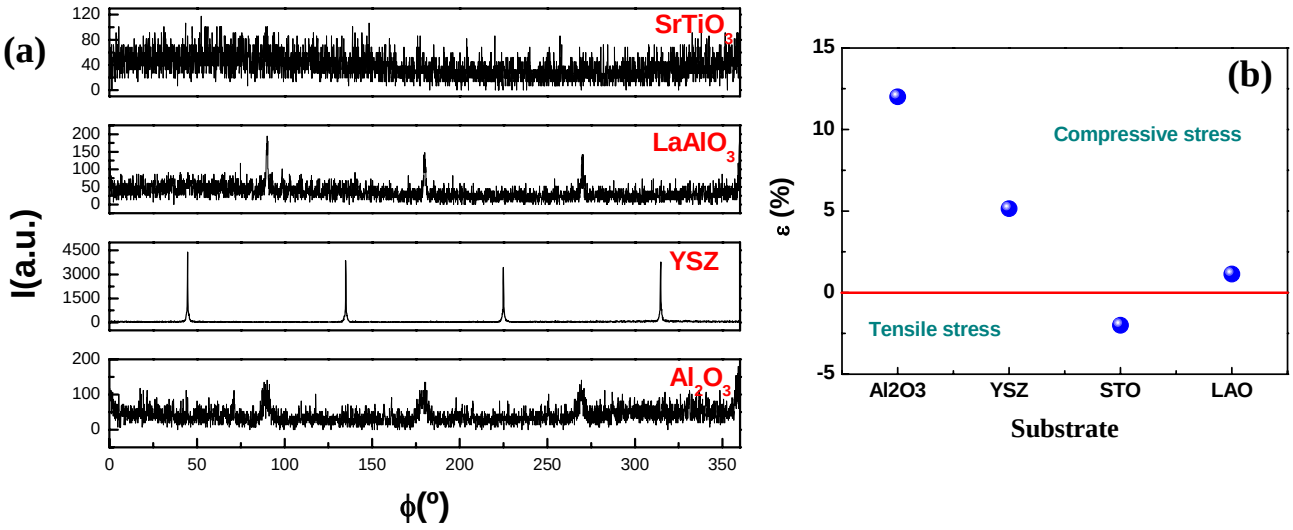

Fig. 4.34(a,b): (111) ϕ-scan analysis of the CeO_2 islands (a). Theoretical strain calculated for the ceria growth on Al_2O_3, YSZ, STO and $LaAlO_3$ (b). For the STO and LAO the calculation has been performed taking in account the more favourable diagonal configuration.

It is interesting to note that the CeO_2, grows on STO covering nearly the whole substrate, but without texture. Probably because is the only example where the ceria grows under tensile stress. All these four CeO_2 samples have been submitted to the in plane analysis as reported in fig. 4.34(a). The reflection for ϕ–scan of ceria was the (111) for all the samples. Only on STO substrate, the CeO_2 grows totally in plane disoriented. The YSZ single crystal nevertheless, with a good mismatch with ceria, exhibits the better in-plane texture.

A precursor solution of 0.25 M has been deposited on STO single crystal and synthesised at 1300ºC for 4 h. This time the ϕ–scan analysis, fig. 4.35, shows a clear increase of the in plane texture of the CeO_2 film. The 45º distance of the (111) peaks of the STO with respect the (111) of CeO_2, confirms the diagonal configuration of the CeO_2 cell on the STO one.

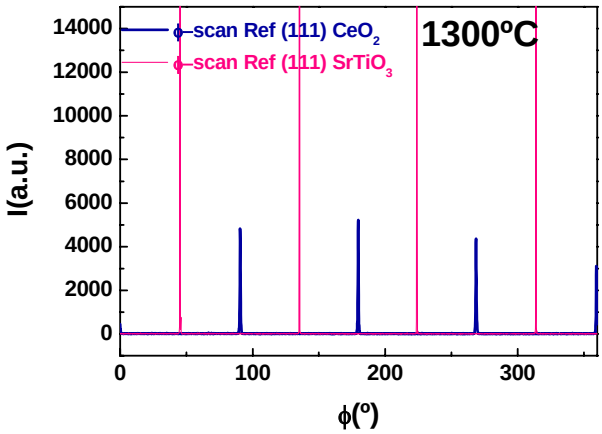

Fig. 4.35: (111) phi-scan analysis of the CeO_2/STO^{SC} sample. The relative position of the peaks confirms the diagonal growth of the CeO_2 cell with respect to the STO^{SC}.

AFM analysis of this sample has shown, fig. 4.36, a different island morphology with respect to the sample grown at 1000ºC. The substrate is not totally covered and the ceria seems to form a kind of labyrinth. In this sample the holes formation and growth has induced the dewetting of the ceria film that has broken into islands.

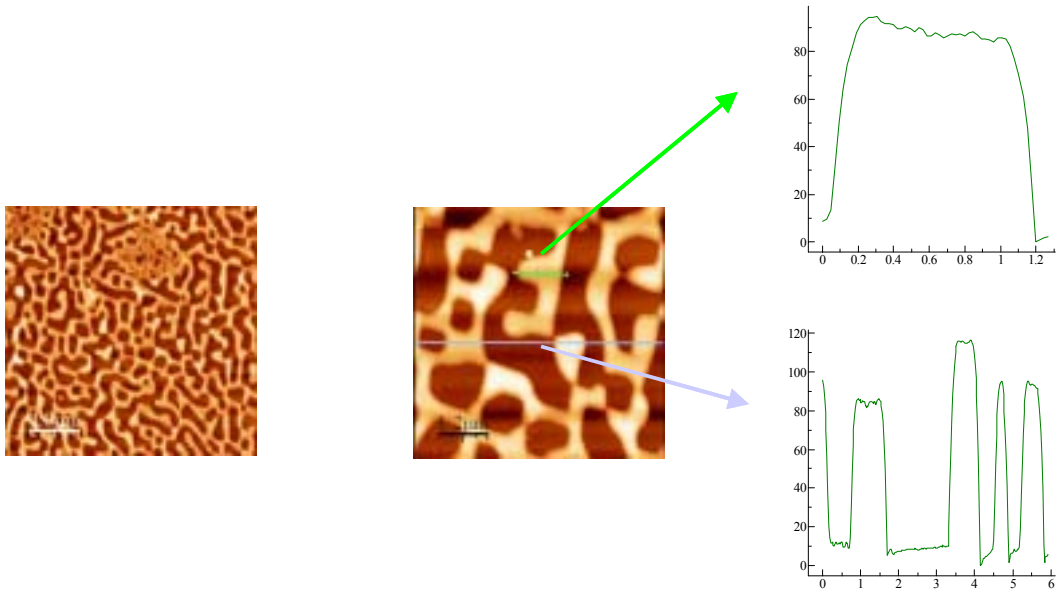

Fig. 4.36: AFM topographical images of the CeO_2 film grown at 1300ºC for 4h. The profiles reveal a flat surface, presumably (001).

The top of it is probably near (00l) as indicates by the profiles presented in fig. 4.36. These preliminary tests seem to that it is possible to tailor self assembled structures, by playing with the synthesis conditions and substrate mismatch.

REFERENCES

[1] J.Gazquez Phd Tesina Universitat Autonoma Barcelona, (2005).

[2] F. Sandiumenge, A. Cavallaro, J. Gàzquez, T. Puig, X. Obradors, J. Arbiol and H. C. Freyhardt, *submitted Nanotechnology, (2005).*

[3] S. N. Jacobsen, L. D. Madsen, U. Helmersson, *J. Matter. Res, **14**, 2385, (1999)*

[4]J.C.Nie, H.Yamasaki, H.Yamada, Y.Nakagawa, and K.Develos-Bagarinao, *Sepercond.Sci.Technol., **16**, 768-772, (2003).*

[5] Andrea Cavallaro, Felip Sandiumenge, Jaume Gàzquez, Teresa Puig, Xavier Obradors, Jordi Arbiol, and Herbert C. Freyhardt, *Adv. Funct. Mater. , submitted (2005)*

[6] P.-Y.Lin, M.Skoglund, L.Löwendahl, J.-E.Otterstedt, L.Dahl, K.Jansson, M.Nygren, *Appl.Catal. B, **6**, 273, (1995).*

[7] W.Liu, M.Flytzani-Stephanopolous, *J.Catal. B, **153**, 304, (1995).*

[8] T. Inoue, T.Setoguchi, K.Eguchi, H.Arai, *S*olid State Ion., Dic.React., **35**, 285, (1989).

[9] H.L.Tuller, *Mixed conduction in nonstoichiometric oxides. In Non-Stoichiometric Oxides, ed. O. Toft Sorensen, Academic Press, New York, 271-335, (1981).*

[10] M.Romeo, K.Bak, J.El Fallah, F.Le Normand, L.Hilarie, *Surf. Interface Anal., **20**, 508, (1993).*

[11] A.Pfau, K.D.Schierbaum, *Surf. Sci., **321**, 71, (1994).*

[12] M.Shelef, L.P.Haack, R.E.Soltis, J.E.de Vries, *J.Catal., **137**, 114,(1992).*

[13] M.Hoang, A.E.Hughes, T.W.Turney, *Appl.Surf.Sci., **72**, 55, (1995).*

[14] M.A.Henderson, C.L.Perkins, M.H.Engelhard, S.Thevuthasan, C.H.F.Peden, *Surface science, **526**, 1-18, (2003).*

[15] J.P.Holgado, G.Munuera, J.P.Espinós, A.R.González-Elipe, *Appl. SurfaceScience, **158**, 164-171, (2000).*

[16] M.L.Gimpl, A.D.Mcmaster, and N.Fuschillo, *J.Appl.Phys., **35**, 3572-3575, (1964).*

[17] A.E.B.Presland, G.L.Price, and D.L.Trimm, *Prog.Surf.Sci., **3**, 63-96, (1973).*

[18] H.Caswell and Y.Budo, *J.Appl.Phys., **35**, 644-647, (1964).*

[19] L.Bachmann, D.L.Sawyer, and B.M.Siegel, *J.Appl.Phys., **36**, 304-308, (1966).*

[20] N.L.Wu and J.Philips, *J.Appl.Phys., **59**, 769-779, (1986).*

[21] K.T.Miller and F.F.Lange, *J.Appl.Phys., **5**, 151-160, (1990).*

[22] D.J. Srolovitz, S.A.Safran, *J.Appl.Phys., **60**, 247-260, (1986).*

[23] C. V. Thompson, *Annu. Rev. Mater. Sci., **20**, 45, (1990).*

[24] K. T. Miller, C. J. Chan, M. G. Cain, F. F. Lange, *J. Mater. Res., **8**, 169, (1993)*.

[25] P.A.Beck, J.C.Kramer, L.J.Demer, and M.L.Holzworth, *Trans.AIME, **175**, 372, (1948)*

[26] J.Palmer, C.V.Thompson, and H.I.Smith, *J.Appl.Phys., **62**, 2492, (1987).*

[27] C.V.Thompson, and J.Floro, *J.App.Phys., **67**, 4099, (1990).*

[28] F.F.Lange, *Naterials Science Forum, **113-115,** 81, (1993).*

[29]S.N.Jacobsen, U.Helmersson, R.Erlandsson, Björn Skarman, L.R.Wallenberg, *Surface Science, **429**, 22-33, (1999).*

[30]R.Wallenberg,R.L.Withers, D.J.M.Bevan, J.G.Thompson, B.G.Hyde, *J.Less-Common Met., **156**, 1, (1989).*

[31] T.X.T.Sayle, C.Parker, and C.R.A.Catlow, *Surf.Sci., **316**, 329, (1994).*

[32] G.S.Herman, *Surf.Sci., **437**, 207-214, (1999).*

[33] C. V. Thompson, *Annu. Rev. Mater. Sci., **20**, 45, (1990),.*

[34] T. Suzuki, I. Kosacki, H. U. Anderson, Ph. Colomban, *J. Am. Ceram. Soc., **84**, 2007, (2001).*

[35] X.-D. Zhou, W. Huebner, H. U. Anderson, *Appl. Phys. Lett., **80**, 3814, (2002).*

[36] F. J. Humphreys, M. Hatherly, *Recrystallization and Related Annealing Phenomena, Pergamon, Oxford, 1995.*

[37] P.-L. Chen, I.-W. Chen, *J. Am. Ceram. Soc., **79**, 1793, (1996).*

[38] N.-L. Wu, S.-Y. Wang, I. A. Rusakova, *Science, **285**, 1375, (1999).*

[39] H.Yamasaki, A.Rastogi, A.Sawa, *Cryogenics, **41**, 69-75, (2001).*

[40] J.Wang, B.Han, F.Chen, T.Zhao, F.XU, Y.Zhou, G.Chen, H.Lu, Q.Yang, T.Cui, *Solid State Communications, **126**, 431-434, (2003).*

[41] M.G.Lagally, and Z.Zhang, *Nature, **417,** 917, (2002).*

Chapter 5

$BaZrO_3$, $SrTiO_3$ AND $SrTiO_3$/$BaZrO_3$ ARQUITECTURE BY THE CHELATE PROCESS

The study of the film growth of BZO and STO is presented in this chapter. The two model systems employed to simulate the substrate behaviour of polycrystalline NiO(SOE)/Ni and YSZ(IBAD)/SS were respectively the MgO and the YSZ single crystals.

The synthesis of the single buffer STO and the double buffer STO/BZO on MgO single crystal has been investigated. On the YSZ^{SC} only the double buffer growth has been studied. The hypothesis of using BZO as direct template for the YBCO synthesis has been discarded after the deposition tests of YBCO films by TFA on BZO/LAO^{SC}, which have only produced highly disordered superconducting materials [1].

5.1 EXPERIMENTAL

Chemical solution for BZO and STO buffer layers were prepared from a variety of precursors, including acetate, acetylacetonate and isopropoxide. The precursor and solvents were purchased from Aldrich and Alpha. Anhydrous methanol and other solvents with the lowest water content have been used.

5.1.1 SOLUTION SYNTHESIS OF BARIUM ZIRCONATE

The precursor solution with a concentration in the range of 0.3-0.9 M were prepared by dissolving a stoichiometric amount of barium acetate (Aldrich) plus the same number of moles of zirconium acac (Alfa Aesar) into a volume of glacial acetic acid (Panreac). Solutions of typically two millimetres in volume were stirred for about

30 minutes at room temperature. The nominal concentration value of the solution is refereed to the sum of moles of each cation (e.g. one litre of 0.3M solution will contain 0.15 moles of Zr and 0.15 of Ba). This precursor solution is stable over at least one week.

5.1.2 SOLUTION SYNTHESIS OF STRONTIUM TITANATE

This precursor solution is prepared in two steps: first, a stoichiometric amount of strontium acetate (Aldrich) is dissolved in glacial acetic acid and stirred for 20-30 minutes. Meanwhile the same number of moles of Ti-isopropoxide is weighted directly into a volume of methanol, drop by drop, to avoid the titanium hydrolisation. The two solutions are mixed together and stirred for other 30 minutes. The relation vol.(acetic acid)/vol.(methanol) is one to one and the final solution concentration is also defined as sum of cations moles. The concentration range of the precursor solution used in this work was of 0.25M-0.5M and its stability was proved for over a week.

5.1.3 FILM DEPOSITION AND THERMAL TREATMENT

The solution is deposited by spin coating with the same process parameters employed for the ceria films, see pag.58, which guaranteed a complete and homogeneous substrate coverage. These parameters are: 13 μl of solution (for 5·5 mm substrate), 6000rpm, an acceleration of 3000rpm/s and a total deposition time of 2 min.

The films are synthesised with the thermal ramp shown in fig. 5.1:

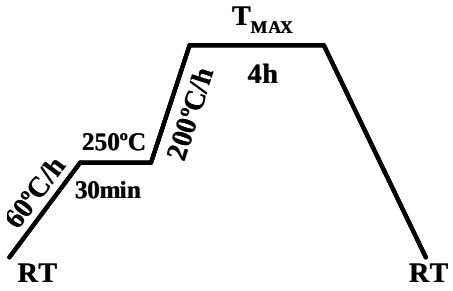

Fig. 5.1: Synthesis thermal process.

This synthesis process consists of three ramps, the first of 60ºC/h up to T=250ºC where stops for 30 min, the second of 200ºC/h up to Tmax at which the oven is maintained for 4h, and the final ramp of 200ºC/h that controls the cooling down to room temperature.

5.2 RESULTS AND DISCUSSION

The viscosity of the precursor solutions with a concentration of 0.3M for BZO and 0.25M STO have been measured by rheometer at 25ºC. The viscosity of BZO precursor solution was 1.72 mPa·s and for STO 1.5 mPa·s. These values are similar to the 1.8 mPa·s measured for a ceria precursor solution with a concentration of 0.25M at 25ºC.

In fig. 5.2(a) a TGA performed at 60ºC/h thermal ramp of a dry BZO precursor solution is presented. The organic decomposition starts at 250ºC and does not stop before 500ºC. The three IR spectra of a BZO film, fig. 5.2(b), first just after deposition, then treated till 250ºC at 60ºC/h and finally post annealed at 200ºC/h till 500ºC, confirms that the decomposition of acetylacetonate group appearing at 1600-1400 cm^{-1} is not complete at 500ºC.

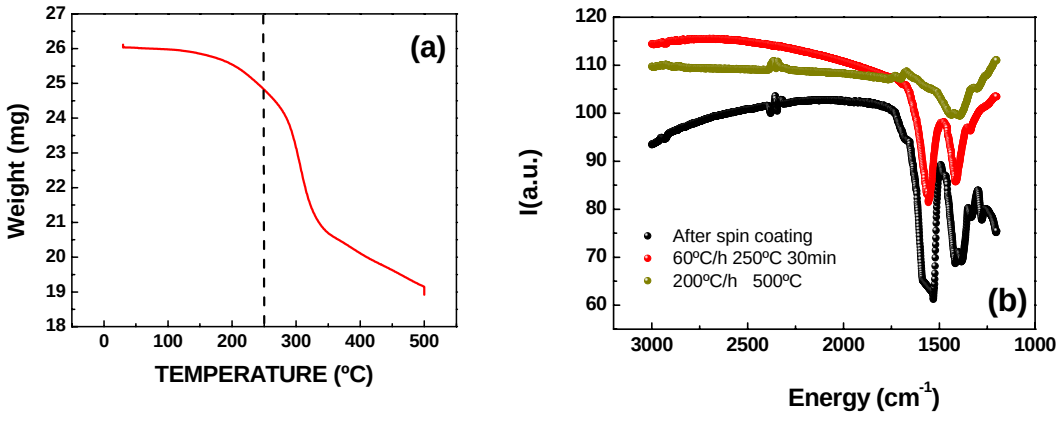

Fig. 5.2(a,b): (a) TGA analysis of a dry precursor solution for BZO indicates that the film decomposition starts at 250ºC. (b) IR analysis of a BZO film has been done after deposition (black line), a thermal treatment at 250ºC (red) and a final heating up to 500ºC (green line).

Further experiments to shorter the synthesis process and optimise the thermal treatment should be prepared. No important variations in the texture or in the film morphology are expected.

5.2.1 THICKNESS CONTROL

The thickness of the BZO films grown at the same synthesis conditions and in a concentration range of the precursor solution of 0.15-0.6 M has been measured by X-ray reflectivity see pag.32. These values (red squares) with the ceria ones (green circles) are presented in fig. 5.3. They all follow the same linear relation with solution concentration, (see chapter 3 pag.66). A sample of STO prepared with a 0.25M precursor solution and deposited on a substrate half covered by a resin has been measured by profilometry, after the synthesis, when the resin has decomposed.

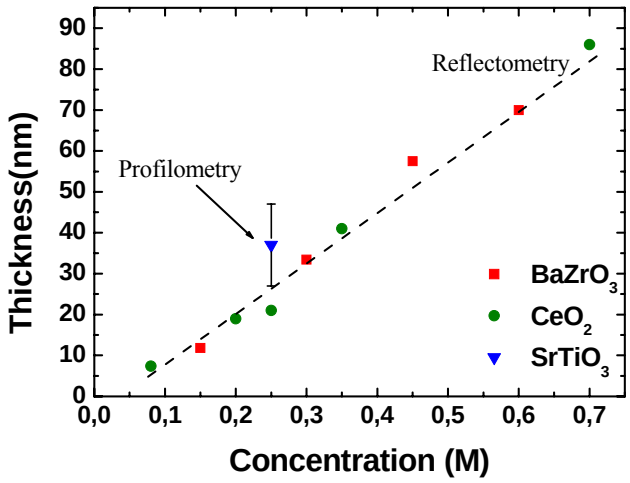

Fig. 5.3: Thickness linear dependence with the concentration of the precursor solution for different buffer layers.

A high error bar, due to the sample preparation, affects the thickness measurement (blue triangle). However, even so the value still fits in the line with the other buffer results.

A solution 0.8 M of BZO precursor has been deposited on MgO single crystal (~90 nm) at the spin optimised conditions and synthesised at 650ºC for 4h in pure Ar C-50. The AFM analysis of this sample, fig. 5.4(a,b,c), indicates that the critical thickness

has been reached and cross type cracks are uniformly distributed. A section of one of these cracks points out that they expand trough the film down to the substrate.

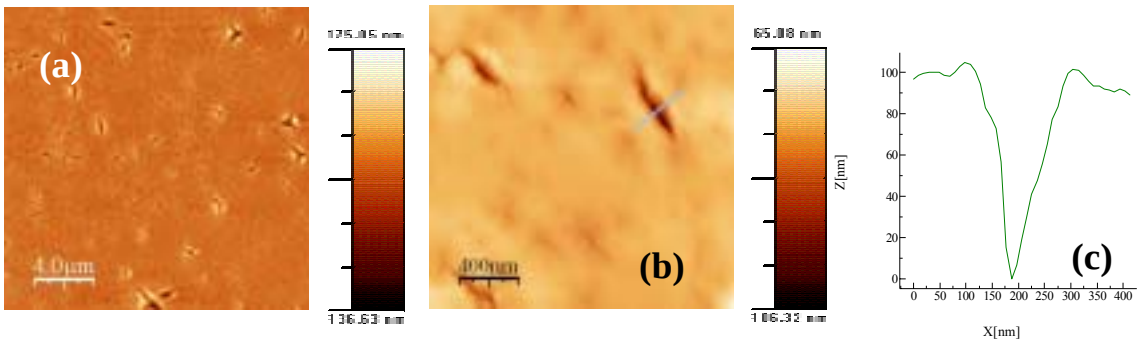

Fig.5.4(a,b,c): AFM analysis of a 90 nm BZO film. Deep cracks homogeneously distributed in the film through it until the substrate. (a)AFM 2·2 mm area scan; (b) 500·500 nm area scan , blue line is a depth measure of a crack; (c) crack profile associated.

Over a certain thickness that depends on the CSD precursors, the tensile stresses that form during the decrease in volume in the pyrolysis can be relieved by the propagation of cracks, F.F.Lange [2]. For many precursors the critical thickness is found to be near the 100 nm [3,4].

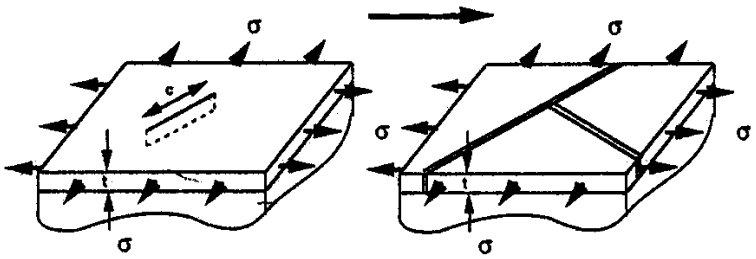

Fig. 5.5: Cracks propagation due to a biaxial tensile stress.

The film before pyrolysis is assumed to be an elastic material with a Young's modulus E and a Poisson's ration ν and subjected to a biaxial tensile stress σ, (fig. 5.5).

The compressive stress can be neglected when the film is very thin with respect to the substrate. A crack can only extend if it reduces the free energy of the system. Lange demonstrated that this condition does not depend on the length of the crack but instead it is true when the film exceeds a critical value:

$$t \geq t_c = 2\, G_c\, E/(Z\, \sigma^2)$$

Where Z is a factor correlated to the crack geometry and G_c is the critical strain-energy release rate.

5.2.2 ROUGHNESS DEPENDENCE WITH SYNTHESIS TEMPERATURE

The roughness evolution with temperature has been analysed for the different systems of our study: STO/MgO, BZO/MgO, and BZO/YSZ. In fig. 5.6(a) three BZO samples of 60 nm synthesised at different temperatures for 4h in pure Ar C-50 have been measured by AFM. Fig. 5.6(b), collects the rms values of 25-30 nm films of STO grown at 650ºc, 750ºC, 850ºC, 950ºC and 1000ºC for 4h in pure Ar.

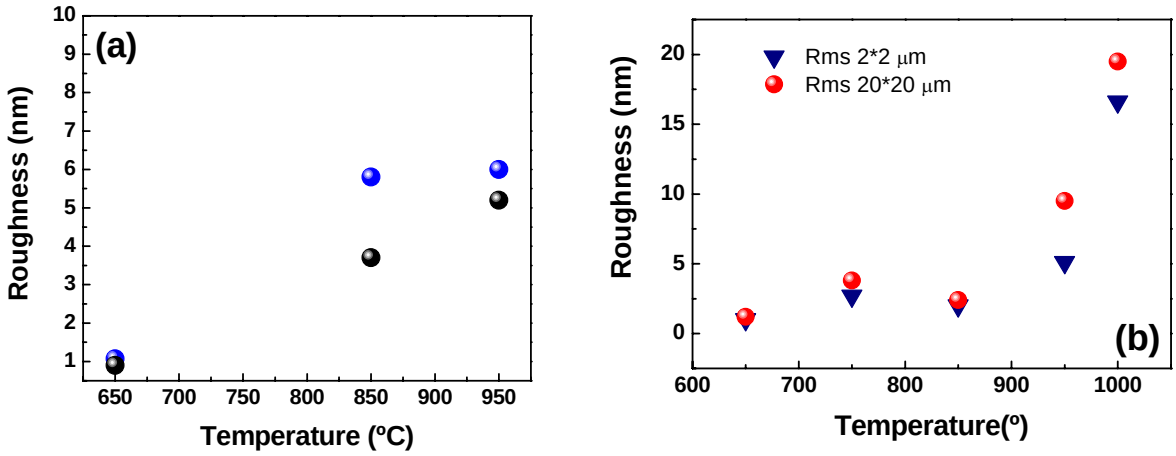

Fig. 5.6(a,b): the Roughness surface values as a function of the synthesis temperature. (a) BZO films, (b) STO ones.

In both systems, the roughness increases with temperature. In the STO films this behaviour is exponential as observed for the ceria thin films see pag.73.

Also the 35-40 nm BZO films on YSZ single crystal confirm this temperature dependence. The blue points in fig. 5.7 are the rms values of the BZO surfaces after growth at 650ºC, 750ºC, 850ºC and 950ºC respectively. The red ones are the rms values obtained on the STO films deposited on each of the BZO buffers, all synthesised at 700ºC.

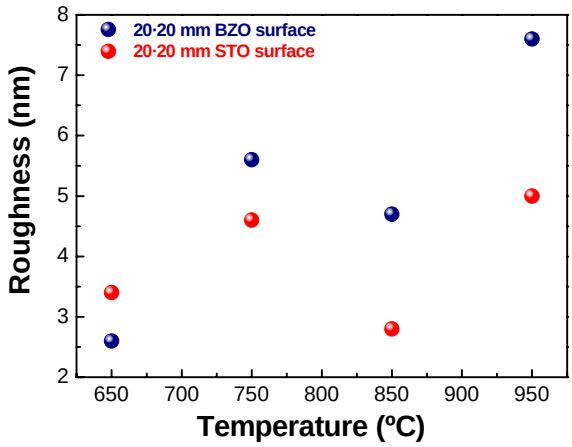

Fig. 5.7: The blue points are the rms values of BZO surfaces synthesised at different temperatures; the reds ones instead, are the values of the final STO buffer layers grown on BZO/YSZ^{SC} samples at 700ºC.

The STO roughness values follow the underlying BZO values. It is interesting to note that when the synthesis temperature of the upper STO film is lower than that of the underlying BZO, its rms value is lower too. This difference increases as the difference in the synthesis temperature. The achievement of flat films by CSD seems to be connected relatively less with the surface roughness of the substrate than to the synthesis temperature, that should be as lower as possible.

5.2.3 STRUCTURES CHARACTERIZATION

$SrTiO_3$/$BaZrO_3$ ON YSZ SINGLE CRYSTAL

Eight samples with a solution concentration of the BZO precursor of 0.3M have been synthesised at different temperatures for 4h in Ar/H_2 atmosphere.

Two by two, the samples have been synthesised at: 650ºC, 750ºC, 850ºC and 950ºC. Fig.5.8 shows the XRD analysis of these samples. The film crystallinity increases with the synthesis temperature, however at 950ºC the (110) orientation of the BZO appears.

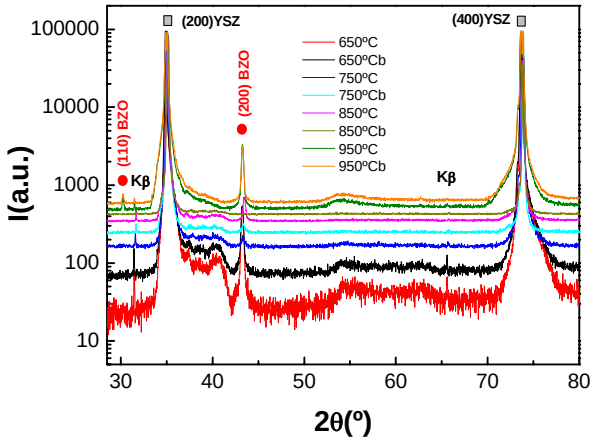

Fig. 5.8: XRD patterns of BZO films synthesised at: 650ºC, 750ºC, 850ºC and 950ºC. The films are only (00l) oriented except for the 950ºC ones where a small amount of (110) orientation has appeared.

On these buffer layers, 25-30 nm STO films have been deposited at 700ºC to study the influence of the underlying different BZO films. Fig. 5.9(a) presents a representative XRD pattern of one of these samples; the out-of-plane analysis of the (200) reflection of the STO is shown in the inset. Only the (00L) orientations for the two materials are visible. Φ scans, fig. 5.9(a,b), indicate an in plane misorientation spread of the STO film of $\Delta\phi$=7.3º.

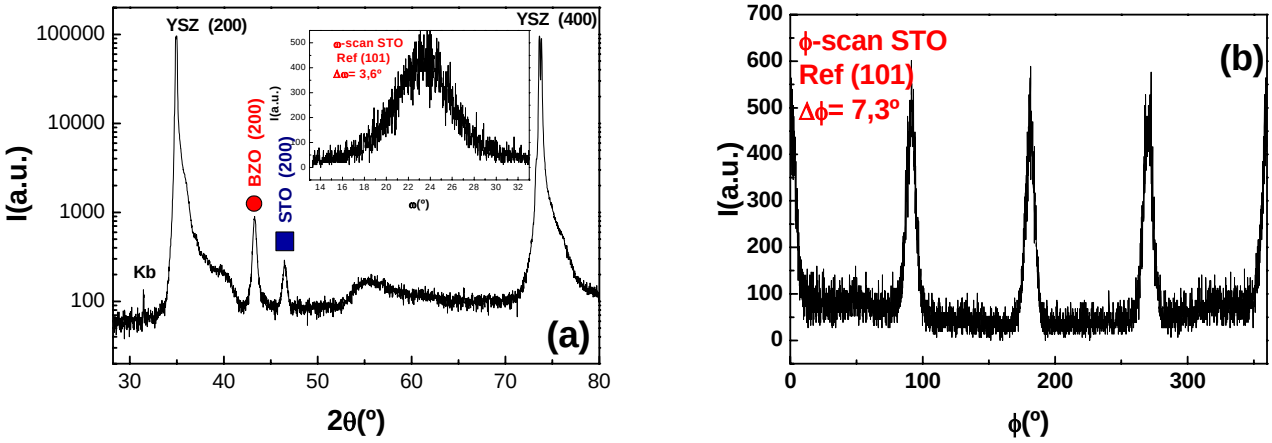

Fig. 5.9(a,b): (a) θ/2θ spectrum of a STO/BZO/YSZ sample, in the inset the (200) ω-scan of STO is presented, $\Delta\omega$= 3.8º. (b) (111) ϕ-scan analysis, $\Delta\phi$= 7.3º.

The ϕ analysis of the reflections (101) of STO, (101) of BZO and (111) of YSZ single crystal in the interval of 35-100 ϕ degree are shown in fig. 5.10. The shift of 45º with respect to the YSZ peak indicates a cube on cube of both films. The calculated mismatch between BZO and YSZ in the cube on cube configuration and the diagonal orientations are: for BZO [100] //YSZ [100] ε = -22.6% and for BZO [110] //YSZ [100] ε = +13.3%. The diagonal configuration should be the most geometrically favoured.

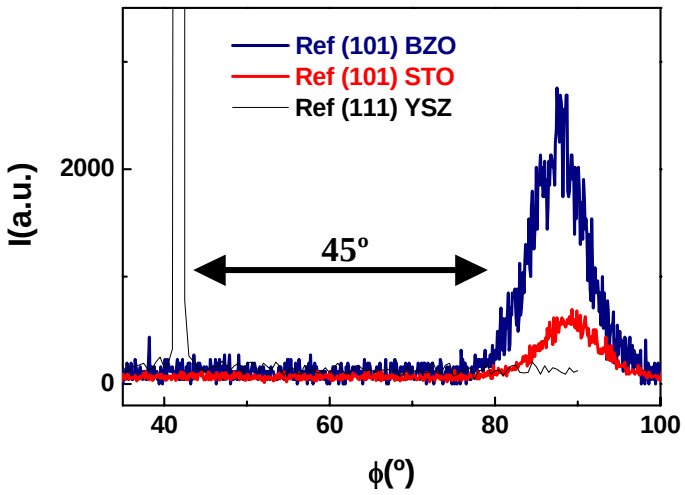

Fig. 5.10: ϕ-scans of a STO/BZO/YSZ sample, pointing out the cube on cube geometry of this system.

In the cube on cube configuration, the BZO grows under tensile in-plane stress while growing with its diagonal parallel to the YSZ cell the stress is compressive. It is worthy to mention that under such very high lattice mismatch, the absolute value of the strain is not significant to the type of epitaxial relationship. Tentatively, we propose that under the tensile stress, the lattice does not have to accommodate any repulsive force, and therefore it is energetically more stable.

$SrTiO_3/BaZrO_3$ AND $SrTiO_3$ ON MgO SINGLE CRYSTAL

The XRD pattern of a typical sample of STO/BZO on MgO single crystal is presented in fig. 5.11. The deposition conditions are the optimized one, the solution concentration of the precursors being 0.25M for the STO and 0.3M for the BZO.

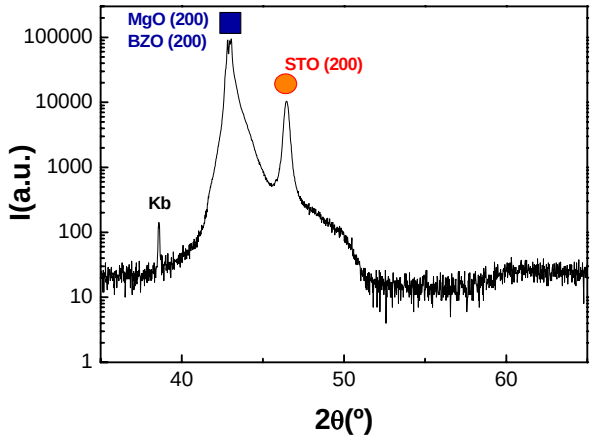

Fig. 5.11: XRD pattern of a STO/BZO/MgO^{SC} sample.

Both films have been synthesised at 700ºC for 4h in pure Ar C-50 gas. The (200) peak of BZO overlaps with the (200) of the MgO single crystal. The good biaxial texture of this sample has been measured in fig. 5.12(a,b). To analyze the out of plane distribution of the BZO film it was necessary to scan the (101) off-plane reflection which is an extinction for the MgO substrate.

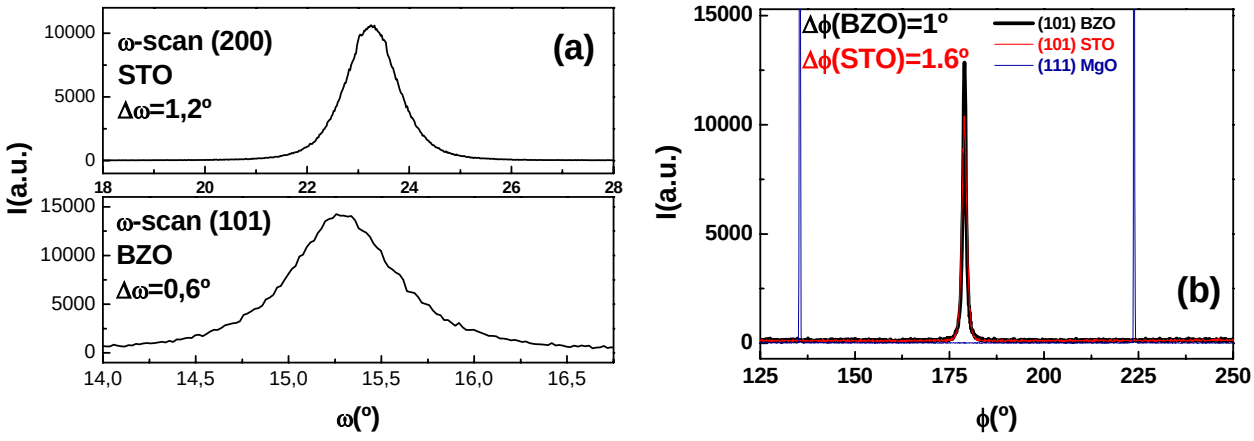

Fig. 5.12(a,b): (a) (200) rocking curves of STO and (101) of BZO . (b) in plane texture of a STO/BZO template grown on a MgO single crystal measured with the (101) and (111) reflections, respectively.

The ϕ-scan indicates a cube on cube epitaxial relationship of the two films with the MgO substrate as expected from mismatch effects.

A series of four samples of 0.25M STO directly grown on MgO have been prepared at different synthesis temperature for 4h in pure Ar: 650ºC, 750ºC, 850ºC and 950ºC. No important differences in the XRD patterns are visible, (fig.5.13). The crystallinity does not increase with temperature as observed before in the synthesis of BZO on YSZ.

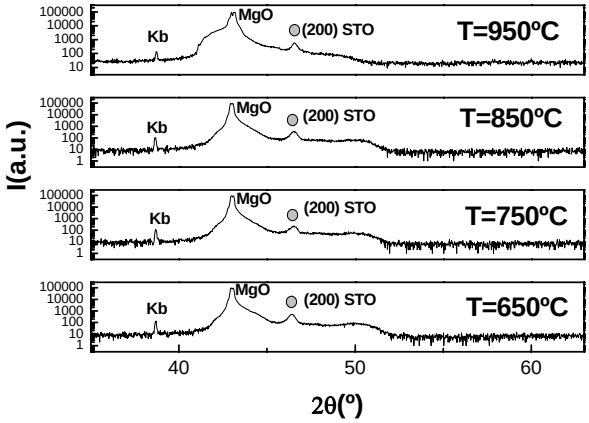

Fig. 5.13: XRD spectra of STO films grown on MgO at 650ºC, 750ºC, 850ºC and 950ºC.

5.2.4 EXPERIMENTAL REPRODUCIBILITY

To check the experimental reproducibility, four samples of STO/BZO on MgO have been prepared at the same synthesis conditions: 0.3M precursor for BZO, 0.25M for STO, and a T_{syn}.of 700ºC for 4h in pure Ar C-50. The out of plane and in plane FWHM of both films are shown in fig. 5.14(a,b).

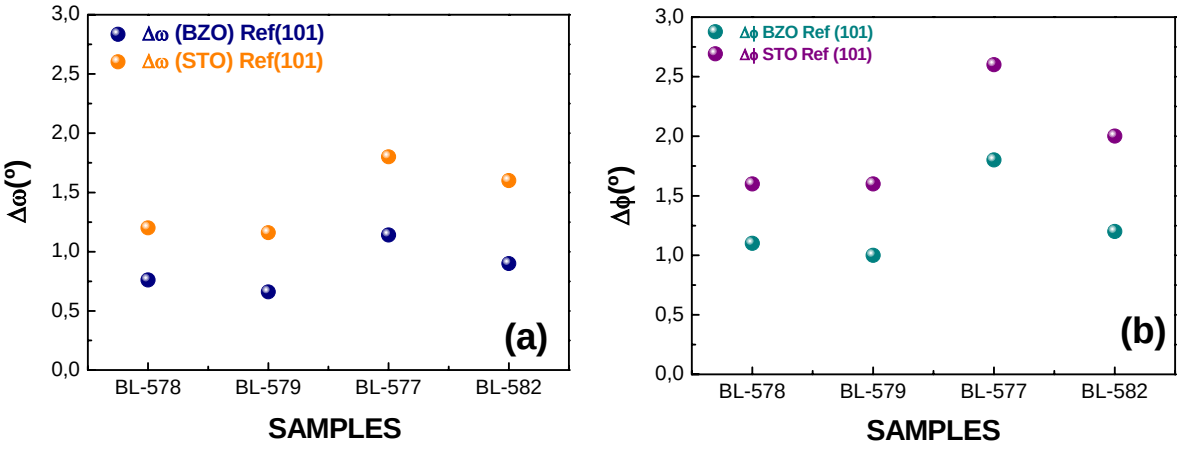

Fig. 5.14(a,b): Four samples synthesised at the same conditions to check the reproducibility of the experimental process. (a) ω-scan and (b) ϕ-scan analysis.

Except for sample BL-577, differences in texture between the other three samples fall within a narrow range, as reported in table 5.1.

TABLE 5.1: Biaxial texture difference in samples grown at the same conditions to verify the reproducibility of the preparation method.

	Δϕ STO (101)	Δϕ BZO (101)	Δω STO (200)	Δω BZO (101)
Difference between the lower and the higher value of FWHM	0.4º	0.1º	0.4º	0.24º

The in plane and out of plane differences in the FWHM values measured for BZO and STO films are maintained near by constant in all the samples, showing how the mismatch between materials affect the misorientation spread of the films.

Indeed, the mismatch (ε) between MgO single crystal and BZO is +1.2%, much lower than the BZO-STO one, +7.3%..

5.2.5 OXYGEN EFFECT ON $BaZrO_3$ GROWTH

Two films of BZO, with the same precursor solution 0.3M, have been deposited on MgO and YSZ single crystals with the following synthesis conditions: 200ºC/h ramp, Tsyn=1000ºC, a dwell of 4 h in static air. Their XRD patterns are presented in fig. 5.15(a,b).

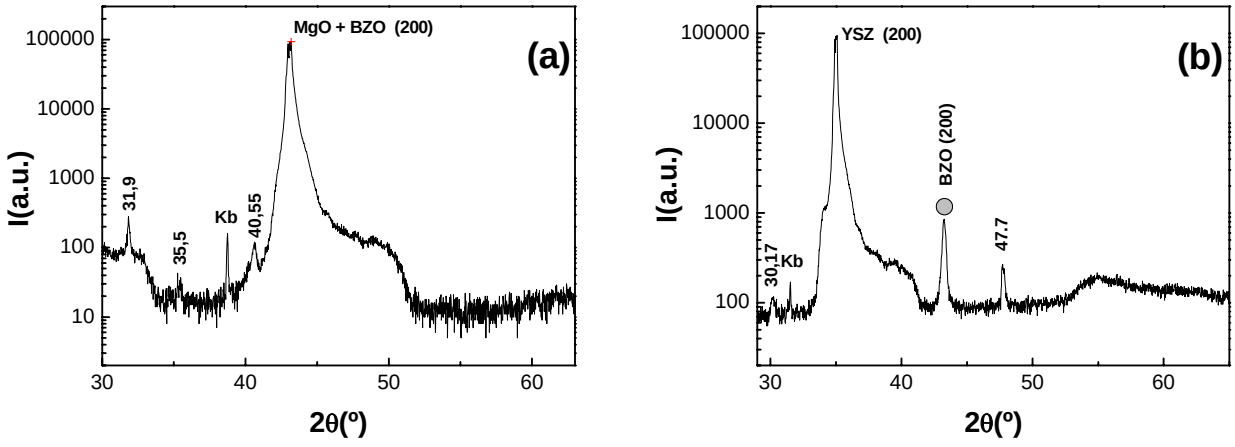

Fig. 5.15(a,b): BZO samples grown in static air on MgO (a), and YSZ(b) single crystals. The XRD patterns indicate the presence of undesired phases, indicated by the presence of non-identified peaks.

The XRD spectra presents in both cases very weak peaks besides those expected for the BZO film, which have not been identified. In fig. 5.16, an AFM image of this BZO film on MgO is shown.

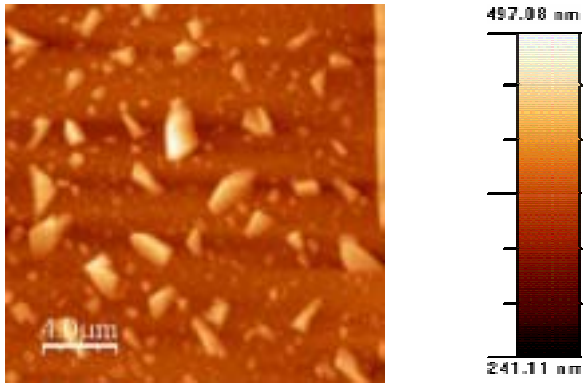

Fig. 5.16: Several irregular shape grains on the surface of a BZO/MgO template grown in air have been observed by AFM analysis.

Grains with irregular shapes are present on the film surface with a homogeneous distribution. Fig. 5.17 is a SEM image of the same sample, after metallization with Au.

SEM image reveals two type of grains. Those found in AFM image and a second type with a stick like shape.

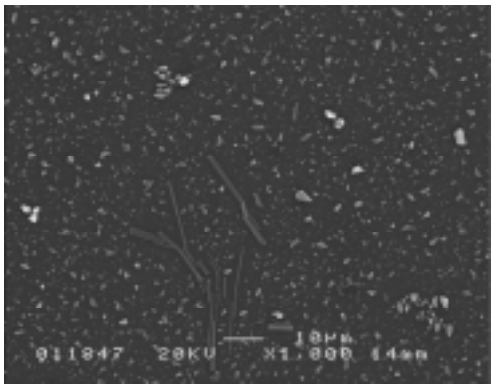

Fig.5.17: Secondary electron image shows the existence of two different types of grains

Line scans of the two grain types have been performed by EDX analysis as shown in fig. 5.18(a,b).

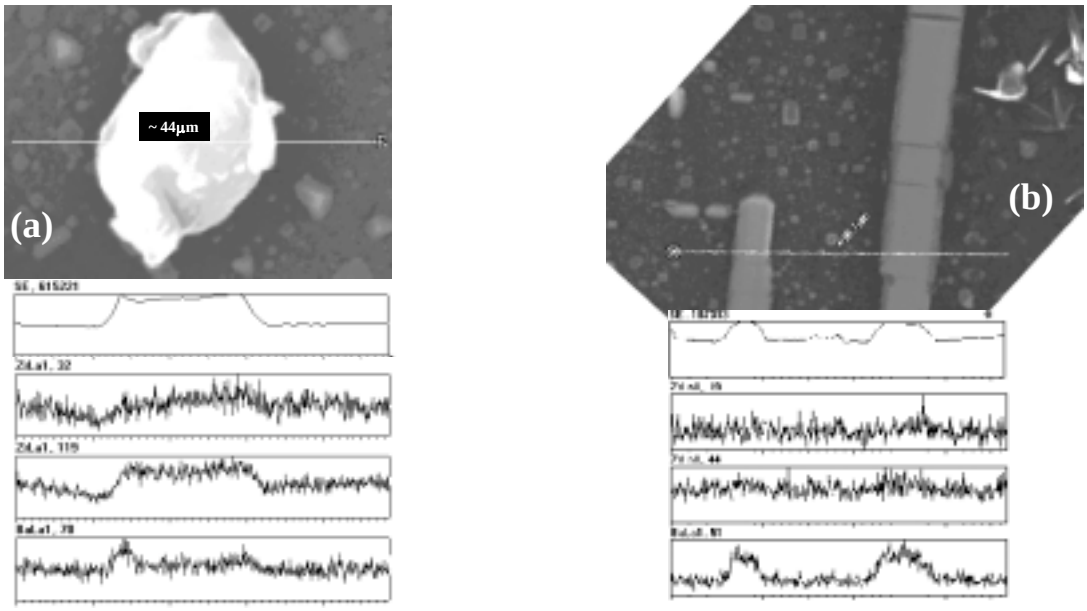

Fig.5.18(a,b): Line scan analysis of two grains with different morphology. (a) The stick in shape grains are reach in barium while the irregular ones (b) in Zr.

The grains with stick like shape have a higher content of barium while the irregularly shaped ones are rich in zirconium as indicated by EDX analysis. The white lines in the fig.5.18 show the zone where the EDX analysis has been performed.

It appears that the oxygen atmosphere favours the formation of Zr and Ba such phases which presumably correspond to the non-identified peaks found in the θ/2θ scans.

5.2.6 SECONDARY GRAIN GROWTH

Grain growth occurs in order to reduce the total energy of a solid [5,6].
BZO and STO films have been synthesised on MgO and YSZ single crystals at two different temperatures: 650º and 950ºC for 4h. The thickness of BZO films was in the range of 35-40 nm while the STO ones between 25-30nm. Fig. 5.19 shows AFM images of the six studied samples.

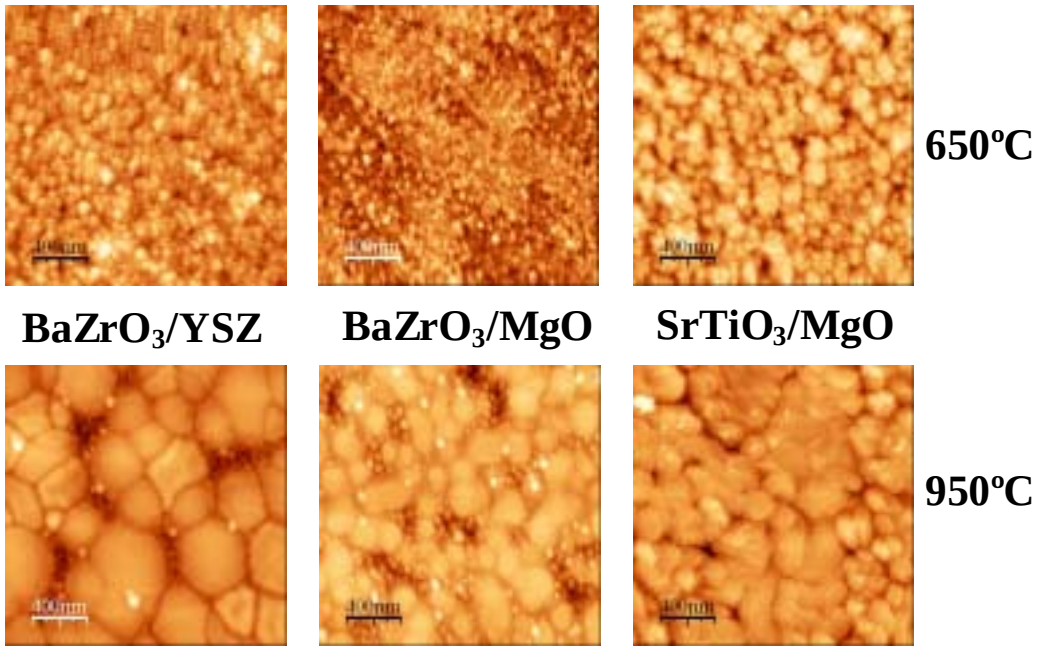

Fig.5.19: AFM analysis of three samples synthesised at 650ºC and three at 950ºC reveals secondary grain growth. The thicker BZO films exhibit a bimodal size distribution suggesting that the growth of the film is uncompleted.

At 650ºC the three films are all in the normal grain growth regime while the others three ones grown at 950ºC indicate a secondary grain growth. For the STO sample grown at 950ºC, the grain growth after 4h seems to be complete. The AFM images of the BZO samples grown at the same synthesis temperature indicate the presence of small grains that have not been "absorbed" yet by the abnormal grains. The double grain size distribution of the thicker BZO films is consistent with a secondary grain growth regime, and also suggest that the growth of the films is incomplete. On the other hand, for the thinner STO film, the homogeneous size distribution suggests that the growth is completed. Again, these observations indicate that grain growth stagnation is achieved faster in thinner films, i.e., grain growth stops when they impinge with other grains with the same favourable surface energy.

5.3 FILM BIAXIAL TEXTURE

The in plane texture of the 30-40 nm of BZO films grown at different temperatures, 650ºC-750ºC, on YSZ and MgO single crystals have been compared in fig. 5.20. The difference in mismatch, ε(BZO/MgO)=-0.6%% and ε(BZO/YSZ)= -22% of the two systems is reflected in the Δϕ values obtained.

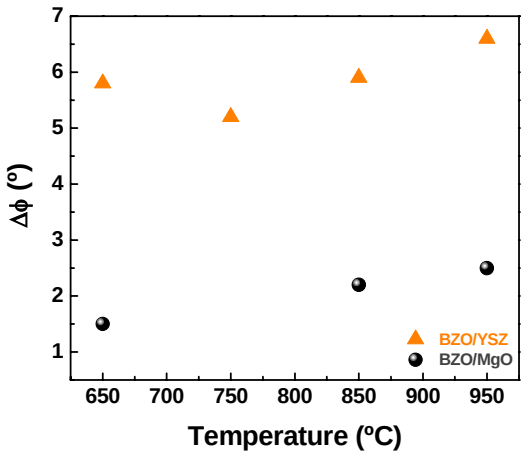

Fig. 5.20: Study of the mismatch influence on the film texture. BZO films have been grown at the same conditions on MgO and YSZ single crystals. The in plane analysis has demonstrated a better texture for the system with the lower mismatch.

The mean FWHM value of ϕ is 2.1º for the BZO/MgO system and 5.9º, almost three times higher for the BZO/YSZ. This difference is mainly explained by the mismatch.

In the other cases, as reported in table 5.2, the differences in texture quality have a more complex explanation, that goes beyond mismatch arguments, that probably are associated with chemical or structural affinity.

STO and BZO buffer layers have been synthesised all at the same conditions, 0.3M for BZO and 0.25M for STO films at a temperature of 700ºC for 4h on different substrates.

TABLE 5.2: Mean FWHM of ϕ peaks for three different samples grown at 700ºC for 4h.

SYSTEMS	STO/BZO/MgO	STO/MgO	STO/BZO/YSZ
Δϕ (BZO)	1.1º	-	5.8º
Δϕ (STO)	1.6º	3º	7.3º

5.3.1 BIAXIAL TEXTURE DEPENDENCE WITH THE FILM SYNTHESIS TEMPERATURE

As already seen there is a clear relation between the increase of synthesis temperature and the increase of the film surface roughness. Hence, we analyze the effect of T on the texture quality of the CSD-films.

The FWHM of the in plane (circles) and out of plane texture (squares) of the four samples of STO (25-30 nm thick) grown at different temperatures are shown in fig. 5.21(a). The surface roughness of these samples obtained by AFM 20·20 μm scan have been represented by triangles. The ϕ–scans of the (101) reflection of the STO films grown on MgO^{SC} at different synthesis temperature are presented in fig. 5.21(b).

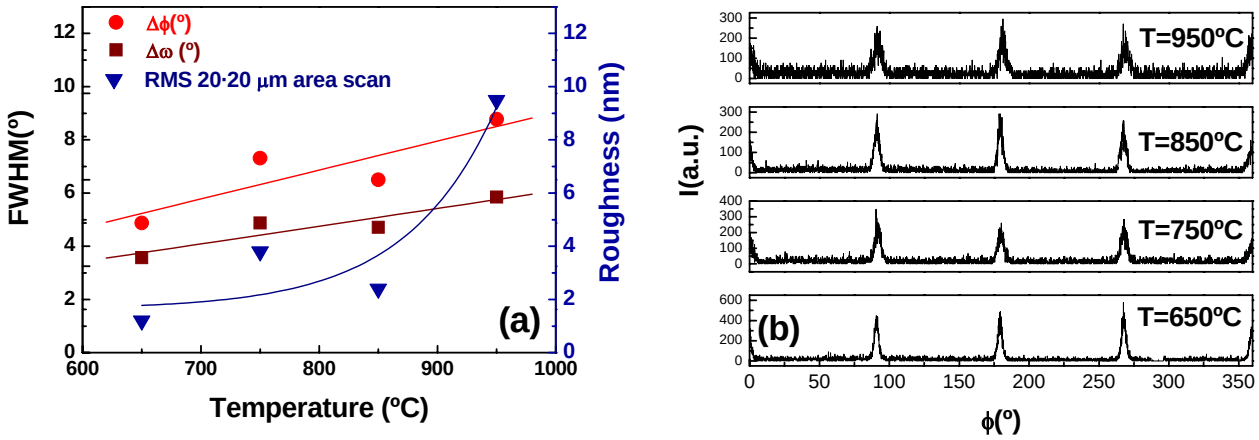

Fig. 5.21(a,b): (a) Biaxial texture dependence with synthesis temperature of a STO films on MgO. (b) (111) ϕ-scan analysis of the STO samples.

The difference in FWHM between the sample synthesised at 650ºC and the 950ºC one is 2.4ºin ϕ and 1.4º in ω.The clear increase of the STO in and out of plane misorientation with temperature seems to follow the same surface roughness behaviour.

Another example is the texture analysis of the 35-40 nm films of BZO grown on YSZ^{SC} in the same range of temperatures and presented in fig. 5.22(a,b).

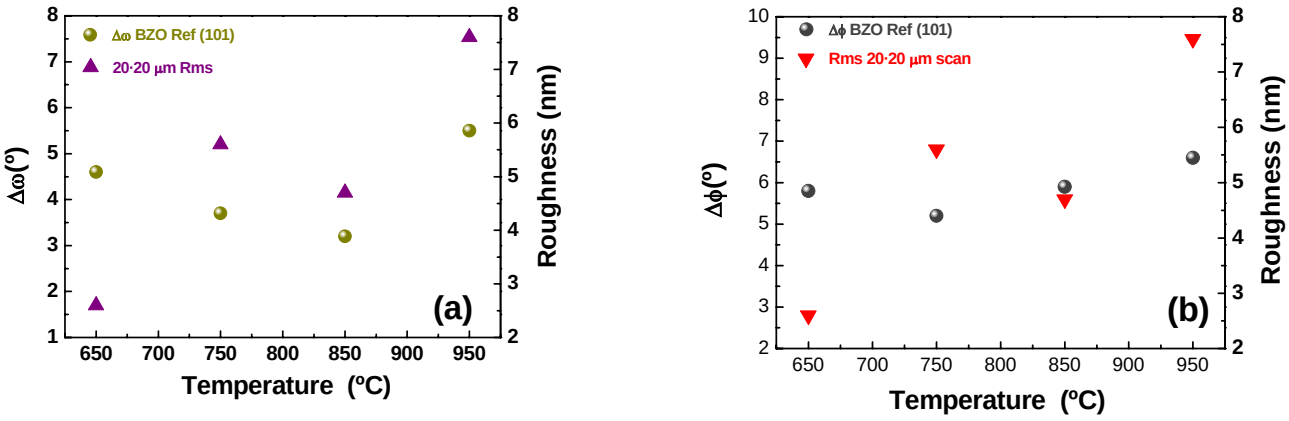

Fig. 5.22(a,b): Study of the biaxial texture and roughness as a function of synthesis temperature for the BZO system. (a) Δω, (b) Δϕ.

The FWHM difference in ω and ϕ between the 650ºC and the 950ºC samples is 0.9º and 0.8º, respectively. The worsening of the biaxial texture is not so important as in the case of the STO on MgO single crystals observed above.

This texture-roughness relation in CSD films, can tentatively be correlated, when the synthesis temperature increases, to the growth of surface grains exhibiting a lower surface energy. In secondary growth regime, minimisation of the total energy of the film may lead to growth of grains with orientations that do not minimize neither the interface energy nor the surface one, but constitute a compromise between both [5]. Probably, in STO and BZO growth the surface energy is minimised for grain orientations different from the epitaxial one. The result is a worsening of the films texture.

5.4 CONCLUSIONS

The solution preparation and the deposition conditions for STO and BZO on MgO and YSZ have been optimised. The secondary grain growth seems to be the predominant regime up to a temperature near 950ºC for a film thickness of 25-40 nm.

This type of growth has two undesired effects, the first is an increase of the film surface roughness connected with grain size, and the second, a worsening of the in plane and out of plane texture. This is the reason way it is necessary to maintain the synthesis temperature as low as possible. At 650ºC nevertheless the film is already textured but in some cases we found an anomalous disorientation of the films that should be attributed

to an incomplete process of grain re orientation, (recall that the film nucleates under homogeneous regime for STO and BZO, the optimum temperature has been fixed in 700ºC.

The matching effect and the structural and chemical affinity between the different materials make the STO/BZO/MgO as the most promising system for the YBCO superconducting deposition. In optimum conditions a $\Delta\phi=1.6^{o}$, the lower for this kind of buffer layers, has been achieved.

It has been demonstrated the importance of controlling the film thickness under its critical value to avoid the formation of cracks.

Two main differences between these buffer layers behaviour and CeO_2 have been found. Working in reducing conditions does not affect the epitaxial growth of STO and BZO films as in the CeO_2 synthesis. In the perovskite film, the secondary grain growth regime may induce a worsening of the in plane and out plane texture of the films. In the CeO_2 synthesis, on the other hand, the films are textured only in a secondary grain growth regime.

REFERENCES

[1] M. Coll PhD Tesina Universitat Autonoma Barcelona, (2005).

[2] F.F.Lange. *Science, **273**, 903-909, (1996).*

[3] J.J.Cuomo, D.L.Pappas, J.Bruley, J.P.Doyle, K.L.Saenger. *J.Appl.Phys.**70**, 1706, (1991).*

[4] D.L.Pappas, K.L.Saenger, J.J.Cuomo, R.W.Dreyfus, *Ibid. **72**, 3966, (1992).*

[5] C.V.Thompson, and J.Floro, *J.App.Phys., **67**, 4099, (1990).*

[6] H.-J.Kim and C.V.Thompson, *J.App.Phys., **67**, 757-767, (1990).*

Chapter 6

DEPOSITION OF THE OPTIMISED BUFFER LAYERS ON METAL SUBSTRATES

6.1 NiO(SOE)/Ni SUBSTRATE

The oxidation of textured nickel is a tricky process. In fact the oxide forms easily and uncontrollably in a very large range of temperatures. Only a careful method allows to obtain flat and biaxially textured self oxidised NiO films, NiO(SOE) [1]. In the course of this research, many different batches of NiO prepared in Cambridge have been used, at any rate in the present work only the results obtained with the better batches will be presented. In Table 6.1 the texture and roughness of different NiO substrates is given.

TABLE 6.1: Different NiO substrates biaxial texture and surface roughness.

	Δω	Δϕ	RMS(nm)	P-V(nm)
NiO^{SOE}/Ni	5.5º	8º	15.2	32
NiO^{SOE}/Ni Best batch	4.3º	6º	10.3	25

The ϕ-scan of (111) reflections of the Ni and NiO(SOE), (fig. 6.1), measured on the same substrate, show that the NiO cell grows along the diagonal of the nickel one, as indicated by the fact that the four ϕ-peaks of Ni are shifted by 45º with respect to NiO ones.

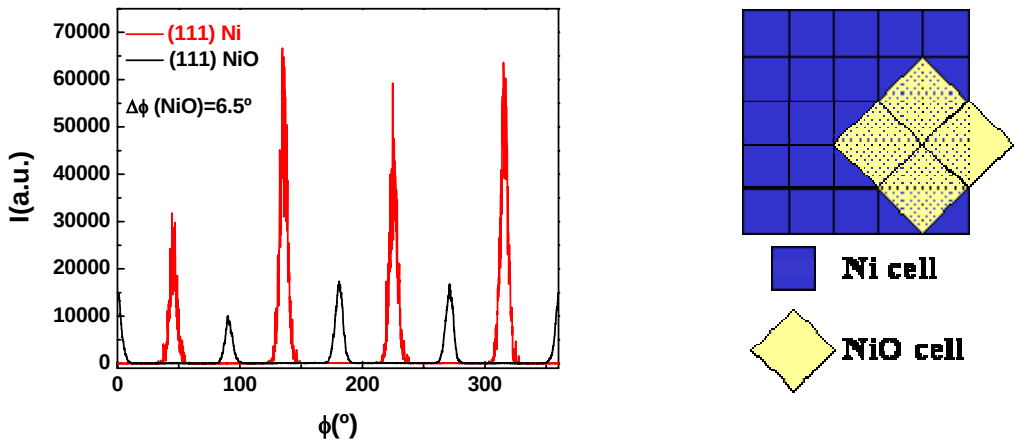

Fig. 6.1: ϕ-scan of the (111) Ni and (111) NiO reflections. The 45º distance between each series of four peaks indicates a diagonal growth of the NiO cell with respect to the Ni one.

Theoretically the lattice mismatch for the cube on cube growth should be the more favourable: +16% versus -18% of the diagonal configuration. Hence again, the orientation is that corresponding to a tensile stress, even at the cost of absolute strain. In fact both types of configurations [2,3], diagonal and cube on cube, have been experimentally found as confirmed by J.Evetts, (private communication). Fig. 6.2(a) is a SEM image of the NiO ; the surface looks like dense and with pores not larger than 200nm, as determined by the profile in AFM analysis fig. 6.2(b).

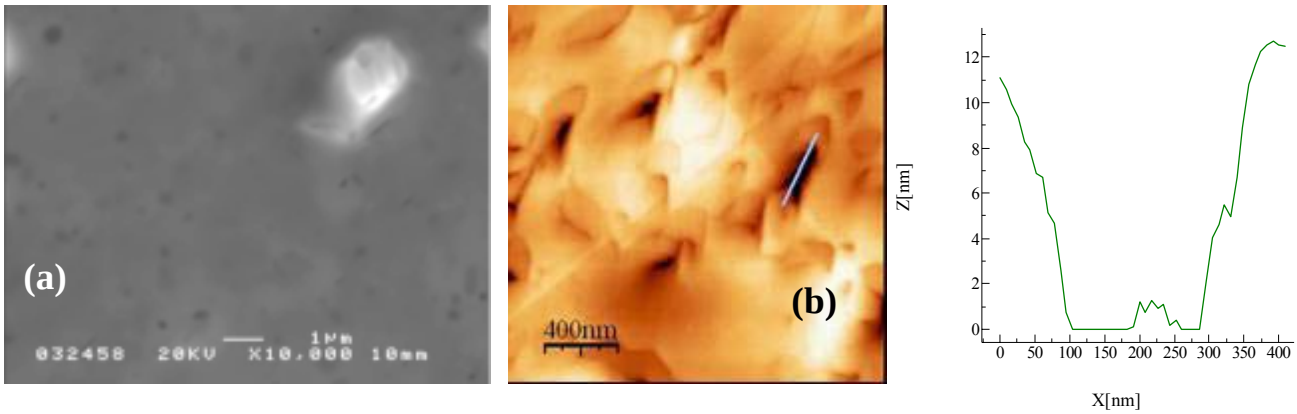

Fig. 6.2(a,b): SEM image of the surface of a NiO(SOE) substrate (a). AFM analysis of the same substrate confirms the presence of pores of 200-300 nm size.

As the first tests of YBCO deposition on STO/MgO^{sc} (the model simulating the NiO behaviour) have not given good results, we tested on NiO(SOE) only the more promising STO/BZO architecture. Actually the misfit STO/NiO is -7 % instead of 0.38% in the case of BZO/NiO and the misfit between STO/BZO is -7.37%. To grow STO directly on NiO or on BZO it is necessary to overcome near by the same stress barrier, however at a parity of mismatch the STO seems to have more affinity for another pervskite structure than for a rock salt one.

We started depositing BZO with the same precursor solution at a concentration of 0.3M. The four substrates of NiO(SOE)/Ni used were part of the same batch. The BZO synthesis conditions for the four samples were: 60ºC/h up to 250ºC, dwell of 30 min., a second ramp up to 700ºC followed by a dwell of four hours. They have been prepared at the same time and in the same oven to reduce the irreproducibility. An upper film of STO with a precursor solution of 0.25M has been deposited on the BZO films at the same conditions except for the synthesis temperature: 600ºC, 700ºC, 800ºC, 900ºC. In both processes a pure Ar atmosphere has been used. The Ar/H_2 one could reduce the NiO buffer. In fact using a reducing atmosphere (Ar/H_2 5%) the textured NiO was totally destroyed after a treatment of 4h at 700ºC as presented in fig. 6.3.

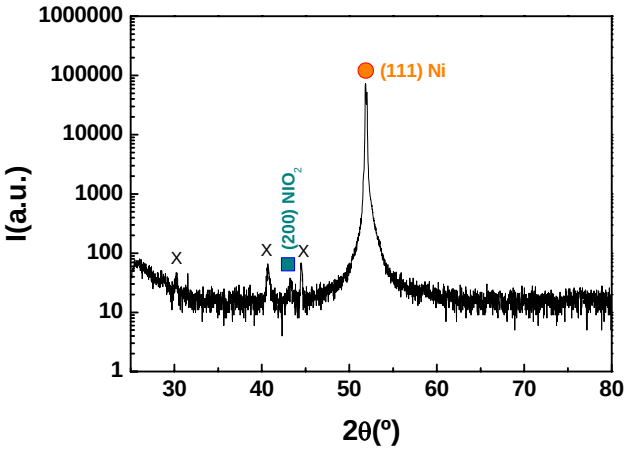

Fig. 6.3: XRD pattern of a substrate of NiO(SOE)/Ni after its reduction in Ar/H_2 atmosphere.

The ϕ-scans of both films (BZO, STO) were measured after the STO synthesis (fig. 6.4(a)). The (101) reflections were selected for the in plane analysis. Since the BZO and NiO(SOE) have nearby the same cell parameter, the (101) reflection is ideal to study only the in plane texture of the BZO film because it is an extinction for the NiO structure. The FWHM values of the BZO samples all synthesised at 700ºC but post annealed during STO growth, green points, get higher with increasing the STO synthesis temperature, from a value of Δϕ~8º (T_{syn}=700ºC) up to Δϕ~14º (T_{syn}=900ºC). If now we focus the attention on the STO FWHM, blue points, it is even more apparent that increasing the synthesis temperature the in-plane texture gets worse (Δϕ~6 .at 700ºC up to Δϕ~18º at 900º).

This behaviour as commented in chapter 5 may be attributed to secondary grain growth, typical of these CSD processes. The sample synthesised at 600ºC has a Δϕ~10º larger than the 700ºC and 800ºC ones, probably because atom mobility is not high enough to achieve the optimum texture in the allowed time.

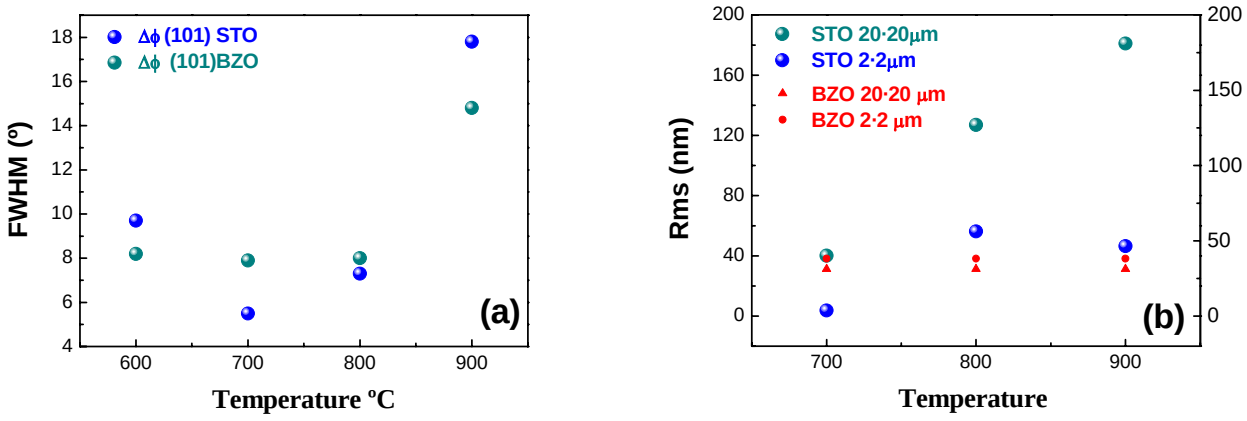

Fig. 6.4(a,b): (a) FWHM of the phi (101) reflections of STO and BZO of four double buffer samples grown on NiO(SOE)/Ni substrates. The BZO buffers have been all grown at 700ºC while the STO at: 650ºC, 750ºC, 850ºc and 900ºC respectively. (b) Dependence of the surface roughness with the synthesis temperature.

The surface roughness of STO films follow the typical dependence on temperature as shown in fig.6.4(b). The roughness value increases with temperature has clearly shown by rms measurements in 20 by 20 μm scan. The red points are the rms reference of the underlying BZO films. The 2·2 μm scan area is not representative of the roughness of the sample but is useful to study more in detail the change in grain size. The secondary grain growth is strictly correlated with the increase of the grain size with temperature. The AFM images of 20·20 μm, 2·2 μm and 500·500 nm area scans of these STO four samples are presented in fig. 6.5. It is evident the coarsening effect in which the grains with minimum surface and interface energies are favoured and grow in size in detriment of those with higher energies. The surface of one of the BZO samples synthesised at 700ºC is also included.

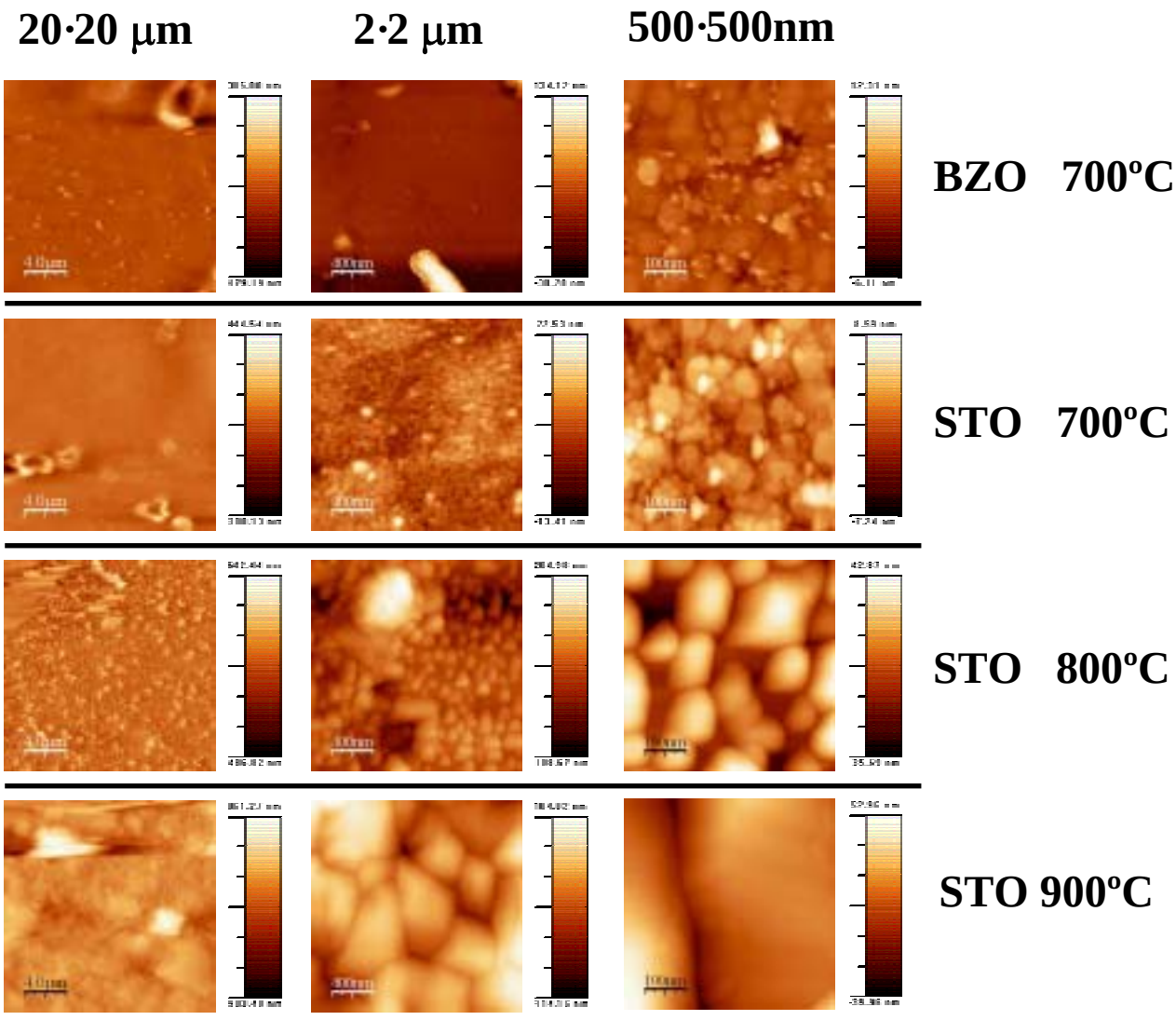

Fig. 6.5: AFM images of the STO surfaces of STO/BZO/NiO(SOE)/Ni samples. AFM image of the BZO surface after synthesis at 700ºC in pure Ar is also shown.

All the STO films have the same thickness, 25-30 nm. The secondary grain growth in the one synthesised at 900ºC has already stopped after 4h confirming the same behaviour observed for STO buffer on MgO single crystal, (chapter 5 pag.122). The STO growth on BZO/NiO(SOE)/Ni also obey to an Arrhenius type relationship $\langle r\rangle^2 - \langle r_o\rangle^2 = \alpha t$, indicating a thermally activated 3D growth, as for CeO_2 film chapter4.

Fig. 6.6 shows a plot of 2ln<r> against 1/T. The good fit (R=0.984).

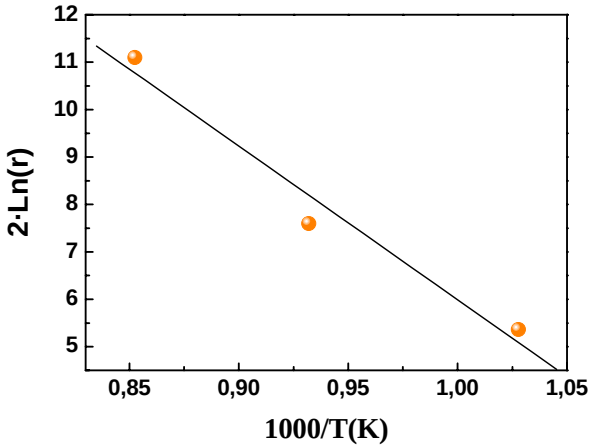

Fig. 6.6: Grain size dependence with synthesis temperature of STO films grown on BZO/NiO(SOE)/Ni.

From the slope of this plot, a value of Q=2.8 eV is obtained

To check the reproducibility of this process, four new samples of STO/BZO/NiO(SOE)/Ni have been prepared. The synthesis conditions for the two buffer layers BZO and STO were the same: 60ºC/h till 250ºC dwell of 30 min., a second ramp up to 700ºC and a dwell of 4h. The results of in-plane texture are presented in fig. 6.7.

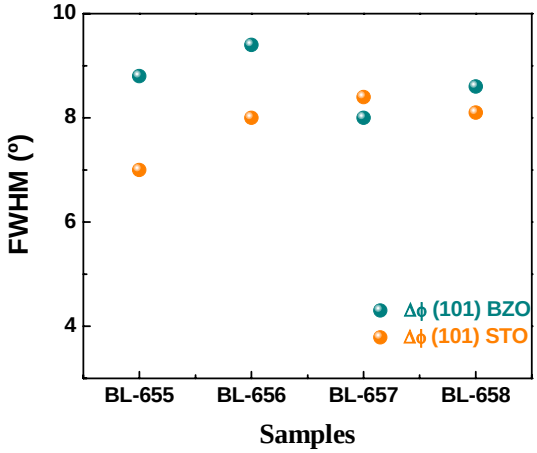

Fig. 6.7: In plane texture analysis of four STO/BZO/NiO(SOE)/Ni samples synthesised at the same conditions to verify the process reproducibility.

The FWHM of STO and BZO is between 7º and 9º. The reproducibility is not high but as found in the first set of experiments, the STO values follow the same trend as those of the

underlying BZO ones. Moreover it is important to emphasize that the texture of the upper STO film improves the BZO one in all the samples except for the BL-657, where, on the other hand the difference between the STO and BZO ϕ–FWHM is less than 0.5º. This behaviour has been also observed in other multi-layers grown by CSD on metal substrates, as we will see beyond.

The XRD analysis of our best sample of STO/BZO/NiO(SOE)/Ni is presented in fig. 6.8(a,b). In the θ/2θ spectrum, only the STO peak is visible because the BZO one overlaps with the (200) peak of the nickel oxide. A small amount of (111) Ni appears probably due to a recrystallization.

Four peaks 90º apart are observed, baring witness of the occurrence of a unique orientation in-plane domain. Comparison with the corresponding (101)-BZO ϕ-scan indicates a cube-on-cube epitaxial relationship as expected by the lower calculated mismatch (-7.37%) of this configuration, with respect to the diagonal one, with ε=24%.

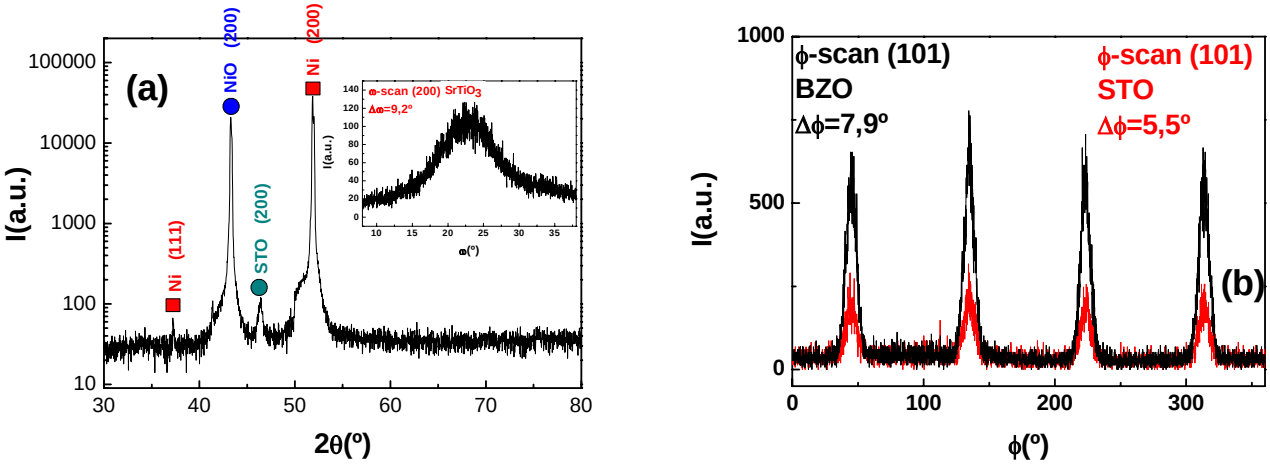

Fig. 6.8(a,b): (a) XRD pattern of a sample of STO/BZO/NiO(SOE)/Ni. In the inset the rocking curve of the (200) reflection of STO is shown. (b) ϕ-scan of the (101) reflections of STO and BZO films.

The optimised process for STO and BZO on NiO has been fixed at a synthesis temperature of 700ºC, dwell time of 4h and an atmosphere of pure Ar-C 50. These values are optimum for the particular thickness of 25-30 nm for STO and 35-40 nm for BZO. The best sample obtained, with an in plane texture of the top STO layer of 5.5º, is encouraging in view of deposition of the YBCO films.

6.2 YSZ(IBAD)/SS SUBSTRATES

The biaxial texture of the YSZ deposited by IBAD is fundamental to obtain an optimum template to deposit the YBCO superconductor film. During this work we have received YSZ(IBAD)/SS substrates with different degrees of texture, as reported in table 6.2.

TABLE 6.2: Biaxial texture characteristics of the different YSZ(IBAD)/SS batches used in this work.

BATCH		Δω	Δϕ
I	**YSZ(IBAD)/SS (tape)**	6.0°	16°
II	**YSZ(IBAD)/SS (tape)**	6.3°	13.4°
III	**YSZ(IBAD)/SS (tape)**	5.6°	11.4°
IV	**YSZ(IBAD)/SS (tape) Best batch**	5º	9.5º

We have investigated the synthesis of CeO_2 and the double buffer STO/BZO as their preliminary results on the model of YSZ single crystal have been the more promising ones. Minor adjustments of the process parameters have been necessary due to the complexity of the YSZ(IBAD)/SS substrates. The first batches (I, II and III) of YSZ(IBAD)/SS [3] with a high in plane disorientation , often presented anomalous surface grains. In the AFM (image 2·2 μm area scan) and in SEM images, (fig. 6.9(a,b)), of one substrate from YSZ/SS batch II, some anomalous grains larger than 1 μm, due to the IBAD process, are visible. Probably many of these grains will be not recovered completely by thin buffer layers that we deposit (~ 25-40 nm). As the grains density in some substrates is very high, it is difficult to know which will be the growth effects on the films.

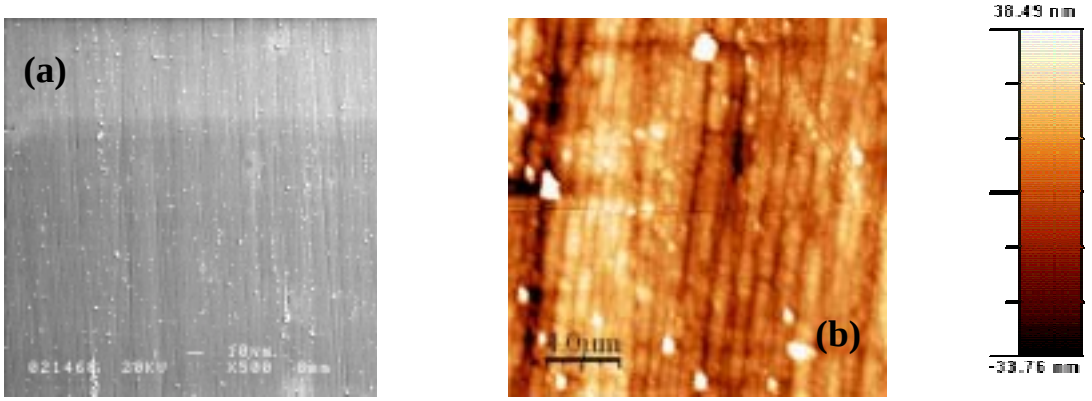

Fig. 6.9(a,b): SEM image of the surface of a YSZ(IBAD)/SS substrate; several grains oriented in the direction of the re-sputtering beam of the (IBAD process), are observed (a). AFM images confirm the same surface morphology.

6.2.1 GROWTH OF CeO_2 FILMS ON IBAD-DEPOSITED YSZ TEMPLATES ON STAINLESS-STEEL TAPES

In table 6.3 the optimised parameters of the synthesis of CeO_2 films in Ar/H_2 and directly in air have been resumed.

TABLE 6.3: Experimental parameters of the synthesis of the CeO_2 buffer layers on YSZ single crystal. In the right column the best parameter values are presented.

	Experimental range	**Best parameters Ar/H_2**	**Best parameters Static Air**
Precursor Solution Concentration	0.08M-0.9 M	0.25 M	0.25 M
Deposition Acceleration	1000-5000 rpm/s	3000rpm/s	3000rpm/s
Deposition Rate	3000-7000 rpm	6000 rpm	6000 rpm
Synthesis Temperature	650-1300 °C	750 °C	1000 °C
Dwell Time	0.25-16 h	4 h	8 h
Oven Atmosphere	Pure Ar,Ar/H_2,O_2,Static Air	Ar/H_2 5%	Static Air

The synthesis parameters of the best experiments on YSZ single crystal in Ar/H_2 were: 0.25M, deposition rate of 6000 rpm, acceleration of 3000 rpm/s, synthesis temperature of 750°C and dwell time of 4h. The samples prepared at these conditions do not present textured growth as sown in fig. 6.10(a). The best textured cerium oxide on YSZ(IBAD)/SS has been obtained changing the synthesis temperature to 900°C. In the XRD analysis of this sample only the (00L) cerium oxide peaks are present fig. 6.10(b).

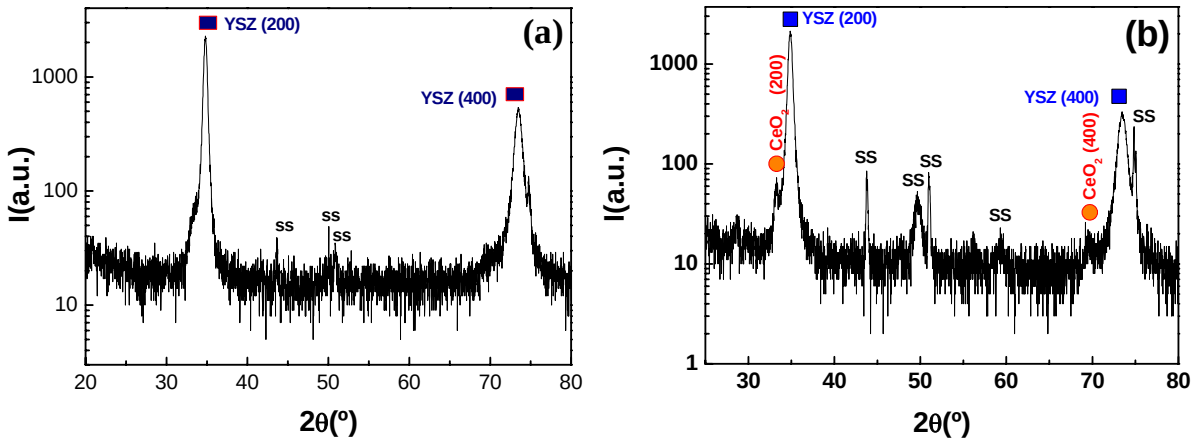

Fig. 6.10(a,b): θ/2θ-scan of a CeO_2 buffer layer grown on a YSZ(IBAD)/SS substrate; (a) synthesised at 750ºC and (b) at 900ºC, both for 4h in Ar/H_2.

The tendency of all the samples prepared in Ar/H_2 is that the cerium oxide grows up maintaining the texture quality of the YSZ(IBAD)/SS substrate . The in-plane and out plane values are similar to the substrate ones and in this particular sample are respectively $\Delta\phi$=10º and $\Delta\omega$=8º, (fig. 6.11(a,b)).

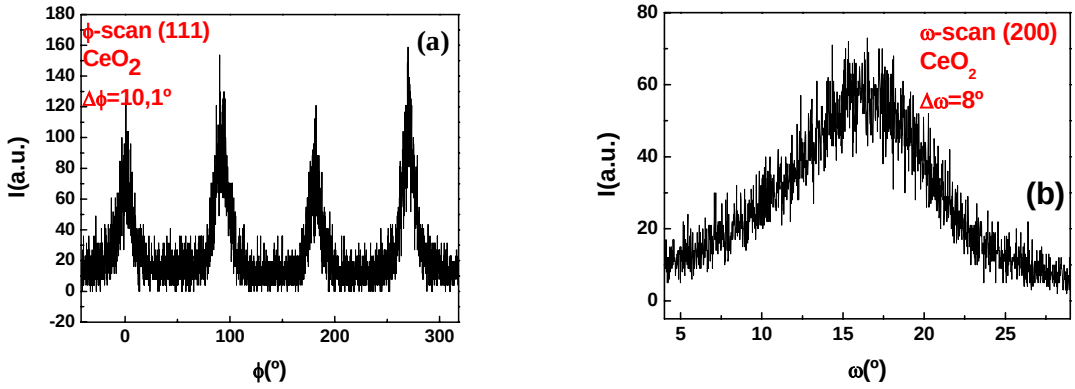

Fig. 6.11(a,b): (a) ϕ-scan of the (111) reflection, $\Delta\phi$= 10º. (b) Rocking curve of the (200) reflection of CeO_2, $\Delta\omega$=8º.

The thin film texture is clearly conditioned by the metal substrates used. A ϕ–scan FWHM value of more than 9º is too high for the YBCO superconducting properties and no high current densities could be obtained. One possibility is trying to increase the texture of the cerium oxide on the YSZ(IBAD)/SS. Since growing the YSZ on the Stainless Steel with a $\Delta\phi$<9º is not easy, the second option could be the self induced epitaxy. It has been reported [4,5] that the cerium oxide grown by PLD, above a thickness of 300 nm, improve its texture with $\Delta\phi$ <5º. No results on CSD CeO_2 self-induced-epitaxy have been reported yet, but new experiments are in progress right now.

The AFM analysis of a CeO_2/YSZ(IBAD)/SS sample grown at 800ºC for 4h in Ar/H_2 (5%) is presented in fig. 6.12.

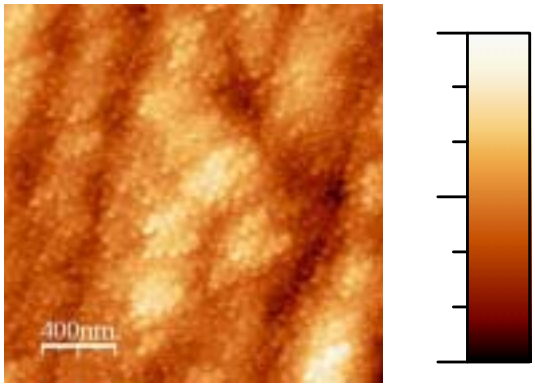

Fig. 6.12: AFM analysis of the ceria surface of a sample grown at 800ºC for 4 h in Ar/H_2. The grain size is particularly small.

The surface is quite flat with a rms~5.3nm, compared with YSZ(IBAD)/SS, in the 2 μm by 2 μm area scan and the grain size is small.

The rms value in the 20·20 μm scan could vary in the range of 10-15 nm, similar to the roughness of the YSZ(IBAD)/SS substrate (see Table 3.1 pag.52).

6.2.2 CeO_2 GROWTH IN OXIGEN ATMOSPHERE

In order to grow a completely textured CeO_2 film in a single step, we attempted its direct growth in air, (see chapter 4). The best condition to grow ceria on a single crystal was: a precursor solution of 0.25M, 6000rpm spin rate, 3000rpm/s spin acceleration, a thermal ramp of 1500ºC/h, a T_{syn} of 1000ºC and a dwell of 8h in static air. The first results using YSZ(IBAD) on stainless steel resulted in the destruction of the metal tape. Fig. 6.13 shows a XRD spectrum of a sample prepared at these conditions. The steel is still resistant enough to oxidation as indicated by the presence of numerous peaks of the oxidised species.

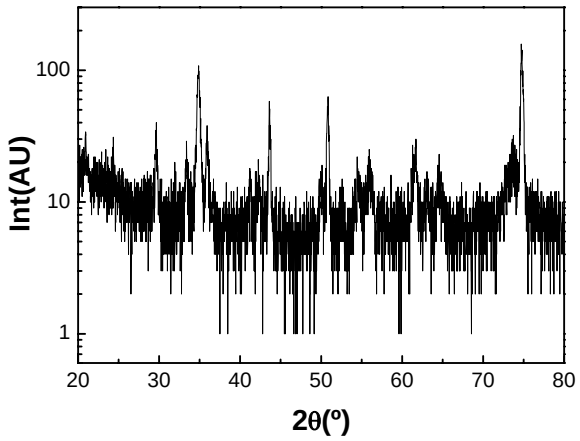

Fig: 6.13: XRD pattern of a sample of CeO_2 grown on YSZ(IBAD)/SS at 1000ºC in static air for 8h, indicates the oxidising of the substrate.

Furthermore the surface has suffered an important degradation as demonstrated by the two optical images shown in fig. 6.14.

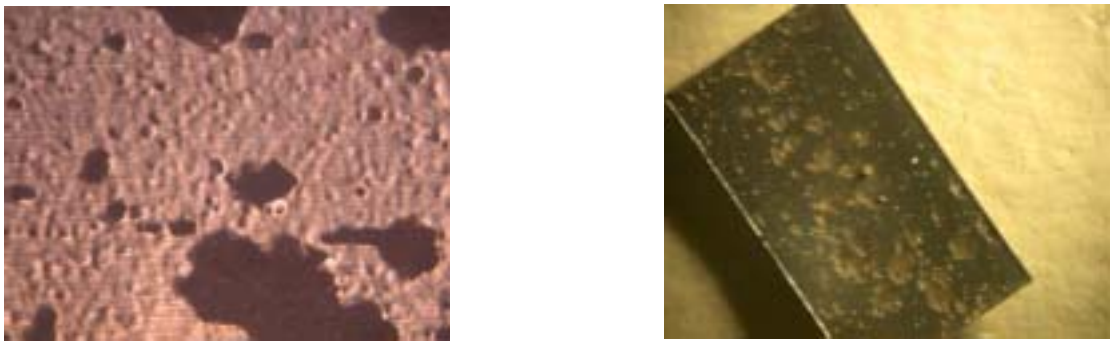

Fig. 6.14: Optical images of the sample synthesised at 1000ºC show how part of YSZ was detached probably during the stainless steel oxidation.

Important detachment of part of the film from the underlying YSZ is visible. We tried to find the tolerance limit of stainless steel to an oxidising atmosphere, decreasing the synthesis temperature. Optical analysis and XRD diffraction on a metal substrate treated for 8h at 900ºC in air have been performed confirming that at this temperature the stainless steel is not altered. We tested then if the decrease in temperature could affect the growth of textured CeO_2. In fig. 6.15(a), a Θ/2Θ pattern of a 25-30 nm ceria film on YSZ(IBAD)/SS substrate is presented.

The presence of only (00L) peaks indicates the absence of secondary phases and a single orientation of the film.

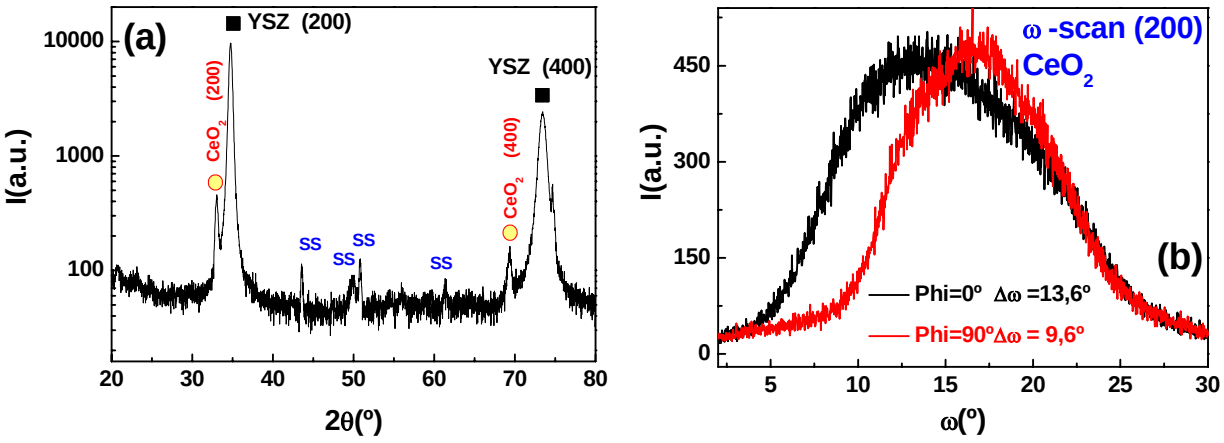

Fig. 6.15(a,b): θ/2θ analysis of CeO_2/YSZ(IBAD)/SS synthesised at 900ºC for 8h in static air. The ceria film presents only the (00l) orientation (a). The rocking curve of the (200) peak of CeO_2 shows an anomalous behaviour. The curve FWHM depends on the ϕ–angle of the sample during the measurement, ϕ=0º and ϕ=90º corresponds to a Δω=9.6º and Δω=13.6º respectively (b).

A careful inspection of the rocking curve of ceria reveals; that the FWHM of the CeO_2 (200) peak depends on the in plane orientation of the sample. The ω-scan of the same sample measured at ϕ=0º and ϕ= 90º gives a difference in FWHM of 4º (fig. 6.15(b)). The ϕ–scan analysis, fig.6.16, presents the same anisotropic behaviour.

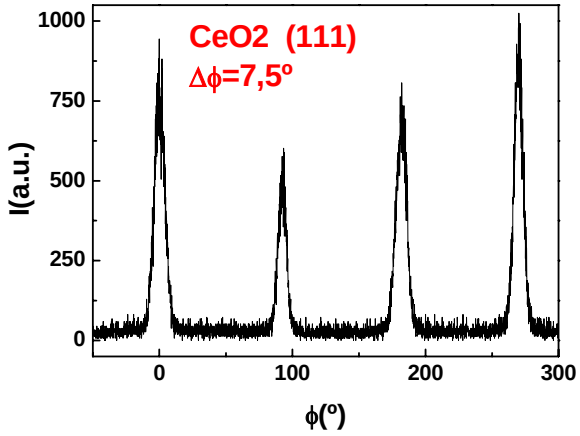

Fig. 6.16: Phi-scan analysis of the (101) CeO_2 orientation presents a mean Δϕ of 7.5º.

In table 6.4 the correspondent values of FWHM for each of the four peaks of the respective ϕ-scan in the (111) reflection for the CeO_2 and for the underlying YSZ are presented.

TABLE 6.4: FWHM values of the Φ-peaks of the (111) YSZ and (111) CeO_2 reflections. These values show that the underlying YSZ template exhibits a pronounced texture anisotropy that is transmitted to the CeO_2 film.

Φ-PEAKS	0º	90º	180º	270º
YSZ(IBAD) (111)	9.1	7.2	9.3	7.6
CeO_2 (111)	8.4	7.1	8.4	6.1

The FWHM for 0º and 180º are greater than the 90º and 270º, ones. SEM analysis of these substrates, fig. 6.17(a), presents linear grain distributions parallel to the re-sputtering Ar+ beam used during the deposition of the YSZ (IBAD).

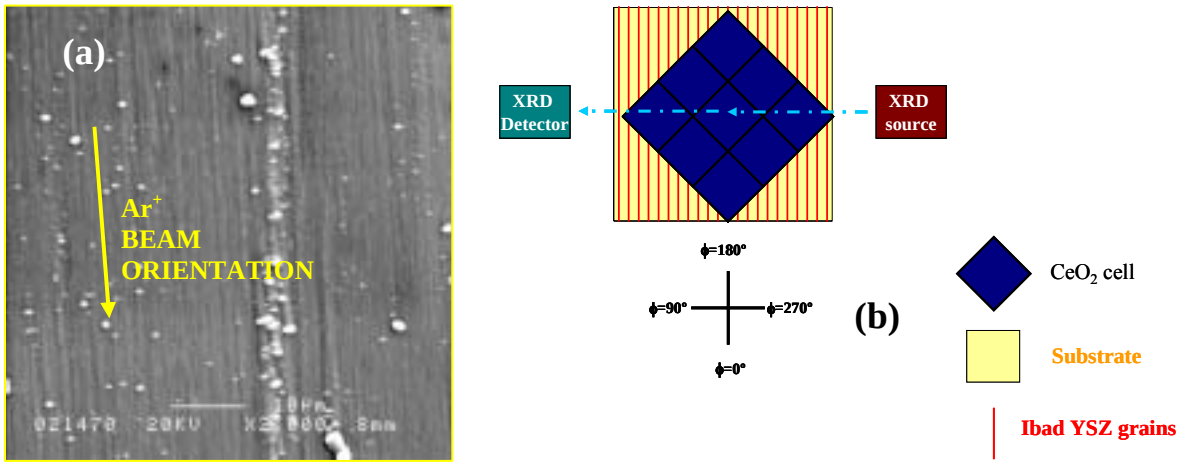

Fig. 6.17(a,b): (a) SEM image of the YSZ(IBAD)/SS substrate. The yellow arrow indicates the orientation of the Ar+ beam. (b) The in plane view shows the substrate orientation with respect to the SEM image and to the sample position during XRD characterization. A correlation between the biaxial texture anisotropy and the Ar+ beam seems to be reasonable.

The coincidence of the higher in plane and out of plane FWHM values with the ion bean orientation during re-sputtering strongly suggests that the IBAD technique could have induced this anisotropy in the YSZ(IBAD)/SS buffer layer.

What is nevertheless important is the mean Δϕ value of this ceria film: 7.5º, which indicates a good in plane texture. Also this time the film texture improves with respect to the underlying substrate, Δϕ(YSZ)=8.3º.

In fig.6.18, an AFM analysis of a 30 nm sample of CeO_2/YSZ(IBAD)/SS after a thermal process of 8h at 900ºC in static air is presented.

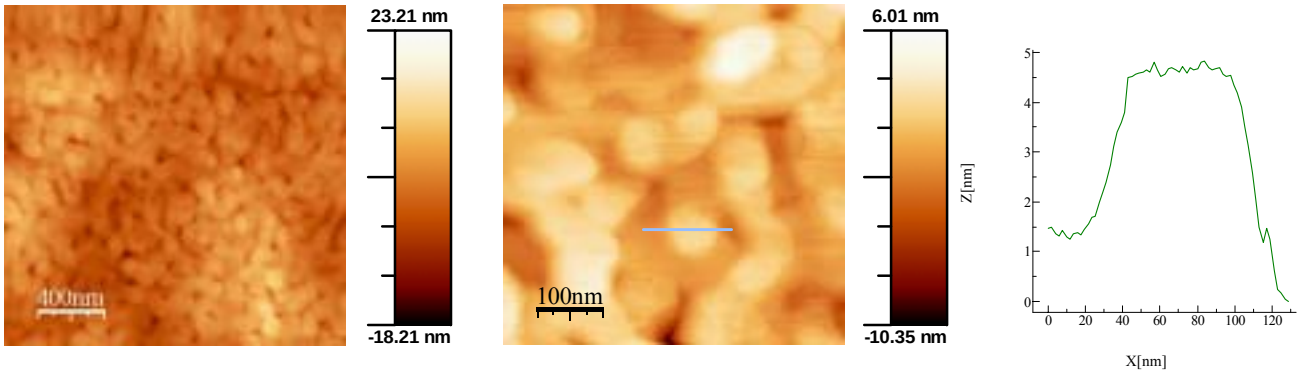

Fig. 6.18: AFM topographical images of the surface of a CeO_2/YSZ(IBAD)/SS sample grown directly in static air at 900ºC for 8h.

The surface morphology is (00L)-terraced. The profile of one of this terrace is similar to the ones found in ceria on YSZ single crystal. It is reasonable to expect that the sample is well textured in its total thickness. Rms values for this sample using different scan areas are presented in fig. 6.19. For the larger scan-area of 20·20 μm, rms is near 11nm. On the other hand, the rms on the terraces is around 0.5 nm.

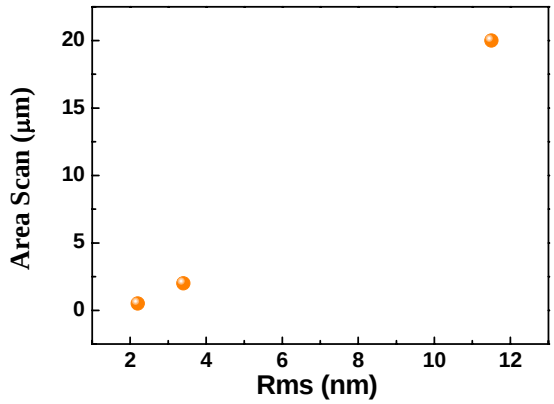

Fig. 6.19: Roughness values of the ceria surface as a function of the area scan size of the AFM instrument.

Locally, the flat surface and a good biaxial texture make this system as one of the more desirable templates for the deposition of the YBCO superconductor film.

6.2.3 GROWTH OF $SrTiO_3/BaZrO_3$ FILMS ON IBAD-DEPOSITED YSZ TEMPLATES ON STAINLESS-STEEL TAPES

The conditions of solution preparation and the thermal treatment of deposited films of STO and BZO are the same as those presented in chapter 5. The in plane texture of these substrates was in the range: $11.5º<\Delta\phi<16º$. A high level of irreproducibility has been observed, especially due to the development of undesired films orientations, in particular for the formation of barium zirconate with (110) orientation. Below we present the best results obtained at present. The synthesis conditions of the buffer layers have been modified only for the process temperatures: for BZO, 800ºC and for STO 850º C seem to give the best results, see table 6.5.

TABLE 6.5: Optimised synthesis condition for the BZO and STO buffer layers on YSZ(IBAD)/SS.

BUFFER LAYERS	SOLUTION CONCENTRATION	THERMAL PROCESS	SYNTHESIS TEMPERATURE	OVEN ATMOSPHERE
$BaZrO_3$	0.3M	60ºC/h-250ºC dwell 30min 200ºC/h-Tmax	800ºC	Ar/H_2
$SrTiO_3$	0.25M	60ºC/h-250ºC dwell 30min 200ºC/h-Tmax	850ºC	Ar/H_2

The θ/2θ pattern of a sample of BZO on YSZ(IBAD)/SS, fig. 6.20, shows only the (00L) orientation. In the inset the omega-scan peak reveals an out of plane texture with $\Delta\omega=10º$. This wide value is correlate to the underlying YSZ film ($\Delta\omega=9º$).

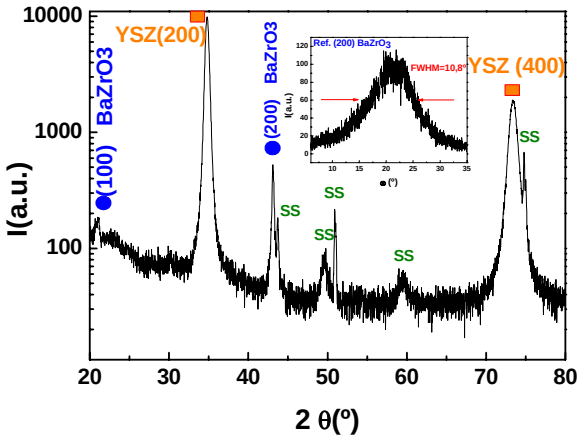

Fig. 6.20: θ/2θ spectrum of a BZO/YSZ(IBAD)/SS template synthesised at the optimised conditions.

The (101)-BZO pole figure for the BZO/YSZ(IBAD)/SS structure confirms that the in plane [100] BZO and [110] YSZ directions are at 45º from each other, indicating a cube on cubeorientation, (fig. 6.21).

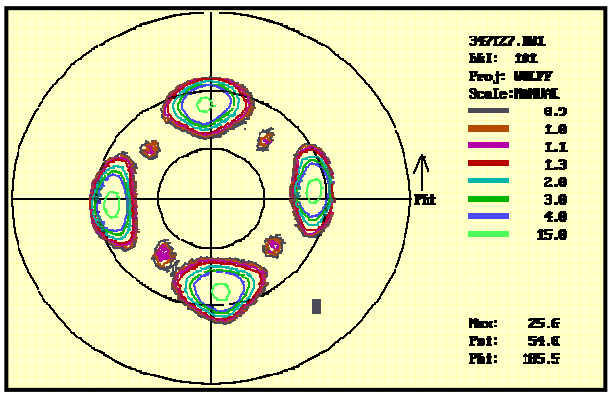

Fig. 6.21: (101)-$BaZrO_3$ pole figure for the BZO/YSZ/SS structure. Eight peaks are visible due to the high off-plane misorientation of the YSZ(Δω=9º).Their relative positions at 45º reveals a cube on cube epitaxial relationship.

The ϕ-scan of the (101) reflection of BZO in fig.6.22 presents also eight peaks; four correspond to (101)-BZO and four to (111)-YSZ.. The angular shift between both sets of peaks is 45º, confirming the cube on cube epitaxial relationship between BZO and YSZ. The FWHM of the BZO is Δϕ=12,6º compared to the Δϕ=10,6º of the YSZ(IBAD)/SS.

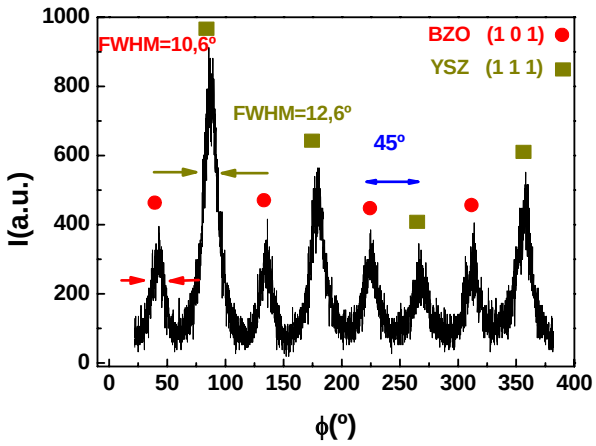

Fig. 6.22: (101) ϕ-scan of the BZO Δϕ=12,6º compared to the Δϕ=10.6º of the YSZ peaks.

On these substrates buffered with (00L) oriented BZO, a film of STO (25-30 nm) has been deposited at 850ºC for 4h in Ar/H_2. Fig. 6.23 shows the θ/2θ of our best sample. Also STO has grown with only the (00L) orientations.

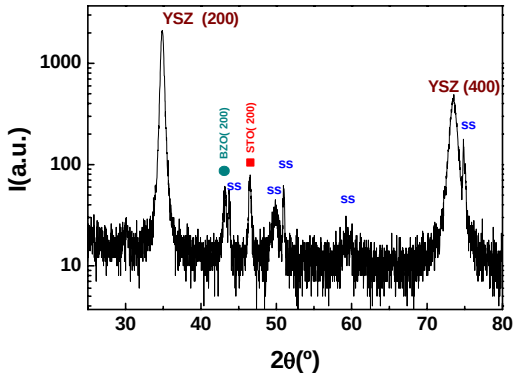

Fig. 6.23: XRD pattern of the double buffer STO/BZO/YSZ(IBAD)/SS grown at optimum conditions.

Fig. 6.24 (a,b) are respectively the out of plane measurements of the (200) peak of BZO (black), STO (red) YSZ in the inset , and the in-plane measurements of the upper film of STO.

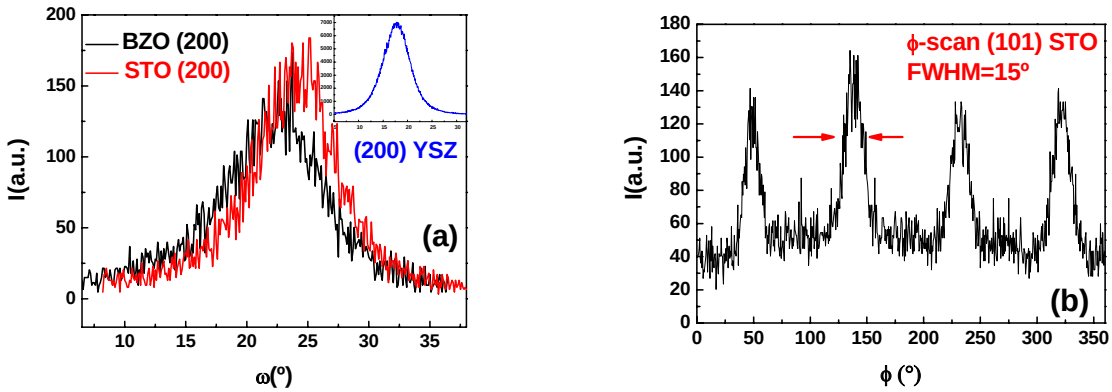

Fig. 6.24(a,b): (a) Rocking curve analysis of the (200) reflections of YSZ, BZO and STO. (b) Phi-scan analysis of the top buffer, STO, Δϕ=15º.

The four peaks of STO in comparison with the corresponding (101)-BZO ϕ-scan indicate a cube-on-cube epitaxial relationship as shown in fig. 6.25.

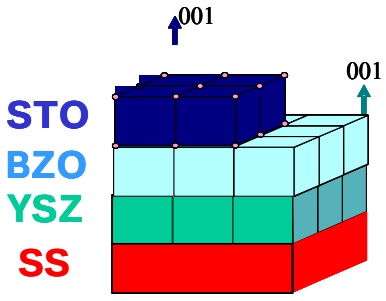

Fig. 6.25: Architecture of the STO/BZO/YSZ(IBAD)/SS template.

By these analyses any important change in the biaxial texture of the two buffer layers respect to the underlying YSZ is detected fig. 6.26(a).

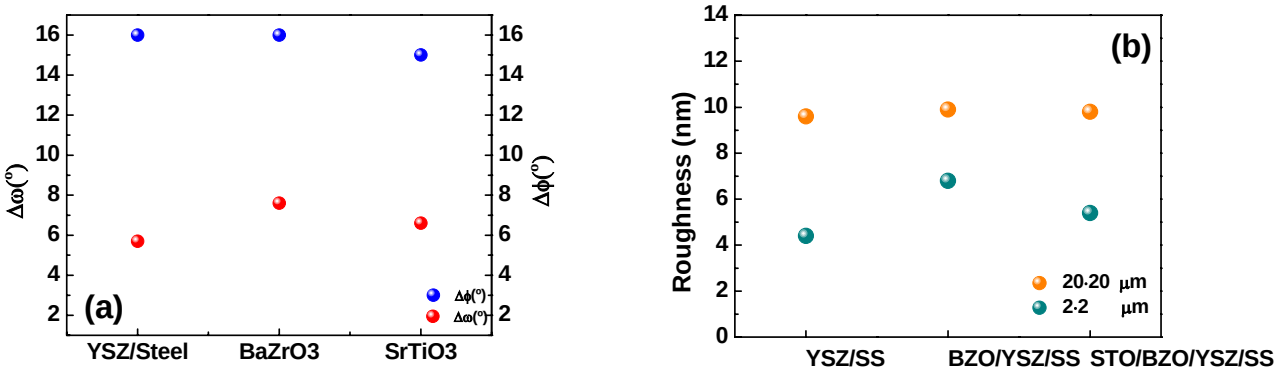

Fig. 6.26(a,b): (a) FWHM of ω and ϕ-scan of STO/BZO/YSZ(IBAD)/SS. The measurements have been done first on the YSZ/SS substrate, and then after each MOD buffers deposition. The similarity between the misorientation spread of the BZO and STO layers and the YSZ one, strongly suggest that the texture quality of the MOD deposited buffers is limited by that corresponding to the underlying YSZ template. (b) Typical roughness values of the YSZ, BZO and STO layers of a single STO/BZO/YSZ(IBAD)/SS structure. Black points represent the 20·20 μm scan area and the red ones the 2·2 μm area.

Also the roughness of the sample does not change as shown in fig. 6.26(b); the measures have been obtained just before deposition for YSZ surface, and after each of the two film synthesis. Fig. 6.27(a,b,c) are respectively the YSZ, BZO, and STO surfaces measured in 2·2 μm scans. No porosity is visible.

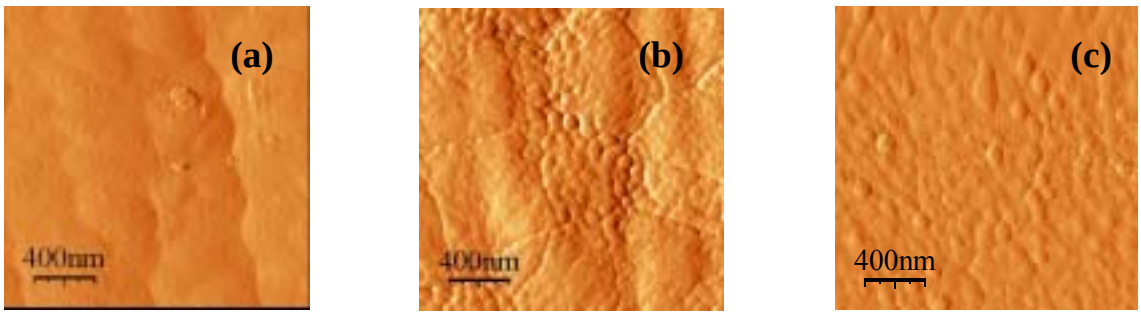

Fig. 6.27(a,b,c): AFM images of the three surfaces of a STO/BZO/YSZ(IBAD)/SS sample: (a) YSZ, (b) BZO and (c) the STO.

We have succeeded in growing BZO and STO/BZO layers having the unique (00l) orientation on YSZ(IBAD)/SS by the CSD technique. As an important result, neither the texture spread nor the surface roughness of the MOD deposited layers are worst than those corresponding to the underlying YSZ template. Further experiments using best textured YSZ(IBAD)/SS will be necessary to understand if the STO/BZO/YSZ(IBAD)/SS template could be a real candidate to the final superconductor cable.

REFERENCES

[1] A.Kursumovic,R.Hühne, R.Tomov, B.Holzapfel, B.A.Glowacki, J.E.Evetts. *Physica C,* ***405,*** *219-226, (2004).*

[2] M.Kai, T.Izumi, K.Hasegawa, Y.Tokunaga, S.Asada, Y.Nakamura, T.Watanabe, Y.Shiohara, *Physica C,* ***378-381****, 998-1002, (2002).*

[3] J.Dzick, J.Hoffmann, S.Seviers, L.O.Kautschor, H.C. Freyhardt. *Physica C,* ***372-376,*** *723-728, (2002).*

[4] T.Muroga et al., *Superconductiovity Conference in Huston, August 4, 2002, Program No. 4MH01 preprint.*

[5] T.Muroga, H.Iwai, T.Niwa, T.Araki, Y.Yamada, T.Izumi, Y.Shiohara, Y.Iijima, T.Saito, T.Kato, Y.Hirayama, *Physisca C(2003) Proceedings.*

Chapter 7

SYNTHESIS AND GROWTH OF MOD-TFA YBCO

7.1 INTRODUCTION

P.Barboux et al.[1]using a Sol-Gel method realised for the first time a YBCO film with a controlled precipitation of the inorganic salts of Yttrium, Barium and Copper.

This method resulted to be slow and yielded inhomogeneous samples. In 1989 G. Moore et al. [2] produced YBCO films using an alkoxides Sol-Gel route. Barium and Yttrium salts with Copper ethoxide were dissolved in methanol and after a hydrolysis, a gel was produced. However the use of alkoxide precursors has several problems: alkoxides can react in contact with the air humidity and they have a high cost. Kumagai et al. [3,4] were the first using Metal Organic Decomposition (MOD) [5] to obtain a YBCO film, thus simplifying the experimental process avoiding the necessity of using an inert atmosphere. In spite of that, a not easy problem appeared: the barium cation reacts during the thermal treatment preferably with the organic compound forming $BaCO_3$. $BaCO_3$ is undesirable because it may deteriorate the superconducting YBCO properties [6]. Once it is formed the only way to eliminate $BaCO_3$ is to treat the film at 1000°C, but at these elevated temperatures metal substrates may become unstable and interdiffusion effects are enhanced.

The solution to this problem was found by A.Gupta et al. [7], who used a MOD-TFA process, similar to that used by P.M. Mankiewich et al. [8] in their thermal co-evaporation. In this process the Ba-precursor is BaF_2, more favourable than the $BaCO_3$ one. BaF_2 decomposes at high temperature, when there is no more risk of $BaCO_3$ formation. This decomposition can be controlled by adjusting the water partial pressure.

In this chapter we make use of the TFA process to grow YBCO on the different buffer layers described in the preceding chapters.

Following A.Gupta et al., we use a precursor film with metal trifluoracetates, (MOD-TFA), $Ba(CF_3COO)_2$ $Cu(CF_3COO)_2$ $Y(CF_3COO)_3$, which transform to BaF_2, CuO and Y_2O_3 by a pyrolysis process.

7.2 STATE OF THE ART

The TFA-MOD solution precursors are Yttrium, Barium and Copper triacetates, which are dissolved in trifluoracetic acid (TFA) and water [9]. To obtain an homogeneous solution, it is useful to submit the solution to reflux at 75ºC for four hours to transform the triacetate in trifluoracetate, as shown in the following reaction :

$$M^{(z+)}(\text{-OOC-CH}_3)_z + z\cdot CF_3COOH \xrightarrow[4h]{75^oC} M^{(z+)}(\text{-OOC-CF}_3)_z + z\cdot CH_3COOH$$

where $M^{(z+)}$ corresponds to Y^{3+}, Ba^{2+} or Cu^{2+}.

The solution is dried into a blue gel by a slow solvent evaporation at 110ºC; the blue colour is derived from the Cu^{2+}ion. The gel is then dissolved in methanol obtaining a blue solution that is ready to be deposited. The metal concentration of the coating solution is below 3.0 mol/l because of the limited solubility of trifluoracetates. In TFA-MOD, impurities as water and acetic acid in the coating solution may degrade the J_c of the resulting film. Araki et al. developed the so called SIG (solvent-into-gel) method [10], in which a highly purified coating solution is used to obtain high J_c films. Many deposition processes exist, but the most widely used at the laboratory level is the spin coating, due to its "easy" technology. In fig.7.1 it is schematically described how the gel polymerises during the spin coating process [11].

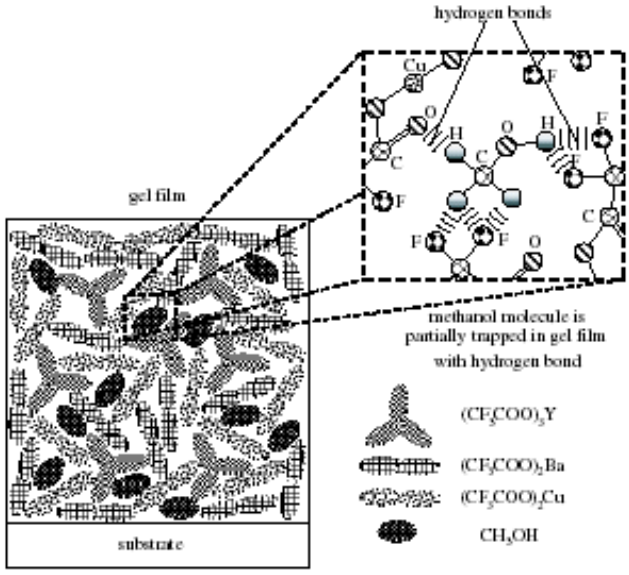

Fig. 7.1: Gel structure after deposition of the TFA- MOD YBCO film.

In this technique, for a given concentration and viscosity the film thickness is controlled by the spinning rate as shown in fig. 7.2 [12]. It decreases with spinning rate but it has a lower limit.

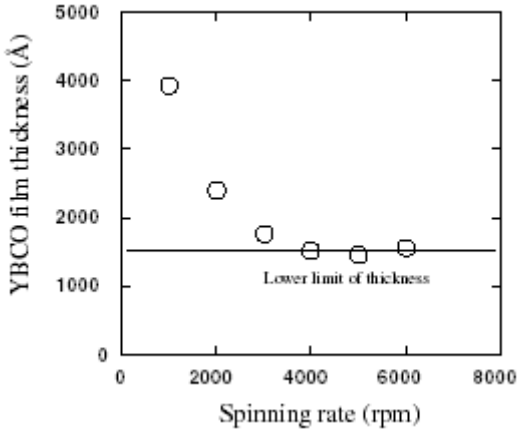

Fig. 7.2: Dependence of YBCO film thickness on the spinning rate. Reducing the spinning rate the thickness increases.

In any case, , to avoid homogeneity problems associated to slow spinning rates, the best way to increase the YBCO film thickness is raising directly the TFA-solution concentration, (see chapter 3). However cracks are generated in a thick film because of the drying stress that is inherent to the material [13]. Each material has a critical gel film thickness, that for YBCO films on (001) LAO single crystal substrates it is about 350-450 nm.

After deposition, the first thermal treatment is the calcination process, well known as pyrolisis process. The organic part of the film is burned out in a controlled atmosphere until an amorphous matrix of Y-Ba-O-F and nanocrystals of CuO [12] is obtained.

The gas flow through the oven is humidified during the pyrolisis to suppress the sublimation of copper trifluoracetate [14] through the formation of the copper hidroxytrifluoracetate, which decomposes before sublimating. Metal trifluoracetates decompose at 200-250ºC within about 10h during the pyrolysis. If the time is shorter, the salts are burned out to become a black oxide powder. The long chemical reaction required for decomposition is typical of organo-chemical reactions involving the break out of a covalent bond. After pyrolisis, the precursor film is composed by Y-Ba-O-F and nano-crystalline CuO [15].

During the firing process the film reacts to form tetragonal YBCO according to the simplified reaction:

$$2\ BaF_2 + 2\ CuO + 1/2\ Y_2Cu_2O_5 + 2\ H_2O \longrightarrow YBa_2Cu_3O_{6.5} + 4\ HF$$

The maximum firing temperature is in the range of 725ºC-850ºC, the controlled gas flux in the oven is humidified at 0.1-30%, the gas is inert and can be Argon or Nitrogen mixed with 50-4000 ppm oxygen gas [10,16,17]. The humidified gas is used to decompose the BaF_2 according to:

$$BaF_2 + H_2O \longrightarrow 2\ HF + BaO$$

The fluoride decomposition takes place at about 650ºC [18]. At this temperature the $BaCO_3$ formation is not favoured. Above 725ºC, a c-axis-oriented YBCO structure is obtained, while at lower temperatures, a-axis is preferred. That is why it is used a fast ramp to reach the maximum firing temperature, of about 25ºC/min .The reaction is controlled to a high extent by the BaF_2 decomposition and F^- elimination. The process can be in situ monitored using a F^-detector [19] in the gas exhaust line. When no more fluoride anions are detected the reaction is completed and the humidified gas flux is substituted by a dry one of the same inert gas. The final treatment is an annealing in an oxygen flux, below 525ºC, for about one hour, to transform the tetragonal YBCO structure to the superconducting orthorhombic one [9,19].

7.3 EXPERIMENTAL

7.3.1 SOLUTION PREPARATION AND DEPOSITION

In the present study we follow a procedure for the TFA deposition of YBCO developed in our laboratories by Castanyo et al [20].

The solution can be prepared in a non classical way by dissolving a weighted amount of YBCO commercial powder supplied by Praxair. This powder is dissolved in

TFA acid [21]. The blue solution is gellified by a thermal treatment at 110ºC. The gel is then dissolved in methanol as usual, forming the blue solution. In this way, the problem of controlling the solution stoichiometry as well as the presence of water are crossed, which improves the reproducibility of the growth process. The deposition system is the spin coater described in chapter 3 pag.58, using the conditions listed in Table 7.1.

TABLE 7.1 : Optimised parameters for the deposition of YBCO precursor.

Parameters	Optimum value
Metals concentration	1.45 mol·dm^{-3}
Precursor solution viscosity	0.0012 Pa·s
Spinning acceleration	2500 rpm/s
Spinning deposition rate	5000 rpm

7.3.2 PYROLYSIS

During the pyrolysis, as said before, we control the Cu volatility by adding a certain quantity of water which transforms $Cu(CF_3COO)_2$ to $Cu(OH)(CF_3COO)$, which is not volatile. The water partial pressure is regulated by bubbling the vector gas in water at a controlled temperature. Depending on the water bath temperature, the gas will contain a different amount of water (fig. 7.3).

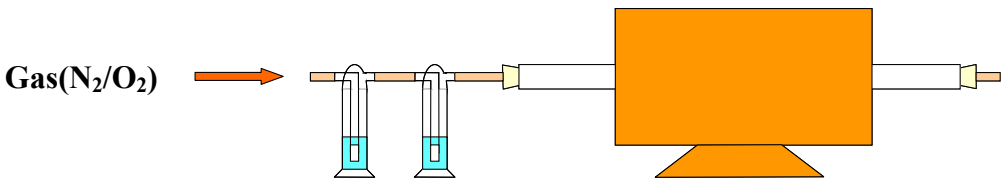

Fig. 7.3: Experimental system to control the water partial pressure in the gas.

The oxygen pressure, instead, is controlled by two mass flows, one for nitrogen allowing a 0.6 l/min maximum flux, and one for oxygen with a maximum flux of

0.003 l/min. Mixing the two gasses it is possible to work in a range of oxygen partial pressures of 0.2 mbar-1bar. Fig. 7.4 shows a schematic diagram of the thermal treatment.

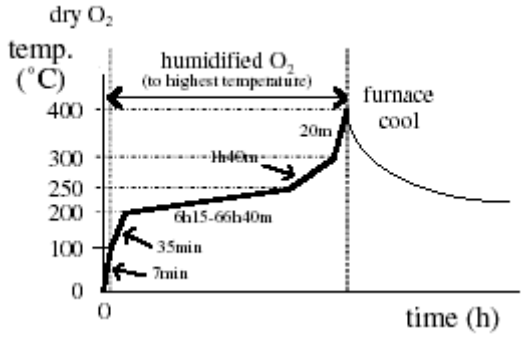

Fig. 7.4: Slow pyrolysis thermal treatment.

The vector gas is bubbled in the water starting from 110ºC to avoid its condensation on the pyrolized YBCO film. In Table 7.2 are summarized the optimised parameters for the pyrolysis.

TABLE 7.2 : Optimised values for the YBCO pyrolysis

Parameters	**Optimum value**
Duration	12 h
$P(O_2)$	1000 mbar
$P(H_2O)$	73 mbar
Flux	0.1 l/min

One effective way to control the film quality after the pyrolysis is by inspection of the film surface in an optical microscope. When the organic decomposition has been well controlled, the sample looks like very homogeneous, almost featureless, as shown in fig. 7.5(a), otherwise the film exhibits important heterogeneities as may be seen in fig. 7.5(b).

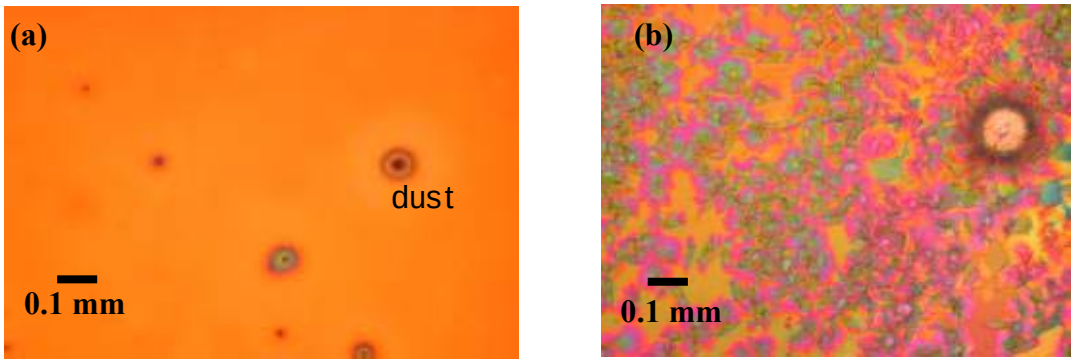

Fig. 7.5 (a,b): Optical microscope images: (a) homogeneous pyrolized film, (b) defective pyrolysis film presenting heterogeneities.

A homogeneous colour also means that the film thickness is the same throughout. The geometric figures which can appear in the microscope pictures fig. 7.5(b) may be related to local very exothermic reactions. Even if the thermal treatment during pyrolisis does not exceed 400ºC, it is possible that local undesirable exothermic reactions suddenly rise the temperature above 400ºC inducing cation segregations into exotic shapes as those shown in fig. 7.5(b).

7.3.3 FIRING PROCESS

In this step of the TFA process, it is very important to control all the synthesis parameters: the water partial pressure, the oxygen pressure, the vector gas rate, the fast thermal ramp, the synthesis temperature and the dwell time at T_{max}. Only a proper combination of all these parameters allows growing YBCO with good superconducting properties.

The thermal ramp, for example, can influence the texture and growth orientations of the YBCO film. If the T_{max} of the synthesis is reached rapidly, the c-axis YBCO growth is favoured, otherwise with a slow ramp a,b-planes will be present. The YBCO c-growth is also connected with the oxygen partial pressure of the process, as illustrated in fig. 7.6, where the YBCO orientation phase diagram is presented. At 800ºC, it is better to use a low oxygen partial pressure (0.02%) in order to be in the zone where the c-growth is favoured.

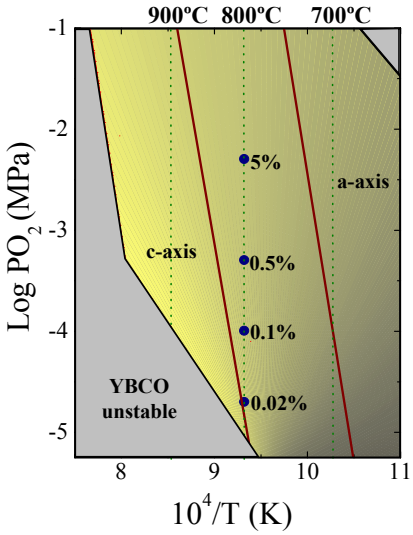

Fig. 7.6 : Phase diagram of YBCO orientation depending in temperature and oxygen partial pressure.

The typical firing treatment is represented in fig. 7.7.

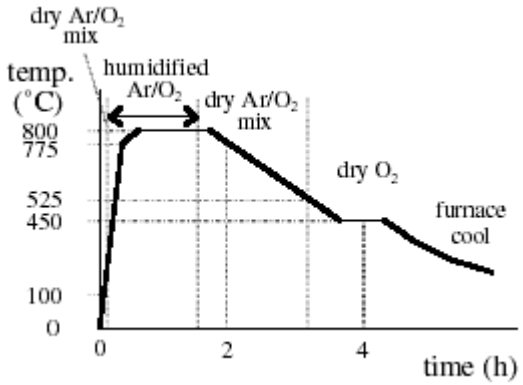

Fig. 7.7: YBCO typical firing process.

The TFA YBCO reaction is controlled by eight different steps as sown in fig.7.8:

- The water gas diffusion in the precursor film towards the reaction front, run by the vector gas flow.
- The water absorption in the reaction front.
- The chemical reaction between water and BaF2.
- The release of HF at the reaction front.
- Diffusion of HF out of the film.
- Stagnant layer formation.

- Diffusion of HF thought the stagnant layer towards the vector gas.
- Release of HF from the stagnant layer in to the vector gas.

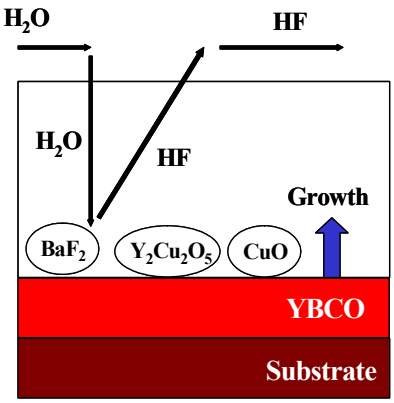

Fig. 7.8 : The reaction parameters can be summarised in eight different steps.

The discussion about whether the YBCO formation is limited by gas diffusion, or by the chemical reaction (see reactions in pag.151), or by a mixed mechanism, is still open.

If the reaction is under a diffusive regime, an increase of the vector gas rate, will increase the exchange between the water containing gas and the HF, thus increasing the YBCO growth rate. In the case of a chemical regime, if the limiting factor is the reaction between BF_2 and H_2O, working at higher water partial pressures will increase the YBCO growth rate.

In order to track the YBCO reaction, we have used a F^-detector [22]. When the F^- concentration does not increase any more, all the BaF_2 has decomposed, (see fig.7.9 (a)) [23], the reaction is completed and we stop bubbling the vector gas in the water bath and the film is dried for half an hour at T_{max}.

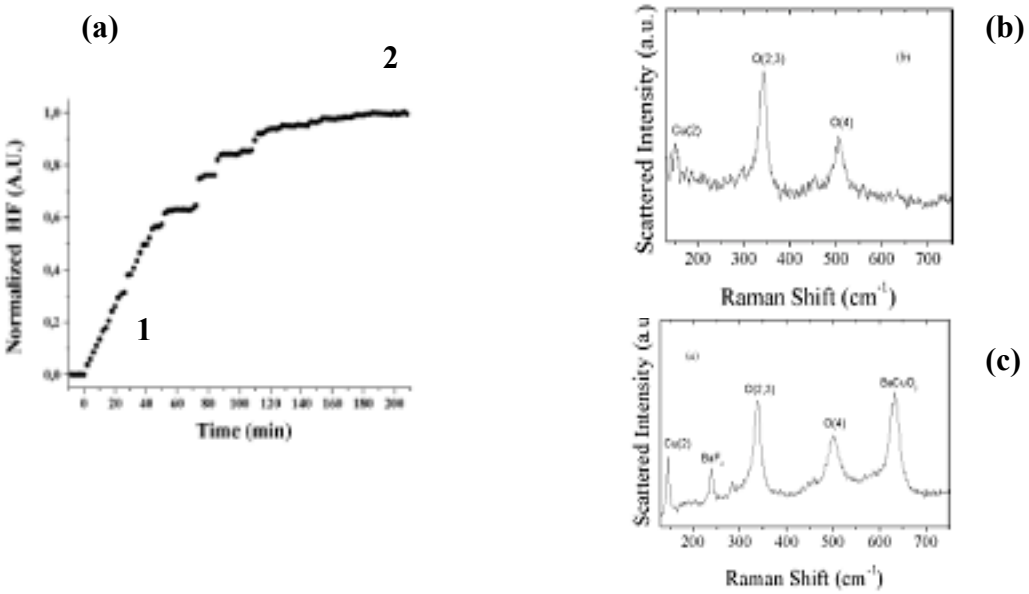

Fig. 7.9 (a,b,c) : (a) **[**F^-] measurement to control the kinetic, of the YBCO growth reaction. In zone 1 the reaction has not already finished, as confirmed by μ-Raman analysis (c). In zone 2, when the F^- signal does not increase any more , the reaction is finished. (b) Ex-situ μ-Raman confirms the absence of non-reacted BaF_2 or $BaCuO_2$. (b) and (c) are the results of different samples, one taken out the oven once in zone 1 and the second that had finished its reaction process.

A complementary way to control the end of the YBCO synthesis, is by micro-Raman spectroscopy analysis. This method, developed by JC Gonzalez et al. [23] in our laboratory, is used to quantify the presence of non-reacted BaF_2 and other intermediate phases, with a sensitivity of 1% (fig. 7.9(b,c)) [23]. Another advantage of this technique is that it allows a local analysis using a light spot size between 1 and 10 μm.

The optimised parameters for the growth of YBCO on LAO single crystal are listed in Table 7.3.

TABLE 7.3 : Firing process parameters optimised for the YBCO synthesis on LAO single crystal.

Parameters	**Optimum value**
Maximum Temperature	795ºC
P(O_2)	0.2 mbar
P(H_2O)	6 bar
Flux	0.6 l/min

7.4 RESULTS ON THE OPTIMISED BUFFER LAYERS

We deposited PLD-YBCO on one buffer of CeO_2/YSZ^{SC} and one of $STO/BZO/MgO^{SC}$. These experiments were carried out in the Department of Optic of the University of Barcelona, (U.B.).These tests have been important to evaluate the real quality of CSD templates, because the PLD technique permits to obtain high quality YBCO film with a high reproducibility. The current densities of these two samples could indicate with a good approximation the upper quality limit achievable by the more complicate TFA-deposition method. In laser ablation, high-power laser pulses are used to evaporate matter from a target surface such that the stoichiometry of the material is preserved in the interaction. As a result, a supersonic jet of particles (plume) is ejected normal to the target surface. The ablated species condense on the substrate placed opposite to the target. The ablation process takes place in a vacuum chamber - either in vacuum or in the presence of some background gas. In the case of oxide films, oxygen is the most common background gas. YBCO layers were prepared using a KrF excimer laser that operates in the ultraviolet spectral region at a wavelength of λ= 248 nm. The maximum pulse energy of this laser is 1.3 J, which corresponds to a mean power per pulse of approximately 30 MW. The maximum repetition frequency is 50 Hz and the pulse duration is approximately 50 ns. For the growth of YBCO the energy density was set to 2.4 J/cm^2 with a pulse frequency of 10 Hz, while the substrate temperature was held at 775ºC. The YBCO film was grown in an oxygen atmosphere of 0.25 mbar O_2 at a deposition rate of 0.07 nm/pulse. After the deposition, the sample was cooled down to room temperature in an oxygen partial pressure of 1 atm.

7.4.1 TFA-DEPOSITION OF YBCO ON CeO_2/YSZ^{SC}

Fig.7.10 shows a typical XRD pattern of a YBCO TFA film, grown at 795ºC, $P(H_2O)$=6 mbar, $P(O_2)$=0.2 mbar, deposited on a CeO_2 buffer layer synthesised at 750º (in Ar/H_2 5% atmosphere). It can be clearly observed that a large quantity of cerium

oxide has reacted with YBCO forming $BaCeO_3$, while the non-reacted part of the film is not visible in the XRD pattern.

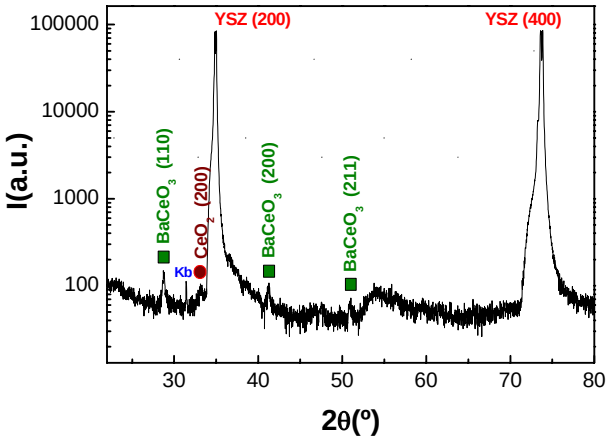

Fig. 7.10: XRD pattern of a YBCO film grown at 795ºC on CeO_2/YSZ^{SC}. No YBCO reflections are observed.

The SEM image of this sample is presented in fig.7.11; the high temperature and the premature reaction with the underlying ceria could have caused the high porosity observed in the film.

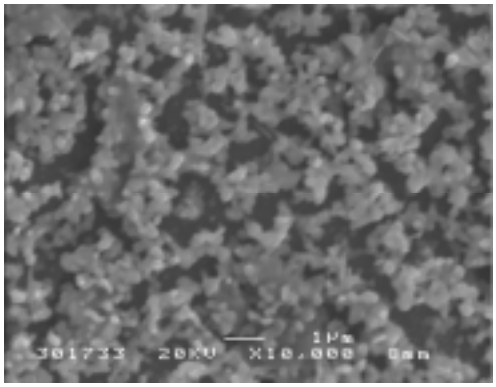

Fig. 7.11: SEM image of the YBCO film grown at 795ºC on a ceria template. High porosity is visible.

In order to minimize the reactivity between CeO_2 and YBCO, we lowered the synthesis temperature to 750ºC. Even in this case, no real improvement of the YBCO texture has been obtained. Since the problem had to be on the surface of the cerium oxide grown in Ar/H_2, in a recent step we tested one buffer layer treated at 1300ºC in static air (see chapter 4). Such buffers have a better crystallinity, a well textured surface, and a well connected surface grain morphology, in contrast to CeO_2 buffer layers

processed in Ar/H_2. On these substrates the YBCO developed good in-plane and out plane texture as represented in fig.7.12 (a,b).

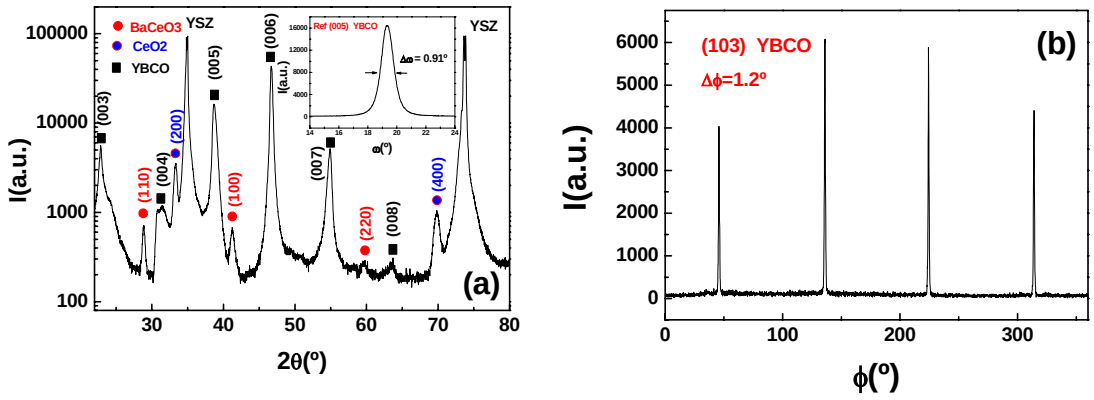

Fig. 7.12 (a,b) (a) θ/2θ scans show only (00l) orientations; the inset shows a rocking curve of the YBCO (005) reflection , Δω=0.91º. (b) Phi-scan , Δϕ=1.2[a]

In the XRD pattern tiny amount of $BaCeO_3$ peaks are still present but the reaction has not altered the formation and the texture of the YBCO film. This observation strongly suggests that the $BaCeO_3$ forms once the YBCO film has already crystallized.

It should be difficult that the YBCO could nucleate and growth epitaxially on the $BaCeO_3$ if it is randomly oriented as shown by the XRD spectra. Fig.7.13 shows the $BaCeO_3$ film at the interface between CeO_2 and YBCO.

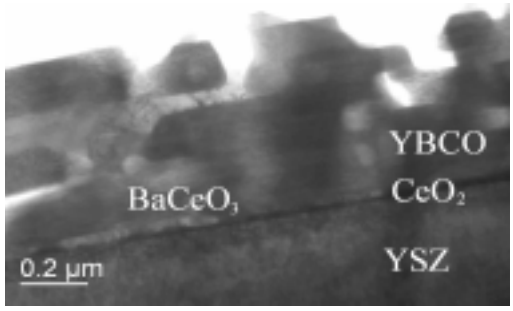

Fig. 7.13: TEM image showing a YBCO film grown on CeO_2/YSZ^{SC}. In some zone of the interface, the presence of $BaCeO_3$ formed from the reaction CeO_2-YBCO has been also detected [15].

It is important not to forget which is our main aim, i.e. to grow a YBCO film on a CeO_2(MOD)/YSZ(IBAD)/SS. Unfortunately the thermal treatment of the CeO_2 at 1300ºC in static air could induce the oxidation and destabilization of the stainless steel

tape as discussed in pag.138. Therefore, we tested the TFA-YBCO deposition on samples of CeO_2 grown in Ar/H_2 but post annealed at a lower T_{max} (1000ºC and 900ºC), at which the static air treatment was still effective. The texture, roughness and the respective critical current density values of the YBCO film on these CeO_2 samples treated in static air are summarised in Table 7.4. The YBCO has been synthesised with the following conditions: Tsyn.=750ºC , $P(H_2O)$= 6mbar,$P(O_2)$= 0.2 mbar and a total flux of 0.6 l/min.

TABLE 7.4: Texture, roughness and transport J_c results of YBCO films grown at the same conditions on CeO_2 buffer layers treated in static air but at different temperatures : 1300ºC, 1000ºC and 900ºC.

Static air Annealing T(ºC)	YBCO Δω	YBCO Δϕ	Rms (nm) 20*20μm area CeO_2	J_C (77 K)
1300	0.91º	1.2º	2.5	0.26 MA/cm^2
1000	0.84º	1.33º	3.2	1.6 MA/cm^2
900	0.74	-	1.7	0.16 MA/cm^2

Best results were obtained on the CeO_2 treated at 1000ºC in static air. The YBCO texture is excellent, as demonstrated by the off-plane and in-plane misorientations spread values: Δω=1.33º and Δϕ=0.84º. In the XRD spectra there are no traces of other crystalline phase except for $BaCeO_3$ and no different YBCO orientations have been detected fig.7.14 (a,b).

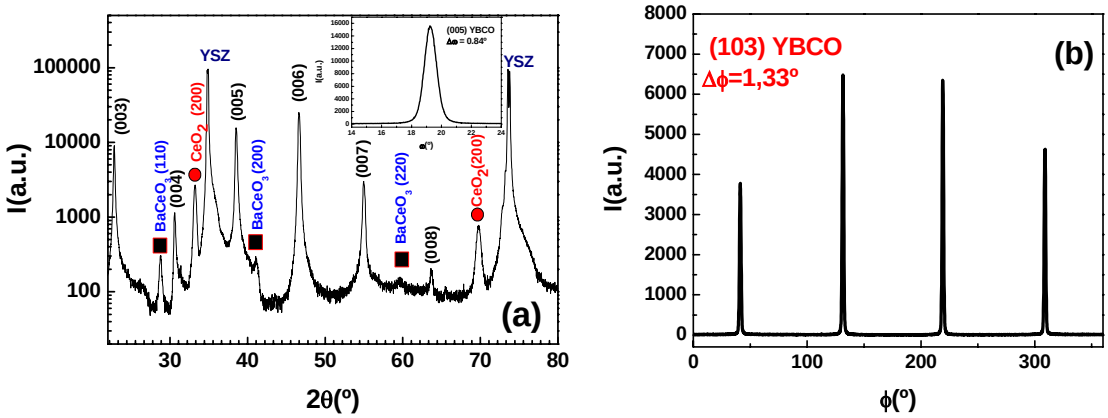

Fig. 7.14(a,b): (a) θ/2θ pattern of a YBCO sample grown at 750ºC on a CeO_2/YSZ^{SC} template post annealed in air. In the inset, the rocking curve of the (005) reflection of YBCO is shown, Δω=0.84º. (b) ϕ-scan of a YBCO film grown on a CeO_2 buffer layer, Δϕ= 1.33º.

In fig.7.15, a superposition of the ϕ–scans of the reflections (111) of CeO_2, (111) YSZ single crystal, and the (102) of the YBCO are presented. Since the four peaks of each single ϕ–scan, lie in the same ϕ angle it is obvious that the YBCO has grown along the diagonal of the cerium oxide unit cell, as expected taking into account the relations of unit cell parameters $\mathbf{a_{YBCO} \sim a_{CeO2} \cdot \sqrt{2}/2}$ **(ε=0.72%).**

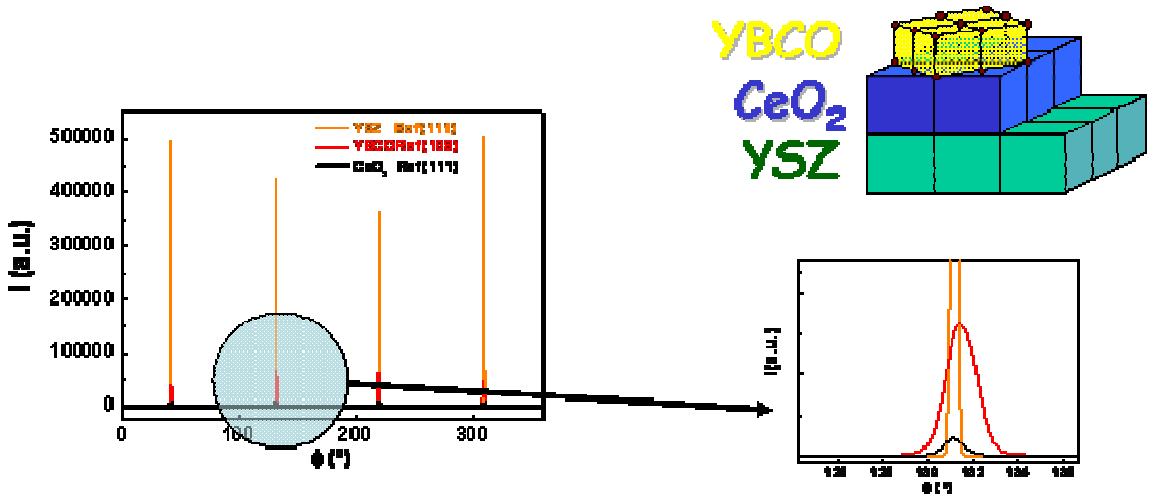

Fig. 7.15 : YBCO coated architecture. The ϕ–scan of the (111) YSZ, (102) YBCO and (111) CeO_2 reflections, indicate a growth geometry as depicted in the schematic.

μ-Raman analysis confirms the absence of impurities, as shown in fig.7.16. In addition, μ-Raman was used to check the occurrence of a-axis grains. The obtained value of δ=0.9 indicates that 90% of the film volume exhibits the desired c-axis orientation.

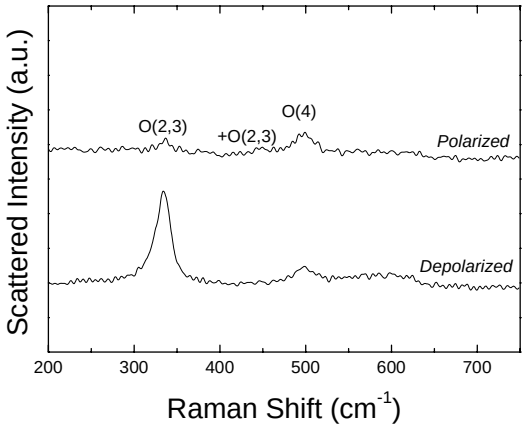

Fig.7.16: μ-Raman analysis of the YBCO film. No traces of impurities are detected [23].

The SEM images, fig.7.17, indicate that the YBCO film is quite dense with a low porosity and no a/b planes or growth disorder.

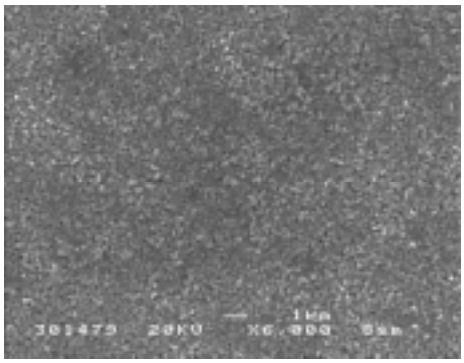

Fig. 7.17: Secondary electrons image of the YBCO thin film grown on CeO_2/YSZ single crystal. No a/b planes are present.

SQUID measurements confirm the high quality of the YBCO superconductor film. The critical current density, J_c, has a value of 17 MA/cm^2 at 5K , and 2.3 MA/cm^2 at 77K, (fig.7.18). The resistivity curve shows a critical temperature of 90K and no residual resistivity, that is what we expect for a single phase YBCO film (fig.7.19).

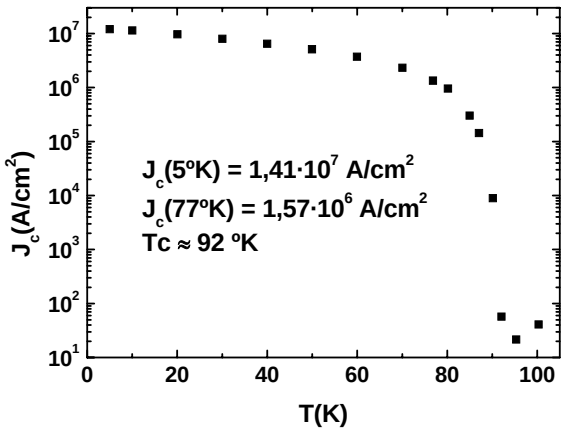

Fig. 7.18: Inductive measurement of the critical current density.

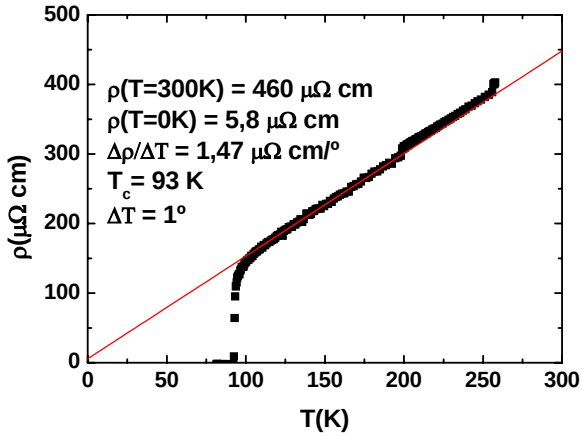

Fig.7.19: Resistivity measurements 0T for a YBCO thin film grown on CeO_2 buffer layer.

The curve in fig.7.19, shows ρ(T=0K)~0 μΩcm, reflecting a good connectivity of the film, which can be associated with strongly coupled grain boundaries and the absence of impurity phases, in agreement with XRD, μ-Raman and SEM characterisations.

On the other hand, the room temperature value, ρ(T=300K)=460 μΩcm, is consistent with a low porosity, (as a reference, a typical value for single crystals is ρ~200 μΩcm).

The reason why only the cerium oxide samples treated in static air are an useful buffer layer to grow up a well textured YBCO thin film, is associated with two possible causes. The first is that the standard CeO_2 samples (grown at 750ºC in Ar/H_2), unlike the ones treated in static air , have non textured surfaces, (see chapter 3 pag.71). The surface is fundamental to transfer the texture to the YBCO film. The second reason as seen by the AFM analysis, could be that in the standard cerium samples the surface morphology is markedly granular while in the samples treated in static air it is more dense, with well developed (00l) terraces, where the rms roughness is <1 nm, (fig.4.3(a,b) pag.79 and fig. 4.7 pag.82). The grain boundaries are very reactive zones with high energy, so it could be plausible that the 750ºC CeO_2 samples non treated in static air, due to their more extended grain boundary network are more prone to react with YBCO.

We also tested the samples of CeO_2 grown directly in static air at 1000ºC for 8h and a heating ramp of 1500ºC/h. This treatment to texture the ceria film is much more reproducible than the post-annealing in air, as reported in chapter 4. In Fig.7.20 XRD patterns of a TFA-YBCO film and a PLD-YBCO one grown on two of these templates are presented. One of the main differences in the two spectra is the relative amount of $BaCeO_3$ that has formed, which is smaller in the PLD films.

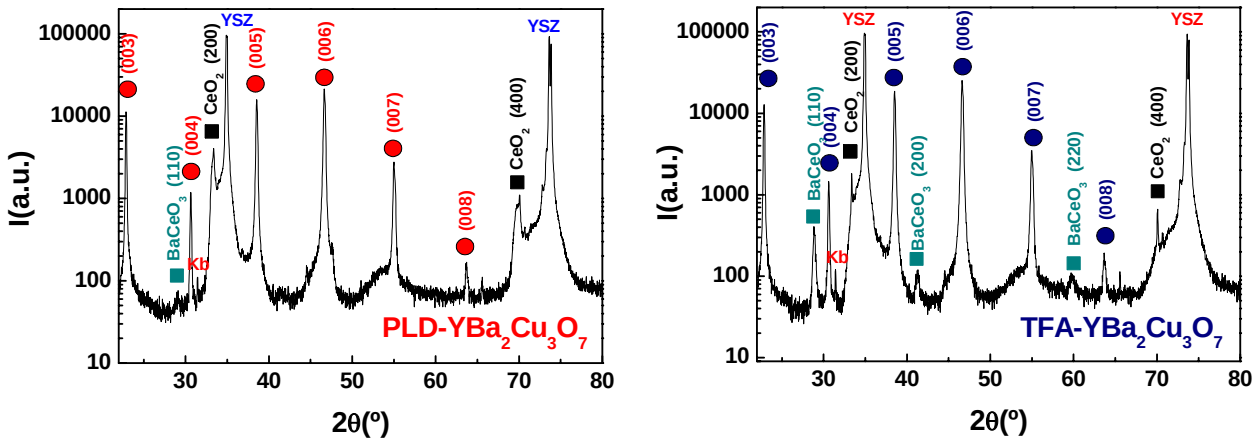

Fig. 7.20: XRD patterns of two samples of YBCO grown on a CeO_2 films synthesised directly in air at 1000ºC for 8h. The YBCO films have been deposited by PLD (left) and TFA (right). In both spectra an amount of $BaCeO_3$ has been detected.

The PLD-YBCO on the CeO_2 directly grown in static air, presented the maximum inductive critical current density obtained on a MOD-ceria thin film, Jc at (5K)=1.6 E7 A/cm^2 and Jc at (77K) =1.2 E6 A/cm^2.

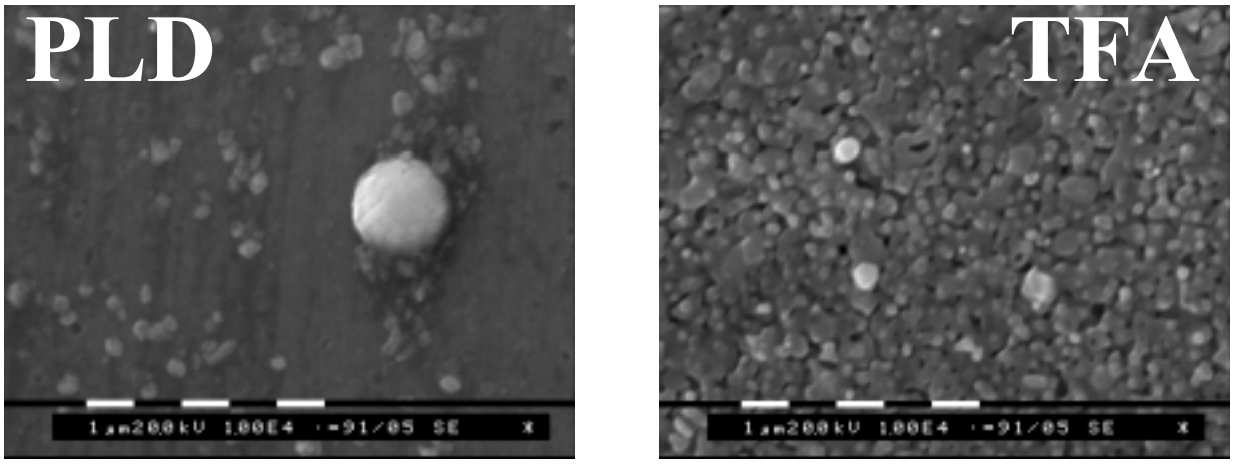

Fig. 7.21 : SEM images of TFA and PLD YBCO films on CeO_2/YSZ. No a/b grains are present in both films. TFA-YBCO is granular with some pores compare to the more compact PLD-YBCO.

SEM images of the samples, fig. 7.21, shows that the TFA-YBCO film morphology is granular compared with the PLD one. Small porosity is visible in the right image while on the left one the film looks like very dense. In both case no ab-planes are detected.

Plotting the in-plane texture together with the critical current densities of TFA-YBCO, no correlation between the in-plane misorientations and Jc(5K) values have been found fig. 7.22(a). The difference in the FWHM of the samples is not high enough to explain the variation in the superconducting properties.

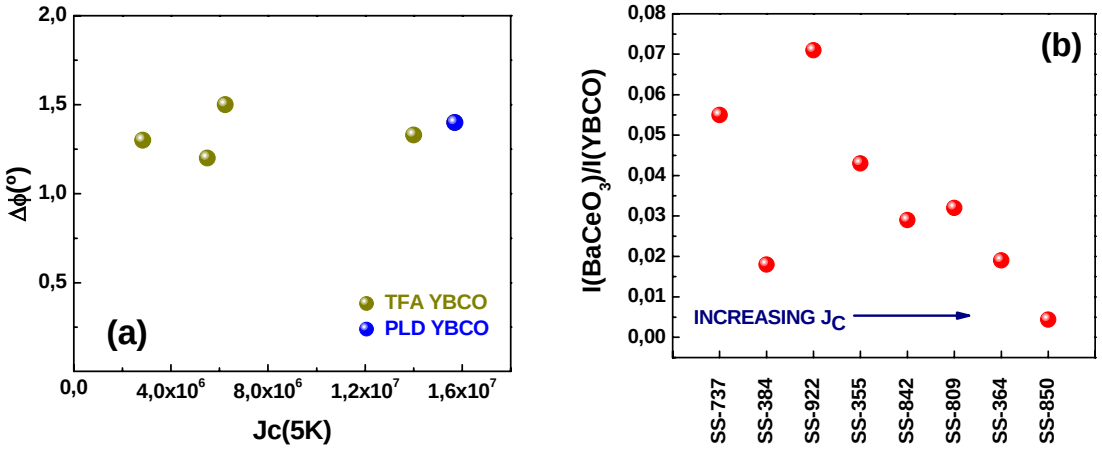

Fig. 7.22(a,b) : (a) Critical current densities measured at 5K as a function of the in plane texture. (b) Relation between the sample quality and the amount of $BaCeO_3$ formed.

Analysing more carefully the XRD patterns we found that the current density of the samples could be correlated with the formation of $BaCeO_3$, (fig.7.22(b)). The intensity of the (110) peaks of the $BaCeO_3$ have been normalised with the (005) of the YBCO films. The PLD sample, SS-850, with the highest critical current density, on the right, has the lowest ratio of intensities. This behaviour could not be only correlated with the reaction of part of the YBCO with ceria. Supposing that no more than 30 nm of superconducting film could have reacted with the CeO_2, the new Jc value, calculated tacking in account the reduced film thickness, is not enough to explain such a difference in J_C between samples grown at the same synthesis conditions. One reason could lie on the way and when the $BaCeO_3$ forms.

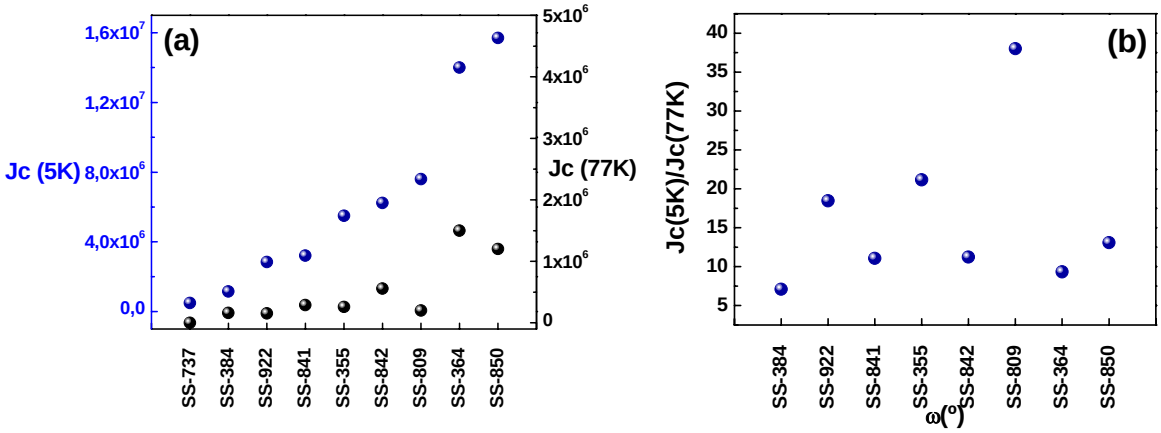

Fig. 7.23(a,b): Jc values measured at 5 and 77 K of YBCO samples grown on CeO_2/YSZ template (a). Anomalous relation Jc (5K)/ Jc (77K) probably due to bad samples oxygenation (b).

In fig. 7.23(a) the current densities measured at 5K and 77K are presented. Usually the Jc(5K)/J_C(77K) ratio between 5K and 77K should be a factor ten. The higher differences shown in fig. 7.23(b) for some samples are probably associated with a bad oxygenation. A XTEM image of one of the TFA-YBCO grown on CeO_2/YSZ film post annealed in air is presented in fig.7.24. The YBCO film exhibits a good texture and a flat interface almost free of $BaCeO_3$ [15].

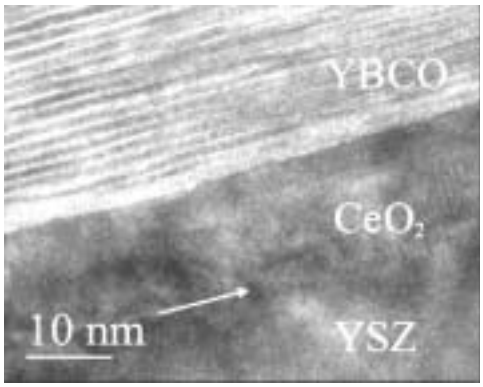

Fig. 7.24: XTEM image reveal a flat interface between CeO_2 and YBCO

7.4.2 TFA-DEPOSITION OF YBCO ON CeO_2/YSZ(IBAD)/SS

The main problem in the TFA-synthesis on stainless steel templates arises from the poor texture of the YSZ templates with $\Delta\phi>9^{\circ}$, limit value to obtain an YBCO film with high J_C. When the YBCO is deposited on a MOD ceria grown in Ar/H_2, disordered material is obtained as concluded from previous experiments on single crystal substrates. On the contrary the ceria templates on YSZ(IBAD)/SS grown in air are able to transfer its texture to the YBCO film. In fig. 7.25, the XRD pattern of a superconducting film grown by TFA on a CeO_2 synthesised directly in air at 900ºC for 8h is presented.

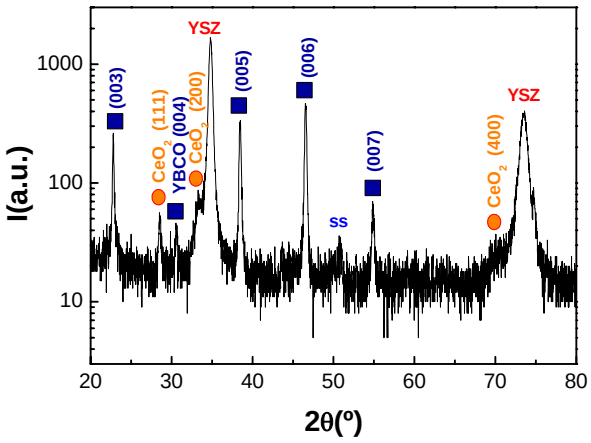

Fig. 7.25: θ/2θ analysis of a textured TFA-YBCO film deposited on CeO_2/YSZ(IBAD)/SS synthesised directly in static air at 900ºC for 8h.

The YBCO is only (00l) oriented. The difference with respect to the samples grown on a YSZ single crystal is that no traces of $BaCeO_3$ are detected, on the other hand the (111) CeO_2 orientation after the YBCO synthesis appears probably due to a secondary ceria recrystallisation .

The out of plane texture ((005) ω-scan), as explained in chapter 6, depends on the ϕ angle at which the measure is performed. In fact the FWHM varies from 12.6º-7.5º-6.4º varying ϕ from 0º to 90º (fig. 7.26).

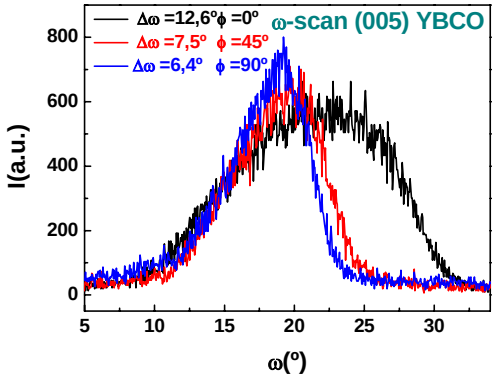

Fig. 7.26: Rocking analysis of the (005) reflection of YBCO as function of the ϕ position of the substrate during the scan.

The ϕ-scan analysis of the (111) reflections of YSZ, and CeO_2 after YBCO deposition, and the (102) reflection of YBCO, corresponding to the same sample, are shown in fig. 7.27.

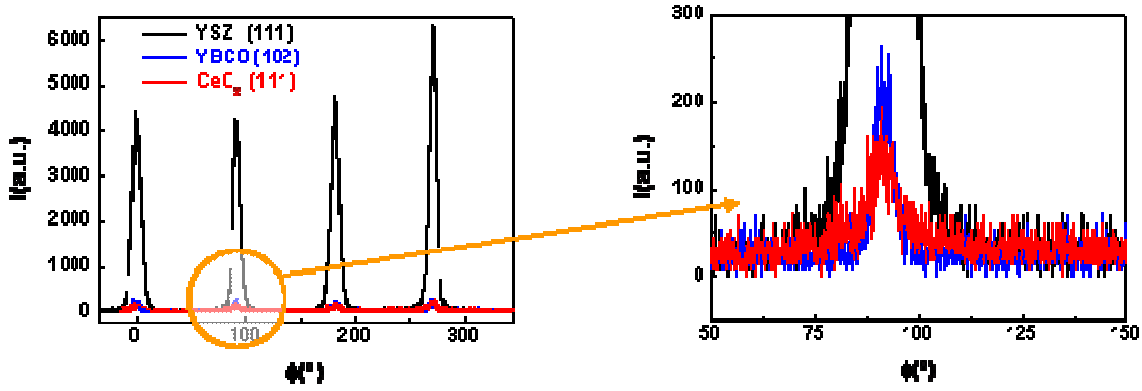

Fig. 7.27: ϕ-scan analysis of (111) YSZ, (111) CeO_2 and (102) YBCO reflections of a TFA-YBCO/CeO_2/YSZ(IBAD)/SS sample fall at the same ϕ angles confirming the geometrical configuration found on single crystals.

The cube on cube relationship of ceria with YSZ(IBAD)/SS, and diagonal with YBCO is confirmed again. The ceria film that has not recrystallised in (111) orientation, maintains a certain in-plane texture. Table 7.5 summarizes the in plane texture FWHM of the multi layer sample:

TABLE 7.5: In plane texture improvement from the YSZ/SS substrate passing trough the CeO_2 buffer layer to the top YBCO film.

ϕ-PEAKS	**0º**	**90º**	**180º**	**270º**	**MEAN FWHM**
Ref. YSZ	9.1º	7.2º	9.3º	7.6º	**8.3º**
Ref. CeO_2	8.4º	7.1º	8.4º	6.1º	**7.5º**
Ref. YBCO	7.6º	4.6º	7.9º	5.4º	**6.4º**
Ref. Residual CeO_2 (111)	11.3º	10º	10.7º	9.2º	**10.3º**

It is interesting to note that the in-plane texture of the films deposited on YSZ(IBAD)/SS substrate improves with the increase of the film thickness grown on it: from 8.3º of the YSZ to 6.4º of the YBCO. Deeps investigations are necessary to understand which are the mechanisms involved in this behaviour. The cerium oxide grown by PLD [24] self-improves its texture above 300 nm, reducing the FHWM from 24º of the substrate to 6º of the cerium oxide. In CSD techniques on the other hand this reduction of FWHM starts to be effective in films with a thickness of only 35 nm as in the case of CeO_2. The SEM images of this sample indicate a surface that even exhibiting a granular morphology, is dense and with small occasional porous. No a/b grains are observed, (fig.7.28).

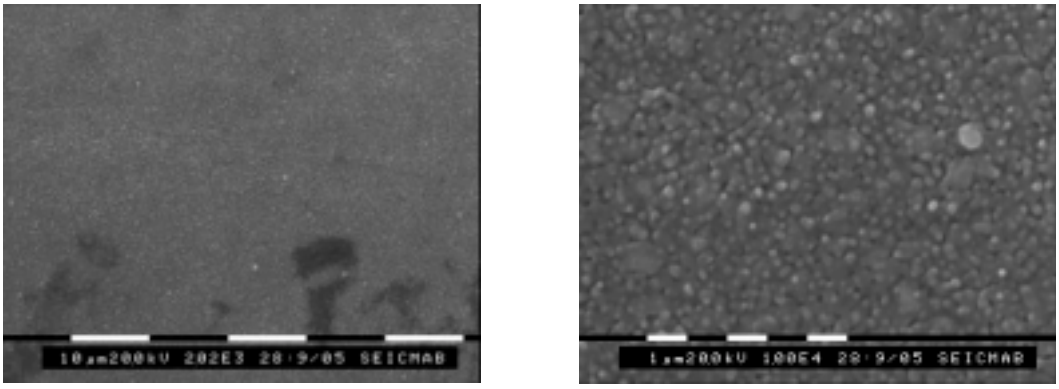

Fig. 7.28: SEM micrograph of the TFA-YBCO/CeO_2/YSZ(IBAD)/SS sample; a homogeneous granular morphology and a low porosity are observed.

Inductive J_C measurements confirm the good quality of the YBCO superconductor film, (fig. 7.29), Jc(5K)= 7 MA/cm^2 and Jc(77K)= 6·10^{5}A/cm^2. These values are near the target of one of one million A/cm^2 at 77K. The thickness of this $YBa_2Cu_3O_7$ film calculated by profilometry is of about 250nm, that corresponds in a hypothetical superconducting cable at a critical current I_C~15 A per cm.

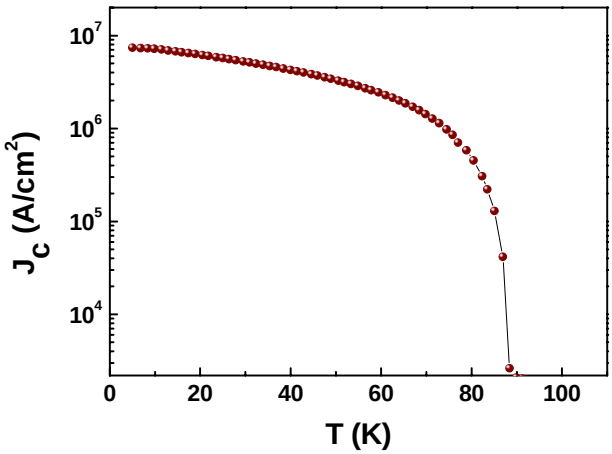

Fig. 7.29: Temperature dependence of the critical current density of the YBCO/CeO_2/YSZ(IBAD)/SS sample.

7.4.3 TFA-DEPOSITION OF YBCO ON $SrTiO_3/BaZrO_3/MgO$

Finally we present results obtained on the STO/BZO double buffer layers. The synthesis temperature was 795ºC; the rest of process conditions were the same as those employed previously, pag.157. Fig. 7.30 presents the XRD pattern of one of these samples, TFA-YBCO/STO/BZO/MgO^{SC} (left panel), to be compared with a PLD-YBCO film grown on CSD-STO/BZO/MgO^{SC} (right panel). The BZO and the STO signals overlap with the (200) of MgO and the (006) peak of the YBCO respectively.

The patterns indicate that the films, in both cases, are prevalently c-axis oriented, although the presence of the (200) peak of YBCO indicates occurrence of a-axis oriented grains.

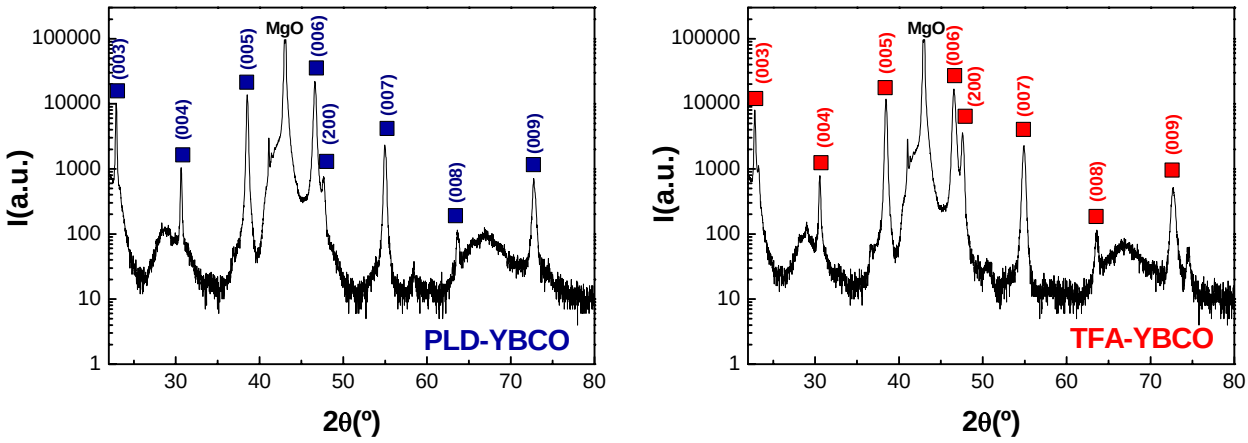

Fig. 7.30: XRD patterns of TFA and PLD -YBCO films grown on two $SrTiO_3/BaZrO_3/MgO$ templates prepared at the same synthesis conditions is presented. YBCO (200) peak in both samples has been found indicating a certain a/b grain growth of YBCO.

The presence of a-grains in both films, grown by PLD and TFA, indicates that they very likely appear as a consequence of surface or structural imperfections of the buffer layer, and the higher content of a-grains in the TFA sample can be attributed to a poorer control of the nucleation in this technique.

The out of plane texture of these two samples is presented in fig. 7.31(a). No differences in the FWHM, Δ~0.3º are observed. The in-plane texture was measured

choosing for each film one reflection not disturbed by diffraction contribution from the others layers. In particular the (222) for MgO, (101) of BZO, (111) of STO and the (102) for the YBCO film were selected. From the analysis of ϕ-scans it is concluded that the epitaxial relation ship between the layers is cube on cube fig. 7.31(b).

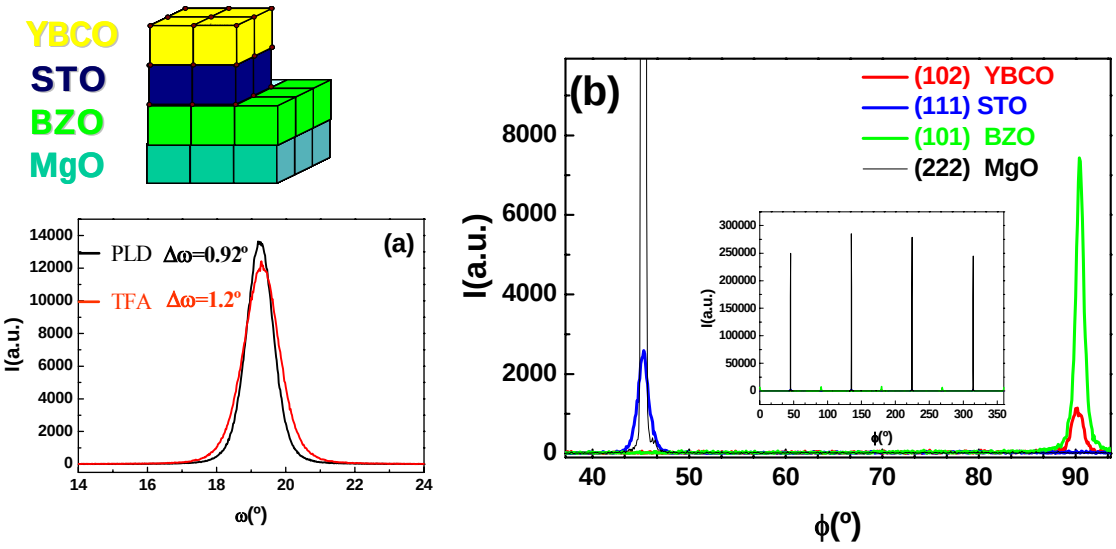

Fig. 7.31(a,b): (005) rocking curve of the YBCO films deposited by PLD and TFA(a). The ϕ–scan indicates that the geometry for the YBCO/STO/BZO/MgO system is cube on cube for each one of the different films (see schematics).

It is worthy to note that there is almost no difference in the in-plane texture of the two YBCO films (PLD and TFA ones). For the PLD-YBCO Δϕ~1.5º and for the TFA-YBCO Δϕ~1.6º . However the Jc value of the PLD film is significant higher.

In table 7.6 all the characteristics of these two samples are resumed.

TABLE 7.6: Confrontation of biaxial texture and critical current density values of the PLD and TFA-YBCO/STO/BZO/MgO samples.

SAMPLES	Δω	Δϕ	J_C(5K) A/cm^2	J_C(77K) A/cm^2
PLD-YBCO/STO/BZO/MgO	0.92º	1.5º	$1\cdot10^7$	$3.7\cdot10^5$
TFA-YBCO/STO/BZO/MgO	1.2º	1.6º	$3\cdot10^6$	$4.4\cdot10^4$

As the underlying buffers have been grown under the same synthesis conditions, we expect that the main difference in the Jc (5K) values could be attributed to the higher amount of a/b grains in the TFA sample. As shown in a recent work [25], a/b planes

formation is correlated with porosity. In fig. 7.32 several samples prepared at the same conditions plus the PLD-one are shown. The plot represents the relative intensity of the (200) peak normalised to the (005) peak of the YBCO film, against the critical current density at 5K. The tendency, as expected, shows a worsening of the Jc with increasing amount of a/b oriented grains.

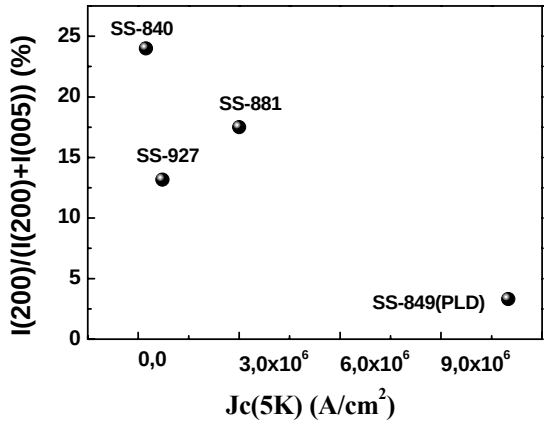

Fig. 7.32: Dependence of the critical current density of YBCO/STO/BZO/MgO samples with the relative intensity of the (200) YBCO peak. A clear decrease of Jc with the increase of a/b grains have been observed

SEM images of the surfaces of these samples are presented in fig.7.33. The samples, from the left to the right, have been ordered by increasing Jc. There is no clear relation between the amount of a/b grains outcropping the surface and the contribution derived from XRD. However a simply inspection of the images reveals an increase of the porosity in the lower Jc samples.

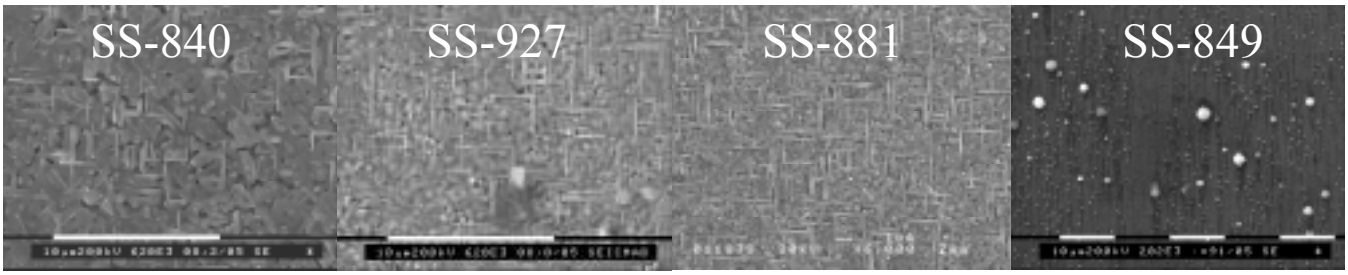

Fig. 7.33: Secondary electron images of YBCO film on STO/BZO/MgO templates. The images are ordered with increasing Jc, from the right to the left. Superficial a/b grains are visible in practically all the samples.

In fig. 7.34 the resistivity analysis of a TFA (right) and the PLD (left) samples are presented. The PLD YBCO does not show any residual resistivity at 0 K while for the

TFA one ρ is near 300 μΩ·cm in agreement with the presence in the film of high porosity formed during a/b grain growth.

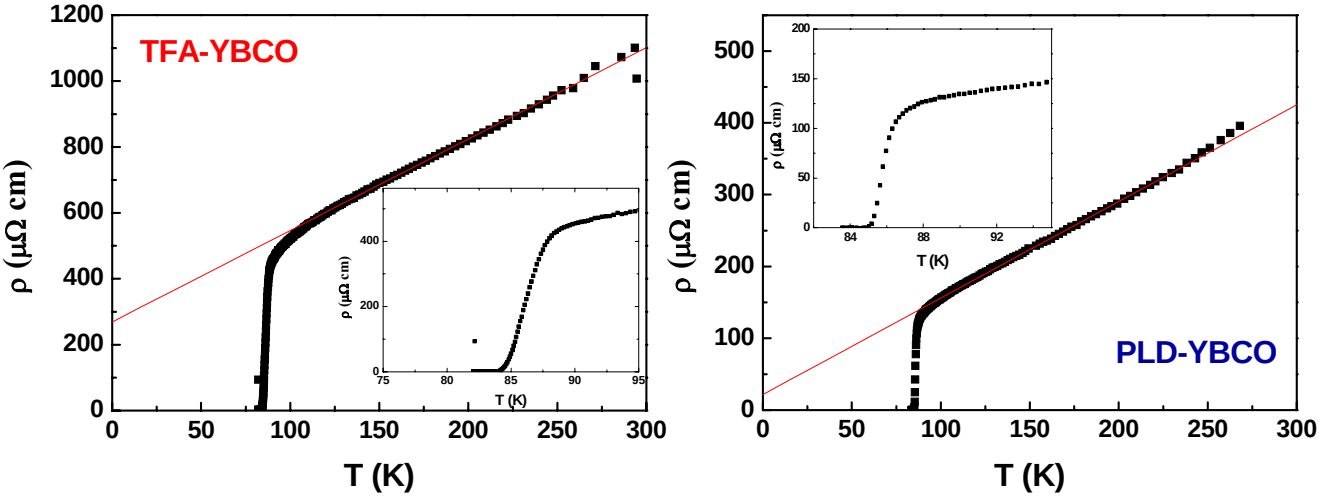

Fig. 7.34: Resistivity as a function of temperature for the TFA (left) and PLD(right) YBCO/ STO/BZO/MgO samples. The insets show a zoom of the transitions zone, from which a Tc of 82K and 84K for the TFA and PLD-YBCO, respectively, has been extrapolated. The difference in the residual resistivity of the two sample at 0 K is due to the higher presence of a/b grains in the TFA sample.

In the insets the transition temperatures are better shown and their values are respectively Tc= 82K for the TFA sample and Tc= 84K for the PLD one. Discarding only a bad oxygenation, it is possible that some MgO has interdiffused into the YBCO film passing trough the double buffer layer. Studies in melt textured materials suggest that Mg ions could occupy the CuO_2 superconducting planes, and estimate for low doping concentration a decrease in Tc as dTc/dx~-12K/at% Mg ($YBa_2(Cu_{(1-x)}Mg_x)_3O_7$) [26]. Further experiments are necessary to confirm this hypothesis in our samples.

7.4.4 TFA-DEPOSITION OF YBCO ON $SrTiO_3/BaZrO_3$/NiO(SOE)/Ni

The best sample of TFA-YBCO on a STO/BZO/NiO/Ni template is presented in fig.7.35. The XRD pattern shows a (00L) oriented YBCO film, although the (200) reflection indicates a certain amount of a/b grains. The inset shows the rocking curve of the (005) peak of YBCO film, with Δω=8º.

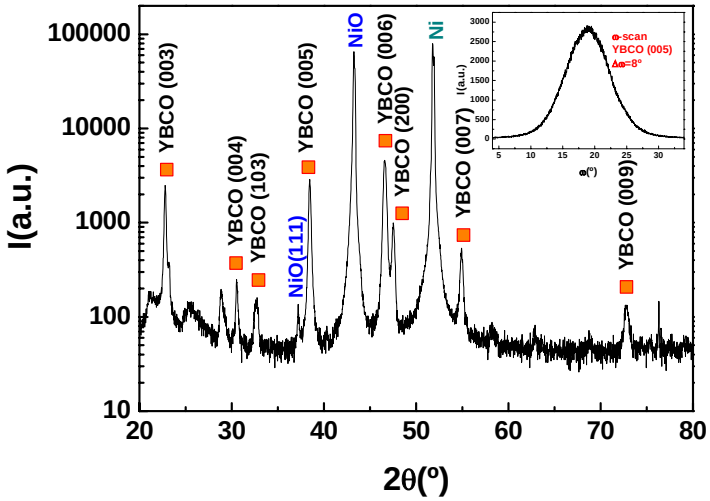

Fig. 7.35: XRD pattern of one TFA-YBCO film grown on a STO/BZO/NiO(SOE)/Ni template. The film has grown with (00l) orientation even if an a/b grain growth has been detected. In the inset the (005) YBCO rocking curve is shown.

The in plane analysis of the substrate and the upper films is summarised in table 7.7.

TABLE 7.7: Summary of the in plane texture improvement of the CSD films of the YBCO/STO/BZO/SOE-NiO/Ni sample.

Ref	Δϕ
Ni (111)	6.1º
NiO (111)	6.6º
BZO (101)	8º
STO (101)	7.3º
YBCO (102	6.6º

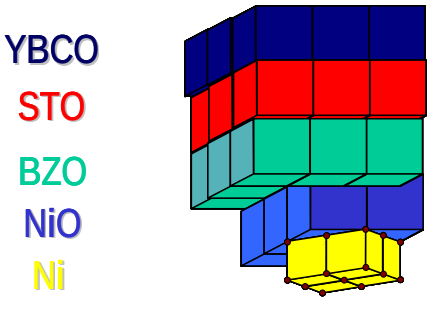

Δϕ improves from the first BZO, Δϕ=8º, to the upper YBCO film with Δϕ=6.6º. The ϕ-scan measured through reflections (111) Ni, (111) NiO, (101) BZO, (101) STO, and (102) YBCO presented in fig. 7.36, define a cube on cube architecture except for the NiO that grows on the diagonal of nickel cell.

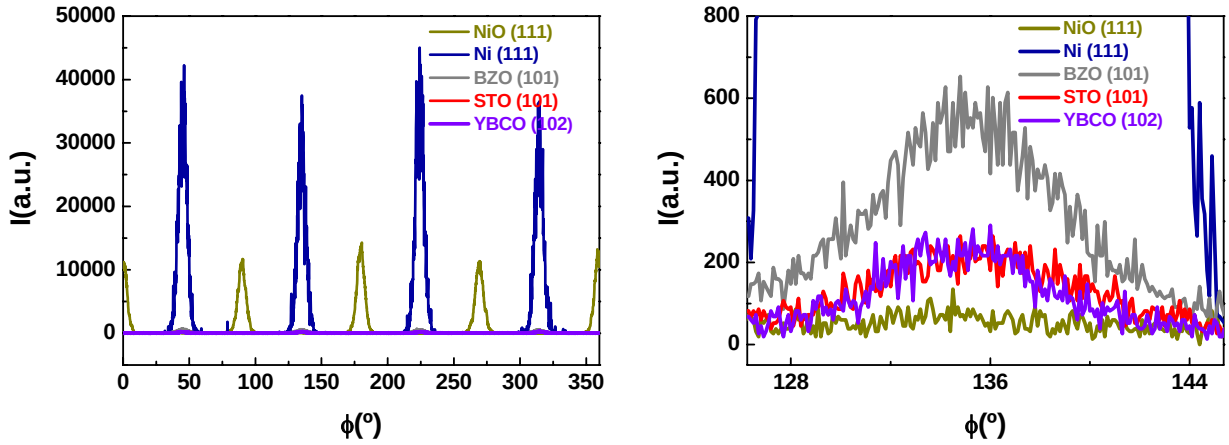

Fig. 7.36: Study of the growth configuration of the YBCO/STO/BZO/NiO/Ni sample through the in plane analysis of the Ni (111), NiO (111), BZO (101), STO and YBCO (102) reflections.

Critical current densities of Jc(5K)=$5\cdot10^5$A/cm^2 and Jc(77K)=$2.5\cdot10^4$cm^2 have been achieved, (fig. 7.37(a)).

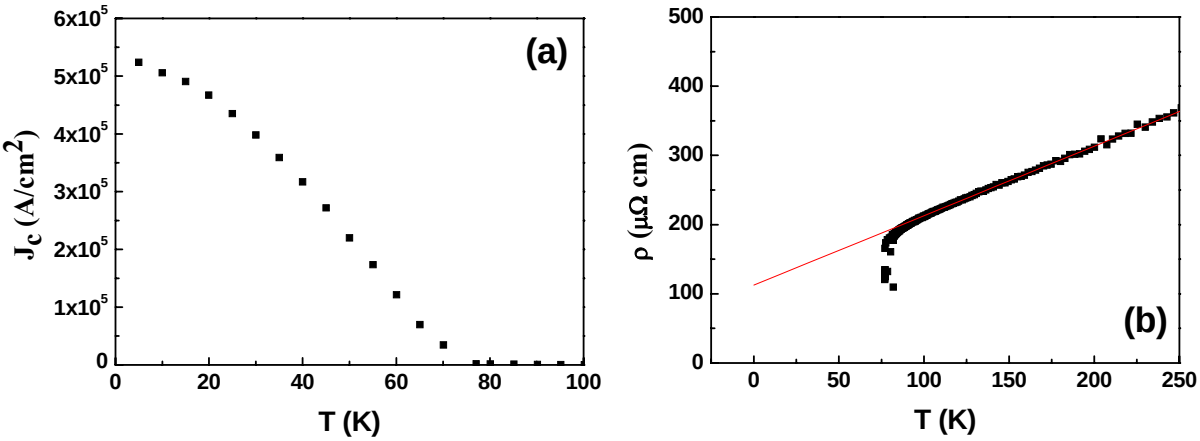

Fig. 7.37(a,b): (a) Dependence of Jc with temperature. Also in the YBCO/STO/BZO/NiO/Ni the Jc decreases anomalously probably due to phenomena of Ni diffusion. (b) Resistivity measure indicates a Tc= 77K, the ρ at 0 K is near 100 μΩ ·cm.

The resistivity analysis, fig. 7.37(b), indicates a Tc near 77K that explains the high decrease of critical current density with temperature. The porosity connected with a/b grain growth is again confirmed by a residual resistivity near 100 μΩ · cm.

Secondary electron image of the sample surface, fig. 7.38(a), indicates the presence of superficial a/b grains. Their orientation seems to follow the cell orientation of NiO fig. 7.38(b).

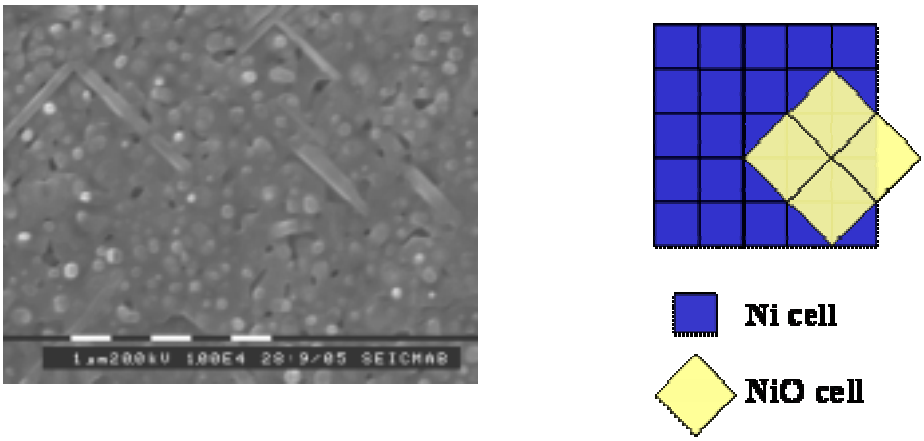

Fig. 7.38(a,b): (a) SEM image of the YBCO surface, a/b grains are present. (b) The a/b grains seem to follow the cell orientation of the NiO as shown in the drawing.

Compared with the SEM image of YBCO grown on STO/BZO/MgO^{SC} (pag. 173), the a/b planes are rotated by 45º to each other. The NiO cell has the same angular difference with the underlying Ni one. The film is quite dense with some pores related to the presence of the a/b grains.

7.5 CONCLUSIONS

The best sample of TFA -YBCO/ MOD-CeO_2/YSZ(IBAD)/SS with its 15 A per cm and a thickness of 250 nm, is a good starting point further optimizations.

In fig 7.39 plot of ϕ-scan versus critical current density at 77K is presented. This plot has been constructed using data from YBCO samples grown by vacuum technique on bicrystals and on polycrystalline IBAD and on RABIT templates. The limiting factor of the YBCO in plane texture makes this line a reference for the maximum accessible Jc. The coloured points correspond to the best YBCO samples reported in this chapter by TFA or PLD: CeO_2/YSZ^{SC}, STO/BZO/MgO^{SC}, CeO_2/YSZ(IBAD)/SS and STO/BZO/NiO(SOE)/Ni.

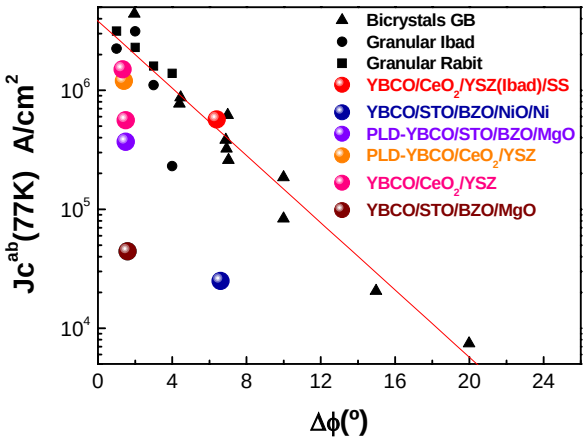

Fig. 7.39: Critical current densities of different samples in relation with the in plane misorientation, $\Delta\phi$.

All the YBCO samples grown on ceria are near by the red line, indicating a quite optimum Jc value for that particular in plane texture. The major difference is detected with the samples synthesised on STO/BZO(MgO or NiO). Our results suggest that the gap cam be filled by reducing the a/b plane growth in YBCO synthesis. The interdiffusion with MgO or NiO could play a role.

Both ceria on YSZ(IBAD) or STO/BZO on nickel oxide templates appear as promising templates for the future superconducting cable.

REFERENCES

[1] P. Barboux, J. M. Tarascon, L. H. Greene, G. W. Hull, and B. G. Bagley . *J.Appl.Phys.* ***63,*** *2725-2729 (1988*).

[2] G. Moore et. al. *Materials Letter,****7-14****, 415-424, (1989).*

[3] T.Kumagai et al. *Chem. Lett., 1645-1646, (1987).*

[4] T.Kumagai et al. *Chem. Lett. ,511-552, (1988).*

[5] G.R.Paz-Pujalt et al. *Mat. Res. Soc. Symp. Proc.,* ***271****, 193-197, (1992).*

[6] F.Parmigiani et. al. *Phys. Rev. B* ***36,*** *7148, (1987).*

[7] A. Gupta, R. Jagannathan, E. I. Cooper, E. A. Giess, J. I. Landman, and B. W. Hussey. *Appl. Phys. Lett.* ***52****, 2077, (1988).*

[8] P. M. Mankiewich, J. H. Scofield, W. J. Skocpol, R. E. Howard, A. H. Dayem, and E. Good. *Appl. Phys. Lett.* ***51****, 1753-1755, (1987).*

[9] P.C.McIntyr, M.J.Cima, J.A.Smith, R.B.Hallock,M.P.Siegal and J.M.Phillipes. *J. Appl. Phys.* ***71*** *(4), 1868-1877, (1992).*

[10] T.Araki, K.Yamagiwa, K.Suzuki, I.Hirabayashi and S.Tanaka *Supercond. Sci. Technol.* ***14,*** *21, (2001).*

[11] *T.Araki and I.Hirabayashi Supercond. Sci. Technol.* ***16,*** *71-94, (2003).*

[12] T.Araki, H.Kurosaki, Y.Yamada, I.Hirabayashi, J.Shibata and T.Hirayama *Supercond. Sci. Technol.* ***14,*** *783, (2001).*

[13] J.C.Brinker and G.W.Scherer *Sol-gel Science (San Dieg, CA: Academic Press) (1990).*

[14] P.C.McIntyre et al. *J. Mater. Res.,* ***5,12****,2771-2779, (1990).*

[15] J Gazquez PhD tesina Universitat Autonoma Barcelona (2005)

[16] T.Araki, Y.Takahaschi, K.Yamagiwa, T.Yuasa, Y.Iijima, K.Tekeda, S.B.Kim, Y.Yamada and I.Hirabayashi *IEEE Trans. Appl. Supercond.* ***11,*** *2869, (2001).*

[17] J.A.Smith, M.J.Cima and N.Sonnenberg *IEEE Trans. Appl. Supercond.* ***9,*** *1531, (1999).*

[18] T.Araki, Y.Takahashi, K.Yamagiwa, Y.Iijima, , K.Takeda, Y.Yamada, J.Shibata, T.Hirayama and I.Hirabayashi *Physica C,* ***357-360,*** *991,(2001).*

[19] T.Araki, K.Yamagiwa and I. Hirabayashi *Cryogenics,* ***41,*** *675, (2001).*

[20] O.Castanyo, A.Palau, J.C.González, S.Piñol, T.Puig, N.Mestres, F.Sandiumenge and X. Obradors, *Physica C: Superconductivity, **372-376**, 806- 809,(2002)*

[21] O.Castanyo PhD Thesis Universitat Autonoma Barcelona (2004)

[22] O.Castaño, A.Cavallaro, A.Palau, J.C.Gonzalez, M.Rossell, T.Puig, A.Pomar and X.Obradors *Supercond. Sci. Technol. **15** (2002) 1-9*

[23] J.Gonzalez,N.Mestres,T.Puig, J.Gazquez, F.Sandiumenge, X.Obradors, *Phys. Rev. B In press.(2004).*

[24] Y.Yamada, T.Muroga, H.Iwai, T.Izumi, Y.Shiohara *Physica C, **392-396**, 777-782 (2003).*

[25] X.Obradors, T.Puig, A.Pomar, F.Sandiumenge, S.Piñol, N.Mestres, O.Castaño, M.Coll, A.Cavallaro, A.Palau, J.Gazquez, J.C.Gonzalez, J.Gutierrez, N.Romá, S.Ricart, J.M.Moretó, M.D.Rossell and G.van Tendeloo, Supercono.Sci.Technol., **17**, 1-10, (2004).

[26] J.Figueras, T.Puig, A.Carrillo and X.Obradors *Supercono.Sci.Technol. **13**, 1067-1073 (2000).*

GENERAL CONCLUSIONS

- ***MOD-CeO_2 deposition***: firstly we tested several different Sol-gel routes to synthesize cerium oxide; we selected the acetylacetonate route for its easy preparation and reproducible results. The biaxial texture of the CeO_2 thin buffer layer was achieved as demonstrated by the $\Delta\omega=0.5^o$ and $\Delta\phi=0.8^o$ values. Important knowledge on the MOD-CeO_2 thin film growth has been acquired during this research. From a combination of TEM, XRD and RHEED analyses it was observed that its growth mechanism exhibits an anomalous behaviour compared with other CSD derived films. The homogeneous nucleation in fact is favoured in this MOD process due to the low Tnuc./Tmel value for ceria film (Tnuc./Tmel=0.21). Only grains nucleated on the substrate are textured as observed in XTEM images. The grain size dependence with temperature follows an Arrhenius relation: $\langle r\rangle^2=\alpha_o \exp(-Q/kT)$, characteristics of 3D undergoing thermally activated grain growth . In agreement with Q= 1.1 eV obtained in other CeO_2 films by X.-D. Zhou et al., a value of Q= 1.04 eV has been obtained. This value is larger than that determined for bulk nanostructure CeO_2, about a factor two. In agreement with such an indication of reduced grain boundary mobility, EELS analyses revealed a significant fraction of residual C decorating the grain boundaries, that very likely acts as a growth by blocking grain boundary motion. The process of post annealing or direct growth in static air, have demonstrated the possibility of growing completely epitaxial CeO_2 films. EELS analyses of such samples clearly demonstrates that the oxygen clean up grain boundaries from C impurities thus unblocking grain growth. The growth of biaxially textured grains follows a secondary growth regime, which explains the growth rate dependence on the total thickness of the film. In the synthesis or post annealing in air an important change in the film surface morphology has been observed, compared to the synthesis in Ar/H_2. At 1000ºC (111), (001) facetted appeared, instead of the granular grains. After a long process of synthesis parameter optimisation, we are now able to control exactly the

epitaxial growth of ceria growth: precursor solution of 0.25M concentration, heating ramp of 1500ºC/h, synthesis temperature of 1000ºC for 8h in static air. These conditions are optimum for a 30 nm film thickness. It has been verified that Cerium oxide can be grown on YSZ(IBAD)/SS with only the (00l) orientation. The optimised process has been adapted to stainless steel substrate reducing the synthesis temperature at 900ºC in order to preserve the metal tape against oxidation. The roughness rms values of $20 \cdot 20\ \mu m^2$ areas are in the range of 9-21 nm but locally, on the terrace surface, rms is of the order of 1 nm. We observed an interesting phenomenon of in plane texture improvement of the ceria film with respect to the underlying YSZ(IBAD)/SS substrate, from $\Delta\phi_{YSZ}$ = 8.3º and to $\Delta\phi_{CeO2}$ = 7.5º.

- ***MOD-$SrTiO_3$ and $BaZrO_3$ deposition***: The solution preparation and the deposition conditions for STO and BZO on MgO and YSZ have been optimised. The roughness dependence with the synthesis temperature has been confirmed for the different systems and buffer layers. These systems show a worsening of surface roughness and biaxial texture at high temperature, that may be associated with secondary grain growth of surface grains. Thus in this case, the optimum synthesis temperature lowered to 700ºC. After several experiments of buffer deposition on YSZ(IBAD)/SS and NiO(SOE)/Ni technical metal substrates the most promising architecture resulted to be the STO/BZO/NiO(SOE)/Ni. Owing to the low mismatch between BZO and NiO(SOE) and structural similitude of the two perovskites STO and BZO, with this system we achieved the best biaxial texture values.
- ***TFA YBCO deposition on optimised buffer layers:*** we have grown YBCO by the TFA method on the optimised buffer layers. In the case of CeO_2 only the buffers submitted to oxygen annealing permit the growth of well-textured YBCO films. The CeO_2 samples react completely with YBCO forming $BaCeO_3$. This reaction probably happens when the YBCO has already grown. The enhanced grain connectivity and terraced topography probably minimize the reactivity of YBCO with cerium oxide in the treated samples. The amount of $BaCeO_3$ is correlated with the critical current density of the YBCO film. The comparison of the superconducting properties of PLD and TFA- YBCO deposited on MOD-CeO_2 has revealed minor differences probably associated

with the more complex nucleation and growth path of TFA derived films . In some TFA-samples an anomalous decrease of Jc at (77 K) with respect to the value at 5K has evidenced some problems of the oxygenation process, that are under investigation. A sample of TFA-YBCOon a CeO_2/YSZ(IBAD)/SS template prepared in air at 900ºC for 8 h has shown a critical current density, J_c has a value of 7 MA/cm^2 at 5K, and $6 \cdot 10^5$A/cm^2 at 77K. These values are near the target of one million A/cm^2 at 77K. The thickness of this $YBa_2Cu_3O_7$ film calculated by profilometry is 250nm, that corresponds to a critical current I_C~15 A per cm. SEM and XRD texture analysis confirm the high quality of the YBCO film. The texture of the YBCO improves the underlying ceria one, $\Delta\phi_{CeO2}=7.5^o$ and $\Delta\phi_{YBCO}=6.4^o$. The experiments on BZO and STO buffer layers have demonstrated the possibility of using the double buffer on NiO(SOE)/Ni as an alternative template for YBCO deposition. The critical current densities of YBCO films grown on the model system STO/BZO/MgO by PLD and TFA, at 5 K, show a good Jc considering that in all the samples, also the PLD one, a/b grain growth has been observed. The porosity associated with a/b grain growth produces a worsening of the superconducting properties. At 77 K the critical current density decreases abruptly probably due to the diffusion of Mg cations through the double buffer layers into the YBCO film. Similar diffusion problems have been detected using the NiO(SOE)/Ni metal substrates. A critical current density of Jc(5K)= $5 \cdot 10^5$A/cm^2 has been achieved for the best sample of YBCO/STO/BZO/NiO(SOE)/Ni.

- ***Future plans:*** It is important to understand why on metal substrates, increasing the film thickness the texture improves. Controlling this behaviour, combined with better textured YSZ(IBAD)/SS substrates, will help to obtain samples with higher critical current densities. In the case of NiO(SOE)/Ni substrates, it is necessary test thicker buffer layers to avoid the metal diffusion and new synthesis conditions to prevent the a/b grain growth during YBCO deposition.